Single atom dynamics in silicon

Joost van der Heijden

A thesis in fulfilment of the requirements for the degree of
Doctor of Philosophy

The University of
New South Wales

School of Physics

Faculty of Science

February 2017

THE UNIVERSITY OF NEW SOUTH WALES
Thesis/Dissertation Sheet

Surname or Family name: van der Heijden

First name: Joost Other name/s:

Abbreviation for degree as given in the University calendar: PhD

School: Physics Faculty: Science

Title: Single atom dynamics in silicon

Abstract:

The experimental study of semiconductors has advanced to the point where individual atoms can be addressed in measurements and, more importantly, manipulated. Single atoms are of great interest as they provide charge, orbital, and spin degrees of freedom, which can be harnessed for emerging quantum technologies. In this thesis state-of-the-art silicon field-effect transistors have been used to probe and control single atoms. This approach benefits from the availability of a highly-developed fabrication platform for silicon nanostructures. In addition, silicon naturally provides a small density of nuclear spins, producing little magnetic background disturbance.

The main focus of this thesis is the investigation of single boron atoms in silicon. The quantum states of holes bound to acceptor atoms are attractive for quantum information processing because of the presence of spin-orbit coupling. Under the right conditions, this gives rise to a strong dipole coupling in a two-level quantum system. Such spin-orbit quantum bits are promising, because of their fast electrical control by local electrodes and long-distance quantum bit coupling via cavity modes.

In this thesis single boron atoms have been identified in both electrical transport and rf gate reflectometry measurements of transistors at cryogenic temperatures. A comprehensive study of the Zeeman effect on the four-fold degenerate ground state of an acceptor shows a strong influence of the local environment. Furthermore, measurements on two coupled acceptors demonstrate, for the first time, the interaction between heavy holes and light holes, which is governed by the spin-orbit coupling. Fundamental heavy-light hole relaxation and heavy-light hole mixing have been observed.

Additionally, the potential of single-atom transistors to be used as efficient single-electron pumps has been explored in this thesis. Quantized charge pumps are promising single electron sources, which could produce a new quantum standard for the Ampere. A single-atom specific model has been developed to describe the distinctive operation of a silicon single-atom electron pump, as observed in recent experiments, and to investigate possible improvements of this pump.

These results demonstrate the distinct dynamical behavior of individual atoms in silicon and thereby show their prospect to be used in the fields of quantum information and quantum metrology.

FOR OFFICE USE ONLY Date of completion of requirements for Award:

ORIGINALITY STATEMENT

'I hereby declare that this submission is my own work and to the best of my knowledge it contains no materials previously published or written by another person, or substantial proportions of material which have been accepted for the award of any other degree or diploma at UNSW or any other educational institution, except where due acknowledgement is made in the thesis. Any contribution made to the research by others, with whom I have worked at UNSW or elsewhere, is explicitly acknowledged in the thesis. I also declare that the intellectual content of this thesis is the product of my own work, except to the extent that assistance from others in the project's design and conception or in style, presentation and linguistic expression is acknowledged.'

Signed ……..

Date ……..

Abstract

The experimental study of semiconductors has advanced to the point where individual atoms can be addressed in measurements and, more importantly, manipulated. Single atoms are of great interest as they provide charge, orbital, and spin degrees of freedom, which can be harnessed for emerging quantum technologies. In this thesis state-of-the-art silicon field-effect transistors have been used to probe and control single atoms. This approach benefits from the availability of a highly-developed fabrication platform for silicon nanostructures. In addition, silicon naturally provides a small density of nuclear spins, producing little magnetic background disturbance.

The main focus of this thesis is the investigation of single boron atoms in silicon. The quantum states of holes bound to acceptor atoms are attractive for quantum information processing because of the presence of spin-orbit coupling. Under the right conditions, this gives rise to a strong dipole coupling in a two-level quantum system. Such spin-orbit quantum bits are promising, because of their fast electrical control by local electrodes and long-distance quantum bit coupling via cavity modes.

In this thesis single boron atoms have been identified in both electrical transport and rf gate reflectometry measurements of transistors at cryogenic temperatures. A comprehensive study of the Zeeman effect on the four-fold degenerate ground state of an acceptor shows a strong influence of the local environment. Furthermore, measurements on two coupled acceptors demonstrate, for the first time, the interaction between heavy holes and light holes, which is governed by the spin-orbit coupling. Fundamental heavy-light hole relaxation and heavy-light hole mixing have been observed.

Additionally, the potential of single-atom transistors to be used as efficient single-electron pumps has been explored in this thesis. Quantized charge pumps are promising single electron sources, which could produce a new quantum standard for the Ampere. A single-atom specific model has been developed to describe the distinctive operation of a silicon single-atom electron pump, as observed in recent experiments, and to investigate possible improvements of this pump.

These results demonstrate the distinct dynamical behavior of individual atoms in silicon and thereby show their prospect to be used in the fields of quantum information and quantum metrology.

Acknowledgements

The 24-hour flight from Amsterdam to Sydney in 2011 started the incredible journey of my PhD, which turned into a fantastic life experience. This thesis could not have been accomplished without the continuous support I received from my family, broadcasted from the other side of the world, and from the incredible people I met in Australia.

First and foremost, I would like to thank my supervisor Prof. Sven Rogge for giving me the freedom and trust to run interesting experiments, for his excellent guidance and encouragement throughout my PhD, and for always making time when I needed help.

I also want to thank my colleagues, who had a tremendous impact on my working and personal life. I am very grateful to Arjan and Jan who welcomed me back in Sydney and ensured a smooth start of my PhD, both in the lab and after work. I greatly enjoyed the many dinners and drinks we shared, and I am thankful we sometimes still do, even though we live on different continents. For giving a direction to this thesis I have to thank Jan, Joe and Giuseppe, who convinced me that it would be interesting to study acceptors in silicon. A special thanks goes to Gabriele with whom I have had the pleasure to share the PhD life side by side, and who was always happy to have a discussion, at work or at the bar. I am also particularly greatful to him for the steady supply of coffee beans, which literally kept me going. I would like to thank Giuseppe for his enthusiasm in discussions about charge pumping, and in organizing cycling trips and dinners. I am especially thankful to Juanita for her incredible support and all her good advice. I would like to express my gratitude to Takashi for his unlimited help with the experiments. I am pleased that Guangchong came to Sydney, and may follow up on the work presented here. Of course I would also like to thank all the other current and former colleagues, Chunming, Benoit, Shouyi, BinBin and Wendy for creating a great working atmosphere. Furthermore, I would like to thank all the part-time students that have stayed in the group: Tim, Jay, Junxi, Karsten, Rodrigo, Steefan, Ludo, Adriaan, Maikel, Markus, Nathan, Niccolò and Qi. A special thanks goes to Reinier for performing the electric field dependence experiments presented in chapter 4 of this thesis and for his strong motivation which made his supervision remarkably easy.

To accomplish this work I have had the pleasure to work with many experts in the field. In Sydney I would like to thank Prof. Alex Hamilton, Prof. Michelle Simmons and Matthew House for their support and interest in my measurements. This work would not have been possible without the high quality transistors provided by Nadine Collaert at IMEC and by the CEA Leti through the AFSID and TOLOP projects. I would also like to thank Prof. Andrew Briggs for allowing me to carry out experiments in his group in Oxford. Many thanks to Jan and Alex for showing me Oxford and how to do EDMR experiments.

In Australia I have had the pleasure to meet many other great people, with whom I shared unforgettable moments. For all the exhausting but fun hours spent on the squash court, I would like to sincerely thank John, Juan Pablo, Patrick and CJ. I have a lot of respect for Juanita, CJ, Wolfgang and Lukas who were willing to get locked in (and escape from) a countless number of escape rooms with me. In the last few years I enjoyed every opportunity to discover Australia. I have especially wonderful memories of my trips to Wilsons Prom, Congo and Hat Head in the amazing company of Wolfgang, Juanita, Ben, Matthias, Miriam and Nico. Exploring the Blue Mountains with Martin, Paula, Matt, Kim, Juanita, Wolfgang and Holger has also been an extraordinary experience.

Finally I would like to express my deepest gratitude to my family. I feel very fortunate to always have had the love, the full support, and the confidence of my parents, my sister Rinie, and my brother Dirk. Heel erg bedankt dat jullie me zijn op komen zoeken toen ik besloot aan de andere kant van de wereld te gaan wonen. Ik hou van jullie en kan me geen betere familie voorstellen.

Publication list

Journal articles

- **J. van der Heijden**, T. Kobayashi, M.G. House, J. Salfi, S. Barraud, R. Laviéville, M.Y. Simmons and S. Rogge, *Spin-orbit induced spin dynamics of two coupled atoms in silicon*, in preparation.
- T. Kobayashi, **J. van der Heijden**, M.G. House, M.Y. Simmons and S. Rogge, *Observation of the molecular coupling of a donor pair in a silicon field effect transistor by radio frequency reflectometry*, submitted for publication.
- **J. van der Heijden**, G.C. Tettamanzi and S. Rogge, *Dynamics of a single-atom electron pump*, arXiv:1607.08696.
- M.G. House, I. Bartlett, P. Pakkiam, M. Koch, E. Peretz, **J. van der Heijden**, T. Kobayashi, S. Rogge and M.Y. Simmons, *High sensitivity charge detection with a single-lead quantum dot for scalable quantum computation*, Physical Review Applied **6**, 044016 (2016).
- T. Kobayashi, **J. van der Heijden**, M.G. House, S.J. Hile, P. Asshoff, M.F. Gonzalez-Zalba, M. Vinet, M.Y. Simmons and S. Rogge, *Resonant tunneling spectroscopy of valley eigenstates on a donor-quantum dot coupled system*, Applied Physics Letters **108**, 152102 (2016).
- M.G. House, T. Kobayashi, B. Weber, S.J. Hile, T.F. Watson, **J. van der Heijden**, S. Rogge and M.Y. Simmons, *Radio frequency measurements of tunnel couplings and singlet-triplet spin states in Si:P quantum dots*, Nature Communications **6**, 8848 (2015).
- **J. van der Heijden**, J. Salfi, J.A. Mol, J. Verduijn, G.C. Tettamanzi, A.R. Hamilton, N. Collaert and S. Rogge, *Probing the spin states of a single acceptor atom*, Nano Letters **14**, 1492-1496 (2014).
- J.A. Mol, **J. van der Heijden**, J. Verduijn, M. Klein, F. Remacle and S. Rogge, *Balanced ternary addition using a gated silicon nanowire*, Applied Physics Letters **99**, 263109 (2011).

Conference Presentations

- Contributed talk: *Dispersive singlet-triplet readout of two holes on coupled acceptors in a silicon transistor*, 33rd International Conference on the Physics of Semiconductors, in Beijing, China (August 2016).
- Contributed talk: *Single dopant atoms in a CMOS environment*, Quantum CMOS Intergration Technology workshop, in Delft, the Netherlands (June 2016).
- Poster presentation: *Dispersive singlet-triplet readout of the acceptor spin state*, Silicon Quantum Electronics workshop, in Delft, the Netherlands (June 2016).
- Contributed talk: *RF-gate reflectometry on acceptor states: singlet-triplet relaxation*, Silicon Quantum Information Processing, in Cambridge, the United Kingdom (September 2015).
- Contributed talk: *Double acceptor singlet-triplet relaxation*, Silicon Quantum Electronics workshop, in Takamatsu, Japan (August 2015).
- Contributed talk: *Hole spins in silicon: the advantage of spin-orbit interaction*, Silicon Quantum Information Processing, in London, the United Kingdom (September 2014).
- Contributed talk: *Probing the spin states of a single acceptor atom in silicon*, CMD 25 - JMC 14, in Paris, France (August 2014).
- Poster presentation: *Probing a Single Acceptor in a Silicon Nanotransistor*, IEEE Silicon Nanoelectronics workshop, in Honolulu, the United States (June 2014).
- Poster presentation: *Modeling the Pumping of Electrons through a Single Dopant Atom in a Si MOSFET*, IEEE Silicon Nanoelectronics workshop, in Honolulu, the United States (June 2014).
- Contributed talk: *Probing the spin states of a single acceptor in silicon*, International Conference On Nanoscience and Nanotechnology, in Adelaide, Australia (February 2014).
- Poster presentation: *Transport spectroscopy of a single acceptor in silicon*, International Symposium on Nanoscale Transport and Technology, in Atsugi Kanagawa, Japan (December 2013).

List of figures

List of tables

List of abbreviations and symbols

α	lever arm
α', β', δ'	quadratic electric field coupling constants
Δ	level spacing
Δ_{LH}	light-heavy hole splitting
Δ_{SO}	spin-orbit splitting
$\Downarrow, \Uparrow$	predominantly heavy hole spins
$\downarrow, \uparrow$	predominantly light hole spins
$\gamma_1, \gamma_2, \gamma_3$	electric and magnetic field coupling constants
κ	dielectric constant
μ_B	Bohr magneton
a', b', d'	deformation potential constants
e	electron charge
E_b	binding energy
E_F	Fermi energy
E_Z	Zeeman energy
f_0	resonance frequency
f_h	Fermi-Dirac distribution of holes
f_{dr}	driving frequency
g^*	effective g-factor defined by gm_j
g_1'	linear part of Landé g-factor
g_2'	cubic part of Landé g-factor
$h, \hbar$	Planck constant and reduced Planck constant
J_{LH}	light-heavy hole exchange energy
k_B	Boltzmann constant
m_e	electron mass
m_j	secondary total angular momentum quantum number
O_h	octahedral symmetry
p_{eff}	effective electric dipole moment
S_{s-th}	subthreshold slope
T_1	relaxation time
T_2	coherence time
T_d	tetrahedral symmetry
A_{Ch}	cross section of channel

ac	alternating current
c	speed of light in vacuum
CMOS	complementary metal-oxide-semiconductor
dc	direct current
DOS	density of states
E_C	charging energy
Eq.	equation
Fig.	figure
FinFET	fin field-effect-transistor
H_{fin}	height of fin
IMEC	interuniversity microelectronics center
L_{gate}	length of gate
Leti	laboratoire d'électronique et de technologie de l'information
LZ	Landau-Zener
LZS	Landau-Zener-Stückelberg
MOSFET	metal-oxide-semiconductor field-effect-transistor
MuGFET	multi gate field-effect-transistor
NV	nitrogen-vacancy
QPC	quantum point contact
rf	radio frequency
SCE	short channel effects
SET	single electron transistor
SOI	silicon on insulator
STM	scanning tunneling microscope
V_{Th}	threshold voltage
W_{fin}	width of fin
WKB	Wentzel-Kramers-Brillouin method

Contents

chapter 1

Introduction

"Nature gives us all, including Prof. Lorentz, surprises. It was very quickly found that there are many exceptions to the rule of splitting of the lines only in triplets. The French physicist Cornu was perhaps the first to observe that, contrary to the elementary theory, in some cases splitting into four lines, a quadruplet, occurs. In other cases splitting into five, six or even nine lines can be observed."

- Pieter Zeeman, 1902, Nobel lecture. The Nobel prize in Physics in 1902 was awarded to Hendrik Antoon Lorentz and Pieter Zeeman in recognition of the extraordinary service they rendered by their researches into the influence of magnetism upon radiation phenomena.

1.1 Impurity atoms in semiconductors

In the last hundred years individual atoms, building blocks of all matter, have made a remarkable transition from being merely a physical concept to become measurable objects, which in the last decennia have become the basis for potential applications. In solid state physics in particular, the quantum mechanical properties of atoms are essential to explain the macroscopic behavior of materials. The characteristics of these materials are set by the nature of the atoms and their specific arrangement at the atomic scale, such that any imperfection plays a critical role. This is especially true for semiconductors, where point defects such as the vacancy of an atomic site or the addition of a foreign atom, can significantly change their electronic, magnetic and photonic properties.

The study of imperfections in semiconductor crystals started in the first half of the 20^{th} century, supported by the new theory of quantum mechanics. Experiments on photo-luminescence[1] could then be explained in terms of atomic orbital levels of impurity atoms[2] and electronic band structures of the host semiconductors.[3,4] Additional experimental techniques, such as x-ray diffraction, photo-absorption, Raman scattering, and electron paramagnetic resonance, started to provide a very comprehensive understanding of many defects in semiconductors.[5–7] The interest in semiconductor defects increased greatly with the invention of the transistor technology at Bell labs in 1947. In particular impurity atoms in silicon and germanium became of interest, both experimentally[8] and theoretically,[9] driving the field of semiconductor technology forward. As a consequence, devices based on semiconductor structures, such as transistors, lasers, and diodes, have become indispensible to the modern world.

Research in the 21^{st} century has focused on a new approach to use quantum mechanical effects in semiconductors for applications in emerging technologies. The goal of these investigations is to directly manipulate quantum degrees of freedom, in order to take full advantage of the quantum mechanical properties of superposition and entanglement. One of the most challenging objectives is to build a network of quantum bits, or qubits, representing quantum information in the form of superposition states of quantum two-level systems, and to accurately control the entanglement between these qubits.[10] These quantum computers are predicted to outperform classical computers in computational efficiency for a still increasing number of algorithms.[11] This has stimulated a large global research effort in identifying quantum two-level systems and characterizing

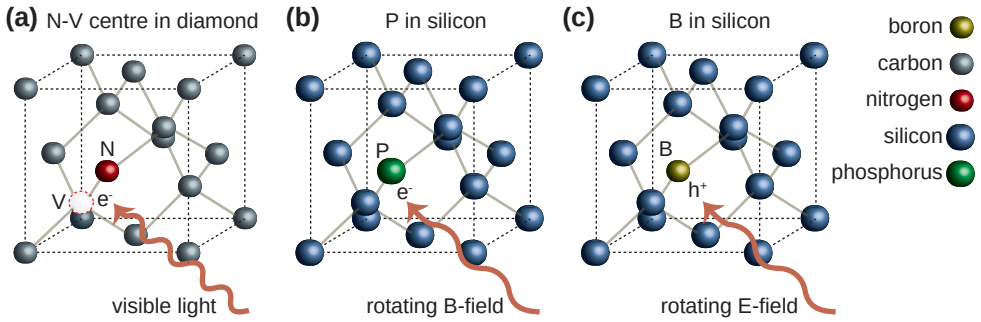

Figure 1.1: Single defects in semiconductors. **(a)** The negatively charged nitrogen-vacancy centre in diamond can be manipulated with visible light at room temperature, which makes it promising for quantum computation and quantum sensing. **(b)** The phosphorus donor in silicon has very long lived electron and nuclear spin states, which can be controlled with an AC magnetic field. **(c)** The boron acceptor in silicon has a hole spin which is strongly affected by the spin-orbit interaction, and can therefore be controlled with an AC electric field.

their properties, which has led to many ground-breaking discoveries in the last decade.[12] Recently this work has been even more encouraged by the investment of some of the biggest technology companies in the world like Intel, IBM, Microsoft and Google.[13] Next to the pursuit of a quantum computer, quantum systems are investigated to be used for inherent secure communication protocols using quantum key distribution,[14] to be used as exceptionally precise quantum sensors[15] and to base our measurement standards on fundamental quantum constants of nature.[16]

The quantized properties of individual impurity atoms in semiconductors form attractive prospects for several of these quantum technologies. Although many of these systems have been successfully studied, two have gained the most attention, being single phosphorus (^{31}P) atoms in silicon and nitrogen-vacancy (NV) centres in diamond, as shown in Figs. 1.1a and 1.1b. In electron paramagnetic resonance studies on ensembles of phosphorus atoms in the late 1950's, both the electron and nuclear spin relaxation times of ^{31}P atoms in silicon were found to be extremely long,[17–19] which led, almost 40 years later, to the proposal of Kane to use these atoms as qubits.[20] Likewise, the photo-luminescence and electron spin resonance properties of NV centres in diamond have been known since the 1970's from studies on ensembles of these defects.[21,22]

Studies on individual defect centres in semiconductors started to take place from the 1980's, a time at which the dimensions of electrical structures had

become small enough (< 1 μm) to sense the effect of single impurities. The first identification of the effect of a single impurity was made through the detection of random telegraph noise coming from the charging and discharging of a single defect in a silicon transistor.[23] More details of individual impurities, such as the charging energy and magnetic spin splitting, were uncovered in resonant tunneling experiments, first performed on Si donors in GaAs quantum wells,[24–26] and later in silicon transistors.[27,28] Direct observations of the spatial extend of defect centres in semiconductors were obtained using scanning tunneling microscopy (STM),[29–31] which resulted in a comprehensive knowledge about their electrical and structural arrangement.[32] The first optical identifications of single defect centres were reported on NV centres in diamond,[33] followed by individual acceptor atoms and pairs of nitrogen atoms in GaAs,[34,35], nitrogen and Te impurities in ZnSe,[36,37] and pairs of nitrogen atoms in GaP.[38]

In recent years substantial progress has been made towards realizing quantum technologies using single impurities in semiconductors. Individual phosphorus atoms have shown nuclear spin coherence times over 30 seconds, while having a high enough quantum gate control fidelity to envision quantum error correction protocols,[39,40] thereby showing their potential use as qubit. Furthermore, placement of phosphorus atoms with atomic precision has been demonstrated using scanning tunneling lithography.[41] Meanwhile, NV centres in diamond have been used as quantum sensors with ultrasensitive detection of magnetic fields,[42–45] electric fields,[46] temperature,[47,48] and pressure.[49] NV centres have also been used in the study of fundamental quantum physics, by performing a loop-hole free Bell test.[50,51]

1.2 Addressing single atoms in silicon transistors

The increasing knowledge about defect centres and the improved control over the concentration of impurities in semiconductors allowed for the first operational n-p-n transistors in 1951.[52] In the decades to follow, the accuracy in the doping of silicon substrates, with both n-type donor atoms and p-type acceptor atoms, drove the exponential miniaturisation of transistor technology and thereby the exceptional growth of the semiconductor industry. In the last decade this continuous miniaturisation has reduced the size of the transistors to the point where the conductive properties are governed by about a hundred dopant atoms,[53] as shown in Fig. 1.2a.

Around ten years ago, the downscaling of the widely used metal-oxide-semiconductor field-effect transistor (MOSFET) through advancements in

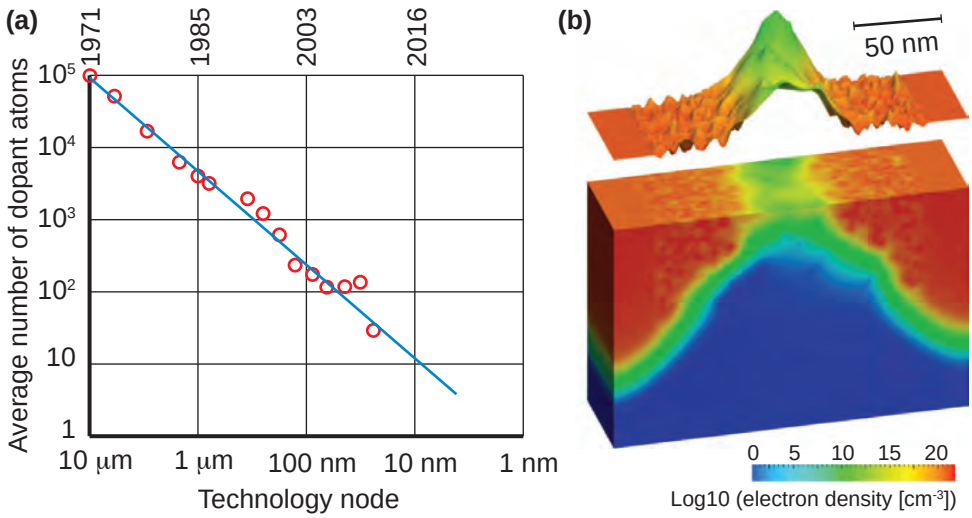

Figure 1.2: Random discrete doping in the semiconductor industry. **(a)** The average number of dopant atoms in the transistor channels of the different Intel technology nodes over time. The visible plateau around ∼100 dopant atoms shows the limiting effect of the random discrete doping distribution. Image adapted from reference.[53] **(b)** Simulation of the electron density in a 35-nm long transistor channel, illustrating the strong effect of the random placement of dopants on the transistor profile. Image adapted from reference.[54]

lithography techniques, reached fundamental limits. At that time, the small number of dopants controlling the operation of the transistor, shown in Figs. 1.2a and b, led to an increasing variability between transistors, due to the effect of discrete random dopant fluctuations. As a result of this variability, and to keep all transistors operational, the tight bounds of on- and off-voltages needed to be alleviated, leading to an undesirable higher power consumption.

Improved gate control over the channel barrier could cutback the need for doping control. However, an increase in gate capacitance requires a reduction of the thickness of the gate-oxide, which also met a fundamental limit set by the gate leakage through the oxide, due to the quantum tunneling effect. A solution to these problems was found in the form of high-κ dielectric materials, replacing the silicon dioxide, in combination with metal gates. This increase in gate control, eliminated for a large part the variability effect of the discrete random dopant distributions. Further improvements in gate-control were achieved by wrapping the gate around the transistor channel, leading to new transistor technologies, such as fin field-effect transistors (FinFETs), tri-gate transistors, and gate all around (GAA) transistors. The transition away from doping controlled transistors is visible in Fig. 1.2a as a sharp decline in number

of dopant atoms used in the 45 nm technology node of Intel.

Although the placement of discrete dopant atoms in sub-100 nm transistors formed a challenge for the semiconductor industry, it also offers an opportunity to use these devices to study the behavior of single dopant atoms. The signature of a single arsenic atom in a silicon transistor was first observed in resonant tunneling transport spectroscopy in 2006.[27] Thereafter, the same measurement technique was used to study a variety of impurity atoms in silicon transistors, like boron,[28] phosphorus,[55] and platinum.[56] Further studies showed the effect of a nearby interface on a single atom,[57] the determination of the location of a single atom,[58] and the effect of the single atom on the room temperature behavior of the transistor.[59]

1.3 This thesis

In this work the dynamics of single atoms in silicon was studied using state of the art silicon nanowire transistors. The main focus of this thesis is the study of individual boron atoms in silicon, see Fig.1.1c. Holes bound to these boron atoms have a strong spin-orbit coupling, which makes these acceptor atoms promising candidates to create electrically controllable qubits. The energy and total angular momentum of the acceptor eigenstates are strongly dependent on the environment of the atom, such as the electric and magnetic field, strain and the proximity to an interface. Due to this sensitivity to the surroundings, a large inhomogeneous broadening is found in most measurements on acceptor atom ensembles, which has restricted experiments to strictly controlled environments, such as zero strain and zero electric field. The study of single boron atoms presented here, opens up the possibility to study the acceptor atom under different conditions, of which some have been indicated as favorable for spin-orbit qubits. Experiments on the spin-orbit dynamics of individual boron atoms are presented in this thesis as follows:

Chapter 2 describes the system of acceptor atoms in silicon. It starts with an overview of the known physical properties of boron atoms, based on ensemble measurements in bulk silicon. In the next section a theoretical framework of a single acceptor atom in silicon is given, which is used in the following section to describe two coupled acceptor atoms. Finally the potential of acceptor atoms in silicon to be used as qubits for quantum computing is discussed.

Chapter 3 outlines the transistor geometries and experimental techniques used in the measurements presented in this thesis. Two types of silicon

transistors were used in this work, and their characteristics are described in the first section of this chapter. This is followed by two sections discussing the experimental techniques of dc transport spectroscopy and rf gate reflectometry. The transport measurement technique is presented in terms of resonant hole tunneling for a single acceptor atom and two coupled acceptors. This is followed by a discussion of the effect of the hole tunneling on the reflection of a LC-circuit in the rf gate reflectometry technique.

Chapter 4 presents the study of the electric and magnetic properties of single boron atoms in silicon transistors. The acceptor atom was identified by comparing the charging energy and excited state spectrum found in transport spectroscopy to the known bulk values. The magnetic properties of the fourfold degenerate ground state of the first hole bound to the acceptor atom were found by a systematic investigation of the Zeeman effect. This is followed by the study of the rotation of the magnetic field and the strength of the electric field on the Zeeman effect.

Chapter 5 describes the measurements on two coupled boron atoms in a silicon transistor. The identification of both boron atoms and a two-hole system were demonstrated by rf gate reflectometry measurements of an avoided crossing in the charging of a single acceptor. A singlet-triplet transition was identified by the measurement of Pauli spin blockade. This was used to investigate the heavy-light hole relaxation processes, which are dominant in this two-hole system, and the mixing between the heavy and light hole states. Further insights into the origins of the heavy-light hole mixing was given by the analysis of the two-hole excited state spectrum found in magneto-transport spectroscopy.

Chapter 6 demonstrates the resulting effects of microwave radiation on a single acceptor atom and coupled acceptor atoms. The first section shows the measurement of a coherent excitation of the two-hole system, as described in chapter 5, from a bonding to an antibonding heavy hole singlet state. Next, the coherent interference in a Landau-Zener-Stückelberg configuration, demonstrated for a single acceptor atom, is presented. Finally, the effect of photon-assisted tunneling on the transport spectroscopy measurements of acceptor states is discussed.

Chapter 7 explains the dynamics of single-atom electron pumps. The possibility to use a single atom, embedded in a silicon double-gate transistor, to periodically transfer single electrons was theoretically investigated. Analysis of the effects of the charge dynamics on the accuracy of these devices shows a strong dependence on the orbital relaxation rates of the atom. The first

section gives an overview of the important progress in the field of quantum metrology based on single electron pumps. This is followed by a theoretical framework developed here to describe an electron pump using the coulomb potential of a single phosphorus atom to trap electrons. Simulations of the operation and accuracy of this single-atom electron pump were compared with recent experimental results and used to investigate the feasibility of such a charge pump.

A conclusion of this thesis is presented in **chapter 8**, along with an outlook of potential further research directions.

chapter 2

Acceptor atoms in silicon

To support the experiments on the dynamical behavior of single acceptor atoms in silicon, this chapter summarizes prior theoretical and experimental studies of acceptors in silicon. Most of the experimental studies were performed on ensembles of boron atoms in bulk silicon, but recent studies performed on single acceptors are also included. Furthermore, a theoretical framework describing the single acceptor and coupled acceptors in silicon is presented in this chapter. Finally, the use of acceptor atoms for quantum computation is discussed.

2.1 Shallow acceptors in silicon

Boron doped silicon is the most used p-type semiconductor in the CMOS technology and therefore boron is by far the most researched acceptor in silicon. In this chapter the general theory of shallow acceptors is discussed, where all specific values are given for boron atoms, as these acceptor atoms were used in the experiments presented in the chapters 4, 5, and 6.

The band structure of silicon, as shown in Fig. 2.1a, has an indirect bandgap of around 1.1 eV. The top of the valence band is found at the Γ-point ($|\mathbf{k}|$=0), while the bottom of the conduction band is positioned at $|\mathbf{k}| = 0.85k_0$ towards the X-point ($|\mathbf{k}| = k_0$). Because the conduction band minimum is not located at the Γ-point, a total of six minima, called valleys, are found in the (100) and equivalent directions. The physics arising from the valley degree of freedom in silicon has been the topic of many studies as it has a strong impact on the implementation of a bound electron as a quantum two-level system.[60] The spin-orbit interaction is minimal in the conduction band of silicon,[17] which is one of the main reasons for the remarkably long coherence times achieved for electrons in silicon. Another reason is the relatively low amount of the nuclear spin carrying isotope ^{29}Si in natural silicon (around 5%), which are sources of random magnetic field fluctuations. The isotope purification to ^{28}Si leads to even longer coherence times for both the electron and nuclear spin.

In contrast to the conduction band, a strong spin-orbit interaction is present

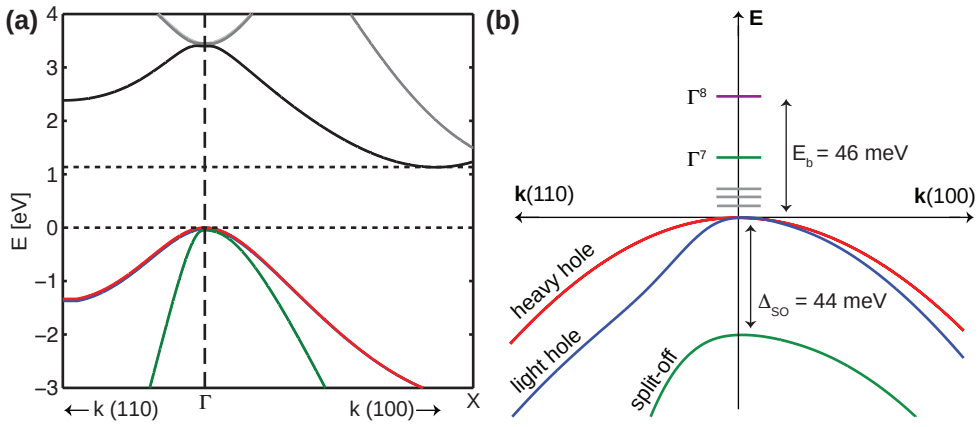

Figure 2.1: Silicon band diagram. **(a)** Part of the band structure of silicon, showing the valence band maximum at the Γ-point and the conduction band minimum at $|\mathbf{k}| = 0.85k_0$. The three bands at the top of the valence band are the heavy hole band (red), the light hole band (blue) and the split-off hole band (green). **(b)** Detailed energy diagram of the top of the valence band, with atomic levels of a boron atom in the band gap.

for holes in the valence band of silicon. The valence band state is p-type (**l**=1), where the two bands at the top of this band carry a total angular momentum of **j**=3/2, with the heavy hole ($m_j = \pm 3/2$) and the light hole ($m_j = \pm 1/2$) bands degenerate at the Γ-point. These bands are separated from the **j**=1/2 split-off band due to the spin-orbit interaction. In silicon this splitting Δ_{SO} is 44 meV,[61] as shown in Fig. 2.1b.

The single hole states of an acceptor are build from the different valence bands, and in bulk silicon the degeneracy between heavy and light holes is preserved in the acceptor ground state, as the spherical symmetric confinement of the atom does not break the cubic silicon symmetry. The energy transitions from the acceptor ground state to the higher lying excited states and the valence band were first investigated by infrared photo-absorption measurements.[62,63] The binding energy of the ground state, which has a fourfold degenerate Γ_8 symmetry, was found to be 46 meV. The first excited state, 23 meV away from this ground state, has a twofold degenerate Γ_7 symmetry, coming from the split-off band. This state was first detected by electronic Raman scattering experiments.[64] Although recent experiments have questioned the binding energy of this state,[65] the original value was confirmed by a combination of electronic Raman scattering, acceptor bound-exciton spectroscopy, and infrared absorption measurements.[66]

The calculation of the energy spectrum of acceptors in silicon was first given by Schechter,[67] following the effective mass approximation introduced by Kohn and Luttinger for donors in silicon.[68] Furthermore, a complete theoretical description of the energy spectrum using a spherical approximation of the atom was given by Baldereschi and Lipari[69,70] and an overview of the measured binding energies of these states is given by Ramdas and Rodriguez.[71]

2.2 Splitting of the acceptor ground state

2.2.1 Zeeman effect

The fourfold degeneracy of the acceptor ground state is lifted by an external magnetic field. The magnetic field part of the Hamiltonian ($\mathbf{H'_B}$) for the spin-orbit states of holes in semiconductors was first given by Luttinger[72] and formulated for acceptor atoms by Bir et al.:[73]

$$\mathbf{H'_B} = g'_1 \mu_B \left\{ J_x B_x + J_y B_y + J_z B_z \right\} + g'_2 \mu_B \left\{ J_x^3 B_x + J_y^3 B_y + J_z^3 B_z \right\}, \quad (2.1)$$

where B is the magnetic field and μ_B is the Bohr magneton, given by $e\hbar/2m_e$. g'_1 and g'_2 are the linear and cubic part of the Landé g-factor respectively and

the matrices J_x, J_y, and J_z are given by:

$$J_x = \frac{i}{2}\begin{bmatrix} 0 & \sqrt{3} & 0 & 0 \\ -\sqrt{3} & 0 & 2 & 0 \\ 0 & -2 & 0 & \sqrt{3} \\ 0 & 0 & -\sqrt{3} & 0 \end{bmatrix}, \tag{2.2}$$

$$J_y = \frac{1}{2}\begin{bmatrix} 0 & \sqrt{3} & 0 & 0 \\ \sqrt{3} & 0 & 2 & 0 \\ 0 & 2 & 0 & \sqrt{3} \\ 0 & 0 & \sqrt{3} & 0 \end{bmatrix}, \tag{2.3}$$

$$J_z = \frac{1}{2}\begin{bmatrix} 3 & 0 & 0 & 0 \\ 0 & 1 & 0 & 0 \\ 0 & 0 & -1 & 0 \\ 0 & 0 & 0 & -3 \end{bmatrix}. \tag{2.4}$$

The Zeeman Hamiltonian can be further extended with a quadratic term in magnetic field, as discussed by Bhattacharjee and Rodriguez.[74] However, this term is negligible for boron atoms in silicon[75] and therefore omitted here.

Observing the Zeeman splitting without any perturbation due to strain or electric field, takes a great effort in sample preparation. The first electron paramagnetic resonance measurements on zero-strain boron doped silicon samples were performed by Neubrand,[78,83] followed by acoustic paramagnetic resonance[82] and dielectric resonance[75] measurements. Recently electron paramagnetic resonance measurements have been performed on purified ^{28}Si

Table 2.1: Linear and cubic g-factors for boron in silicon as reported in several studies based on electron paramagnetic resonance,[76–79] Raman scattering,[80] photoabsorption,[81] acoustic paramagnetic resonance,[82] and dielectric resonance[75] experiments.

Reference	g'_1	g'_2	ratio g'_2/g'_1
Feher et al.,[76] calculated by Bir et al.[73]	1.21	0.002	0.2%
Cherlow et al.[80]	0.84	0.13	15.5%
Shimizu and Tanaka[77]	1.048	0.061	5.8%
Merlet et al.[81]	1.03	0.04	4%
Neubrand[78]	1.0676	0.0317	2.97%
Zeile and Lassmann[82]	1.067	0.037	3.5%
Köpf and Lassmann[75]	1.070	0.033	3.1%
Stegner et al.[79]	1.0728	0.0315	2.94%

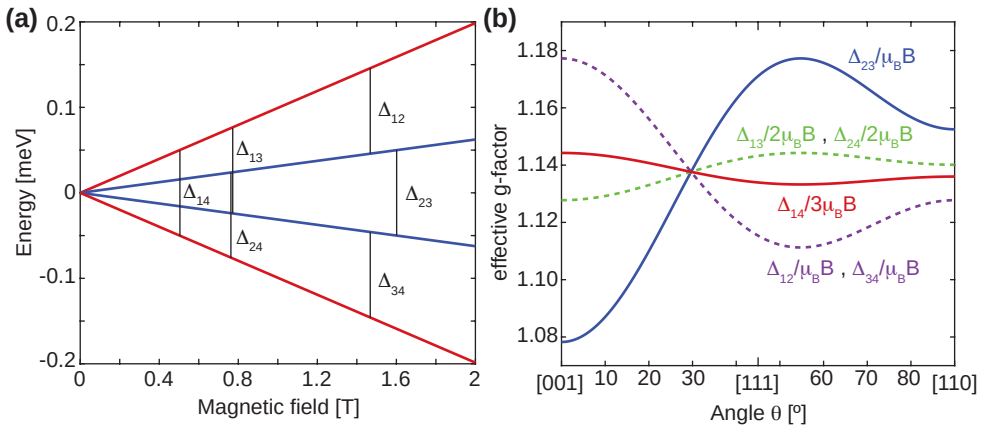

Figure 2.2: Zeeman effect. **(a)** Energy dependence of the acceptor ground state as a function of an external magnetic field applied in the [001] direction, without external strain or electric field. **(b)** Anisotropy of the g-factor in the $(1\bar{1}0)$-plane given by Eq. 2.5, where the splitting between the different states is divided by $\Delta m_j \mu_B B$ to find an effective g-factor.

samples,[79] which resolve the effect of the different silicon isotopes on the boron resonance. The observed resonances in these experiments depend on the angle between the applied magnetic field and the crystallographic axis. When the magnetic field is rotated in the $(1\bar{1}0)$-plane, starting from the [001] direction, reaching the [111] direction at 45° and [110] at 90°, the total Zeeman energy is given by:[78,84]

$$\mathbf{E_Z}(\theta) = m_j \mu_B |B| \left\{ g_1' + g_2' \left(\frac{41}{20} + \left[m_j^2 - \frac{41}{20} \right] \left(1 - 5sin^2\theta + \frac{15}{4} sin^4\theta \right) \right) \right\} \quad (2.5)$$

For all group III acceptors in silicon it is found that $g_1' \gg g_2'$,[75] and for boron g_1' and g_2' are around 1.07 and 0.03 respectively. An overview of values of g_1' and g_2' measured for boron atoms in silicon is given in table 2.1. Using the values found by Köpf and Lassmann, the Zeeman splitting of the ground state is shown in Fig. 2.2a. The splitting between the different states as a function of the angle between the magnetic field and crystallographic axis is expressed in effective g-factors, shown in Fig. 2.2b.

2.2.2 Effects of strain and electric field

Although the degeneracy of the heavy and light hole states is preserved in an unstrained silicon crystal, a perturbation of the atomic Coulomb potential by strain or electric field lifts this degeneracy. The effect of strain is given by the

Bir-Pikus strain Hamiltonian[73] ($\mathbf{H}'_\epsilon$), which is written as:

$$\begin{aligned}\mathbf{H}'_\epsilon = a'\epsilon I + b'\left\{\left(J_x^2 - \frac{5}{4}I\right)\epsilon_{xx} + \left(J_y^2 - \frac{5}{4}I\right)\epsilon_{yy} + \left(J_z^2 - \frac{5}{4}I\right)\epsilon_{zz}\right\} \\ + \frac{2d'}{\sqrt{3}}\left\{[J_xJ_y]\,\epsilon_{xy} + [J_xJ_z]\,\epsilon_{xz} + [J_yJ_z]\,\epsilon_{yz}\right\},\end{aligned} \tag{2.6}$$

where I is the identity matrix and a', b', and d' are the deformation potential constants for boron atoms in silicon, whose values have been experimentally established.[78,80] As can be seen from this Hamiltonian, strain will mix the heavy and light hole states and is expected to lift the degeneracy of these states. This explains why the presence of a random strain in a bulk silicon sample leads to an inhomogeneous broadening of the linewidth in resonance experiments. In the earliest electron paramagnetic resonance measurements the resonance only became visible when a large homogenous strain was applied to the sample in order to split the heavy and light hole states thereby diminishing the mixing between them.[76] Zero external-strain resonance measurements became possible when the defect density in silicon samples decreased enough to suppress the inhomogeneous broadening,[78] where the measured residual linewidth originated from the random strains introduced by carbon and oxygen defects.[83] Recently it has been shown that a further reduction of the resonance linewidth can be achieved by isotopically purifying the silicon to ^{28}Si.[79,85] The broadening caused by the different isotopes is explained by the local fluctuations of the valence band edge at the positions of the isotopes.[86]

The effect of an applied electric field, described by Bir et al.,[87], can be separated in three Hamiltonians. In the diamond cubic crystal structure of silicon, which has an octahedral $O_h = T_d \times I$ symmetry, only terms quadratic in electric field add to the Hamiltonian, given by:

$$\begin{aligned}\mathbf{H}'_{E^2} = \alpha' E^2 I + \beta'\left\{J_x^2E_x^2 + J_y^2E_y^2 + J_z^2E_z^2 - \frac{5}{4}IE^2\right\} \\ + \frac{2\delta'}{\sqrt{3}}\left\{[J_xJ_y]\,E_xE_y + [J_xJ_z]\,E_xE_z + [J_yJ_z]\,E_yE_z\right\},\end{aligned} \tag{2.7}$$

where α', β', and δ' are the coupling constants for these quadratic terms, and are estimated by Bir et al. using the effective mass approximation.[87] The presence of the acceptor atom breaks the inversion symmetry of the silicon crystal, which reduces the symmetry close to the atom to tetrahedral T_d, thereby adding terms linear in electric field ($\mathbf{H}'_\mathbf{E}$) and products of electric and magnetic field ($\mathbf{H}'_\mathbf{EB}$), given by:

$$\mathbf{H}'_\mathbf{E} = \frac{p_{\text{eff}}}{\sqrt{3}}\left\{E_x\,[J_yJ_z] + E_y\,[J_xJ_z] + E_z\,[J_xJ_y]\right\}, \tag{2.8}$$

$$\begin{aligned}\mathbf{H'_{EB}} &= \gamma'_1 \left\{ J_x \left[E_y B_z \right] + J_y \left[E_z B_x \right] + J_z \left[E_x B_y \right] \right\} \\ +\gamma'_2 &\left\{ J_x^3 \left[E_y B_z \right] + J_y^3 \left[E_z B_x \right] + J_z^3 \left[E_x B_y \right] \right\} + \frac{2\gamma'_3}{\sqrt{3}} \left\{ \mathbf{V} \left[\mathbf{E} \times \mathbf{B} \right] \right\},\end{aligned} \tag{2.9}$$

where $\mathbf{V}$ is given by $V_x = \left[J_x \left(J_y^2 - J_z^2 \right) \right]$ and its cyclic permutations of x, y, and z. Furthermore, p_{eff} is the effective electric dipole moment for the linear electric field coupling and γ_1, γ_2, and γ_3 are the coupling constants between the electric and magnetic field, also estimated by Bir, Butikov, and Pikus.[73] The linear Stark coupling given by Eq. 2.8 was measured for different acceptors in silicon by Köpf and Lassmann, giving a value of p_{eff} of 0.26 ± 0.06 Debye for boron acceptors,[75] where 1 Debye is equal to $1/(1 \cdot 10^{-21} c)$ Cm with c the speed of light in vacuum, which is around 0.021 e·nm.

As mentioned before, the linewidths observed in resonance experiments on ensembles of acceptor atoms in silicon regularly show an inhomogeneous broadening due to random local perturbations, such as strain, electric field, and the random distribution of isotopes. This is the reason why in ensemble measurements the properties of acceptor atoms have only been measured in the extreme experimental conditions of either a light-heavy hole splitting far exceeding the Zeeman splitting ($\Delta_{LH} \gg E_Z$) or in the vicinity of zero light-heavy hole splitting ($\Delta_{LH} \sim 0$). However a condition of small strain or electric field, such that the light-heavy hole splitting is of the order of the Zeeman splitting ($\Delta_{LH} \sim E_Z$), has so far been inaccessible as a large inhomogeneous broadening is expected due to the strong mixing of heavy and light holes in this regime. Furthermore, the inhomogeneous broadening in the resonance measurements makes it difficult to detect any spin dynamics of the acceptor atoms.

Inversely, the study of a single acceptor atom allows to probe its local environment. Experiments on single acceptors in silicon Shottky barriers, have shown both the linear Stark effect[28] and the effect of local strain.[88] Scanning tunneling spectroscopy experiments have shown the effect on the splitting of the acceptor ground state created by the perturbation caused by a nearby interface.[89] The experiments presented in this thesis show a detailed study of the Zeeman splitting of the ground state of a single boron atom (chapter 4) and the first investigation of the spin dynamics of a single acceptor by the study of the quantum states of two holes bound to two coupled boron atoms (chapter 5).

2.3 Coupled acceptor atoms

In this section the description of the single acceptor atom is extended to two coupled acceptor atoms. In particular, the system of two holes bound to two boron atoms is discussed, where the case of having each hole located on a different acceptor is compared with the case where both holes are bound to the same acceptor atom.

2.3.1 Two holes bound to two acceptors

First, the case of two holes bound to two acceptor atoms is discussed in the situation where this system is far detuned from the resonance points where one hole can tunnel to the other acceptor. In this case the two-hole state can simply be described as a product state of the single particle states. For each acceptor atom the mixing between the heavy and light hole states and the splitting between these states (Δ_{LH}) are defined by the local environment, which is taken to be different for each acceptor. Although in general the hole states are mixtures of heavy hole and light hole states, the predominantly heavy hole states will be referred to with "H" and the predominantly light hole states will be referred to with "L". The states are written as $\psi^n_{X\pm}$, with energies $E^n_{X\pm}$, where n denotes either the first ($n = 1$) or the second ($n = 2$) acceptor and X denotes the predominantly heavy ($X = H$) or light ($X = L$) holes. The light-heavy hole splittings of the acceptors at zero magnetic field are then defined as:

$$\Delta^{1(2)}_{LH} = E^{1(2)}_{L\pm} - E^{1(2)}_{H\pm}. \tag{2.10}$$

The two-hole energy spectrum can be described by the product states of the two single particles, leading to an energy spectrum of 16 states divided into 4 fourfold degenerate manifolds at zero magnetic field. If both $\Delta^1_{LH} > 0$ and $\Delta^2_{LH} > 0$, the lowest energy manifold, consisting of two heavy holes, is found at $E^1_{H\pm} + E^2_{H\pm}$. The two fourfold manifolds consisting of one heavy hole and one light hole are Δ^1_{LH} and Δ^2_{LH} higher in energy, while the states build from two light holes are $(\Delta^1_{LH} + \Delta^2_{LH})$ higher in energy. Each fourfold manifold splits into a singlet and a triplet state when an exchange interaction is introduced, similar to the case of two-electron systems. For the heavy hole

manifold, this is written as:

$$\begin{aligned} S_{HH} &= \frac{1}{\sqrt{2}}\ \left([\Uparrow,\Downarrow] - [\Downarrow,\Uparrow]\right), \\ T^{-}_{HH} &= [\Downarrow,\Downarrow], \\ T^{0}_{HH} &= \frac{1}{\sqrt{2}}\ \left([\Uparrow,\Downarrow] + [\Downarrow,\Uparrow]\right), \\ T^{+}_{HH} &= [\Uparrow,\Uparrow], \end{aligned} \tag{2.11}$$

where $[i,j]$ represents the spin state i of acceptor 1 and spin state j of acceptor 2, and predominantly heavy holes are represented by a double arrow ($\Downarrow$ or $\Uparrow$), while predominantly light holes are represented by a single arrow ($\downarrow$ or $\uparrow$).

2.3.2 Two holes bound to one acceptor

The two holes are found to be bound to the same acceptor in the coupled acceptor system when the potential landscape is tilted far enough to one side. This doubly occupied and positively charged acceptor state (A^+) has an exchange energy much larger than the Δ_{LH} of this acceptor. Due to this exchange energy, only 6 out of the 16 possible two-hole states can be bound to a single boron atom in silicon.[90] These six states are similar to the states found for two-holes bound to two closely placed boron atoms[91] and the neutral states of two holes bound to group II acceptors.[74,92] Each state is build from a linear combination of two different spin states, which leads to one possible HH-singlet state, one possible LL-singlet state and four possible LH-quadruplet states. These are all separated by the light-heavy hole splitting Δ_{LH}, which again is assumed positive:

$$S_{HH} = \frac{1}{\sqrt{2}}\ \left([\Uparrow\Downarrow] - \Downarrow\Uparrow]\right), \tag{2.12}$$

where $[ij]$ now represents the spins i and j of the two holes bound to the single acceptor. The LH-quadruplet states are Δ_{LH} higher in energy:

$$\begin{aligned} Q^{--}_{LH} &= \frac{1}{\sqrt{2}}\ \left([\Downarrow\downarrow] - [\downarrow\Downarrow]\right), \\ Q^{-}_{LH} &= \frac{1}{\sqrt{2}}\ \left([\Downarrow\uparrow] - [\uparrow\Downarrow]\right), \\ Q^{+}_{LH} &= \frac{1}{\sqrt{2}}\ \left([\Uparrow\downarrow] - [\downarrow\Uparrow]\right), \\ Q^{++}_{LH} &= \frac{1}{\sqrt{2}}\ \left([\Uparrow\uparrow] - [\uparrow\Uparrow]\right). \end{aligned} \tag{2.13}$$

And the LL-singlet state is another Δ_{LH} higher in energy:

$$S_{LL} = \frac{1}{\sqrt{2}}\ \left([\uparrow\downarrow] - [\downarrow\uparrow]\right). \tag{2.14}$$

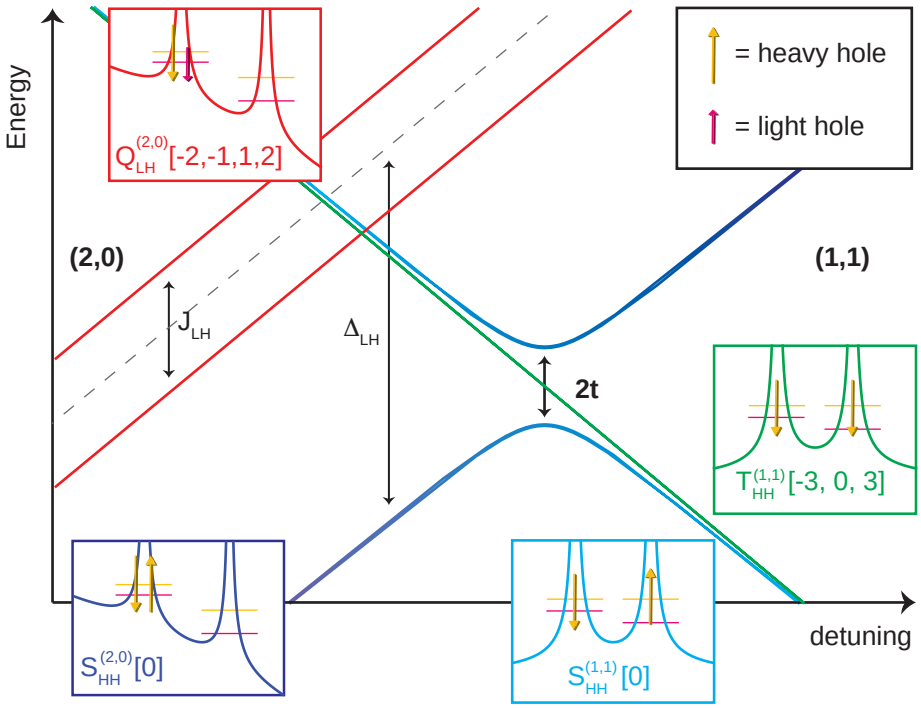

Figure 2.3: Coupled acceptor energy versus detuning diagram. On the left hand side the system of two holes coupled to one acceptor is shown. On the right hand side the two holes are bound to one acceptor each. The relevant energy of the tunnel coupling (t), the light-heavy hole splitting (Δ_{LH}) and the light-heavy hole exchange (J_{LH}) are indicated. In the insets the relevant potential diagrams and the total angular momentum of the two-hole states is shown, where pure heavy ($m_j = \pm 3/2$) and light ($m_j = \pm 1/2$) hole states are assumed.

Furthermore, when an exchange interaction, J_{LH}, between the heavy and light holes is introduced, the Q_{LH} states splits into a singlet and triplet state.[93] Taking the states given in Eqs. 2.11, 2.12, and 2.13 the energy diagram of the two hole system is schematically drawn in Fig. 2.3. Here the states where each acceptor has one hole bound to it are referred to as (1,1) (right side of the figure) and the states where two holes are bound to one acceptor are referred to as (2,0) (left side of the figure). Only the heavy hole singlet state is drawn for both the (1,1) and (2,0) state, and a tunnel coupling between the acceptors leads to a mixing of these states when brought into resonance. Although a finite mixing is also present between most other (1,1) and (2,0) states, these transitions require a change of the spin-state. Therefore these anti-crossings are expected to be smaller than the one shown for the heavy hole singlet state, and omitted in the schematic drawing in Fig. 2.3.

2.4 Acceptor atoms for quantum computation

Recently, a number of single defects in semiconductors have shown to possess robust quantum two level systems, which have emerged as promising candidates to form a basis for quantum computing. Specifically the spin states of negatively charged nitrogen-vacancy defect centres (NV^-) in diamond and neutral phosphorus donors (D^0) in silicon have been demonstrated to have characteristics desirable for quantum bits (qubits).

The NV^- centres in diamond are of particular interest as they can be initialized, manipulated and readout at room temperature using optical techniques, as shown in Fig. 1.1a. Many important steps towards operable qubits have been demonstrated, such as coherent control and readout of the qubit,[94] coherent coupling between two spins,[95] and reliable fabrication techniques using ion implantation.[96,97]

Phosphorus atoms in silicon are very promising for quantum computing because of their long coherence time, especially when the effect of a random fluctuating magnetic fields is minimized by purifying the silicon to the zero-spin ^{28}Si isotope. These donor atoms can be electrically initialized and read-out, while the spin-state can be manipulated with an oscillating magnetic field, as shown in Fig. 1.1b. The essential steps of qubit readout,[98] coherent qubit control,[39,99,100], and atomically precise fabrication of devices[41] have been accomplished at the single-donor level.

Acceptor atoms in silicon exhibit a strong spin-orbit interaction between light and heavy holes, in contrast to the negligible spin-orbit coupling found for donor bound electrons in silicon.[17] This gives the possibility to create spin-orbit qubits with single acceptors, which can be controlled with oscillating electric fields, as shown in Fig. 1.1c, while maintaining the beneficial properties of the silicon material as a host semiconductor.

2.4.1 The spin-orbit qubit

The coupling of spin degrees of freedom to oscillating electric fields has the potential to boost the prospects of scalability for spin qubits. In particular, electric field control enables fast, local single-qubit operations,[101,102] where the oscillating field can be applied using the electrostatic gates already in place to control the energy of the qubit levels or readout the spin state of the qubit. This minimizes the number of gates needed to operate a spin qubit, which is essential for future many-qubit architectures. Furthermore, a strong interaction with electric fields allows the coupling of spin qubits to photons

in microwave resonators, which allows for long-range coupling of qubits via circuit quantum electrodynamics.[103,104] Coupling of spins to electric fields has recently been realized via spin-orbit coupling in III-V based, gate-defined electron[102,105] and hole[106] quantum dots.

The intrinsic spin-orbit coupling between the heavy and light hole states of acceptor atoms in silicon, has given rise to several proposals of acceptor spin-orbit qubits.[93,107–109] Each proposal defines a different local environment of the acceptor atoms as favorable to achieve certain qubit qualities, such as fast Rabi oscillations through a strong dipole coupling or long relaxation and coherence times through weak interactions with phonons. These works suggest that with a precise control over the local environment of the acceptor atom, the acceptor properties can be drastically changed, producing a particularly highly tunable quantum two-level system.

In the proposal of Ruskov and Tahan,[107] a zero-strain acceptor qubit is proposed, as shown in Fig. 2.4a, where the two lowest energy states are a heavy hole and a light hole state. It is suggested to manipulate these states with phonons in a nanomechanical cavity. In the proposals of Salfi et al.,[93,109] the complex local environment of the acceptor creates either two light hole or two heavy hole states as the two lowest energy states. For the light hole qubit, as shown in Fig.2.4b, rapid manipulations with a rotating electric field are predicted due to a strong dipole coupling, while the qubit stays insensitive

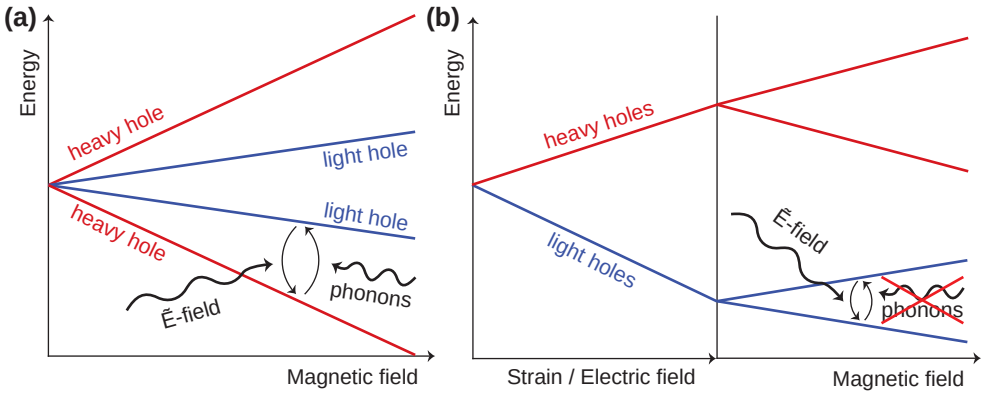

Figure 2.4: Acceptor qubit schemes. **(a)** Zero-strain acceptor levels, as also shown in Fig. 2.2a, where the lowest heavy and light hole states can be operated as an electrically driven or phonon driven spin-orbit qubit. **(b)** Acceptor levels when strain or electric field splits the heavy and light holes. In this example the light hole states can be used as an electrically driven spin-orbit qubit, which is to first order protected from gate noise[93] and interactions with phonons.[107]

to electrical gate noise in first order.[93]

2.4.2 Relaxation and coherence times

The most important parameters to evaluate the potential of a quantum two level system for quantum computing are the time it takes to manipulate the system, set by the Rabi frequency, and the coherence time T_2 of the system. An upper bound for the coherence time is given by the relaxation time T_1 of the system, where $T_2 \leq 2T_1$. For acceptor atoms in silicon T_2 is expected to be close to this upper bound,[93,107,108] as the decoherence from other sources are predicted to act on longer time scales. This includes the decoherence from gate noise, from the charging and discharging of nearby charge traps (assuming a trap density below $10^{15} cm^{-3}$), and from magnetic field noise through the hyperfine coupling to nuclear spins in the lattice.[93] The hyperfine coupling of holes, expected to be smaller than for electrons due to the p-symmetry of the atomic orbitals, was confirmed by measurements on quantum dots.[110] Furthermore, silicon can be isotopically purified to ^{28}Si to drastically reduce the number of nuclear spins in the lattice.

The relaxation time of the acceptor system depends strongly on the local environment of the acceptor. In the zero-strain acceptor case, as shown in Fig. 2.4a, the relaxation time at low temperature for a magnetic field applied in the [001] direction is given by the phonon spontaneous emission rate:[93,107]

$$\frac{1}{T_1} = \frac{(\hbar\omega)^3}{20\pi\rho\hbar^4} 2d'^2 \left(\frac{1}{v_t^5} + \frac{2}{3v_l^5} \right), \tag{2.15}$$

where $\hbar\omega$ is the energy splitting between the lowest two acceptor levels, the heavy and light hole state, set by the Zeeman energy. ρ is the mass density, d' is a deformation potential constant as given in Eq. 2.6, and v_t and v_l are the transverse and longitudinal sound velocities in silicon (v_l = 9.0 10^5 cm/s, v_t = 5.3 10^5 cm/s).[107] In the case where the heavy hole and light hole manifold are split, such as shown in Fig. 2.4b, the phonon relaxation rate within the lower manifold depends on the coupling to the upper manifold, which strongly depends on the electric field.[93,107] This rate has an extra quadratic dependence on the energy splitting,[93] which gives $\frac{1}{T_1} \sim (\hbar\omega)^5$. For the qubit proposed by Salfi et al.,[93] the relaxation time is about 100 times longer than the zero-strain acceptor relaxation time.

Only few measurements of the coherence and relaxation time of acceptor atoms in silicon have been reported. A 'no external strain' EPR measurement has been reported by Song and Golding,[111] where a T_2 of 2.6 μs and a T_1 of

7.4 μs were found. Furthermore, an intentionally strained boron doped silicon sample was probed with a pulsed EPR hole burning experiment by Dirksen et al.,[112] where a maximum T_1 of $\sim$ 80 ms was reported. This T_1 shows a quadratic dependence on the applied strain, as expected for the splitting between the light and heavy hole manifolds. Relaxation from the higher orbital excited states of acceptors around 60 ps have been measured.[65,113]

The experiments presented in chapter 5 of this thesis show the first relaxation measurements on single acceptor atoms and the first magnetic field dependence of the relaxation rate. The relaxation rate found in this magnetic field dependent measurement shows a light to heavy hole relaxation rate with a $(\hbar\omega)^3$ dependence.

2.5 Conclusion

This chapter has introduced the effect of a magnetic field, electric field and strain on a single acceptor as well as two-hole states bound to two acceptors. These descriptions were used to analyse the experiments shown in the following chapters. From the equations given in this chapter it follows that the specific local environment of an acceptor atom has a strong effect on the energy levels and their splitting in magnetic field. This commonly causes inhomogeneous broadening in resonance measurements on acceptor ensembles. Therefore measurements on single acceptor are important to the understanding of acceptor atoms, in particular to gain knowledge about the spin-orbit dynamics between the heavy and light hole states. Due to the spin-orbit coupling, the states of acceptor atoms in silicon are predicted to form electrically driven and highly tunable qubits.

chapter 3

Experimental background

This chapter provides background information about the experiments and data analysis presented in the following chapters. In the first section, the geometry and room temperature performance of the silicon transistors used in this work are presented. Then the single hole transport measurement technique is described, introducing transport through a single acceptor and two coupled acceptors. Finally, the radio frequency (rf) gate reflectometry measurement technique is introduced and the recent improvements of this technique are reviewed.

3.1 Silicon field-effect transistors

In this thesis several types of silicon transistors were used to study the dynamical behavior of single atoms. The main force behind the growth of the semiconductor industry over several decades has been the miniaturization of planar metal-oxide-semiconductor field-effect transistors (MOSFETs). These devices consist of different layers making up the semiconductor channel, a thin dielectric layer of oxide, and a metal gate layer on top. The downscaling of the planar MOSFETs became more challenging when the size of the transistors reached ~ 1 μm, where so-called short channel effects (SCE) start to influence the transistor performance.[114] The introduction of high-κ dielectric materials to replace the native silicon dioxide and multiple gate field effect transistors (MuGFETs) allowed for an improved gate control, which enabled the further miniaturization of the transistor. The transistors used in the experiments presented here make use of the high-κ dielectrics and multiple-gate layout. Several types of MuGFETs have recently been developed, which rely on including more than one gate-surface facing the silicon channel. These multiple gate surfaces are often contacted by a single electrode, wrapped around the silicon channel resulting in surfaces on three sides of the channel (see Fig. 3.1). Fin field-effect transistors (FinFETs) and tri-gate transistors, the transistor types used in this work, are examples of these type of MuGFETs, which are discussed in detail in the following sections. Alternatively, multiple gates can also be attached to different electrodes to get a more dynamical gate control over the channel. This type of MuGFET was used in the experiment presented in chapter 7, where a double gate FinFET is used to accurately control the movement of electrons in the transistor.

3.1.1 FinFET

To realize this work on single acceptor atoms, two types of transistors were used, which have similar design features with a gate nanowire wrapped around a silicon channel. The first type, which is referred to as FinFET in the thesis, has a fin-type channel, i.e. a greater height than width. These FinFETs were fabricated on a complementary metal-oxide semiconductor (CMOS) platform, using silicon on insulator (SOI) wafers, at the Interuniversity Microelectronics Center (IMEC) in Leuven, Belgium. The scanning electron microscope image of a typical FinFET, shown in Fig. 3.1a, illustrates the layout of the device, consisting of a silicon nanowire between a source and drain region around which a gate nanowire is wrapped. The gate stack consists of 5 nm TiN and

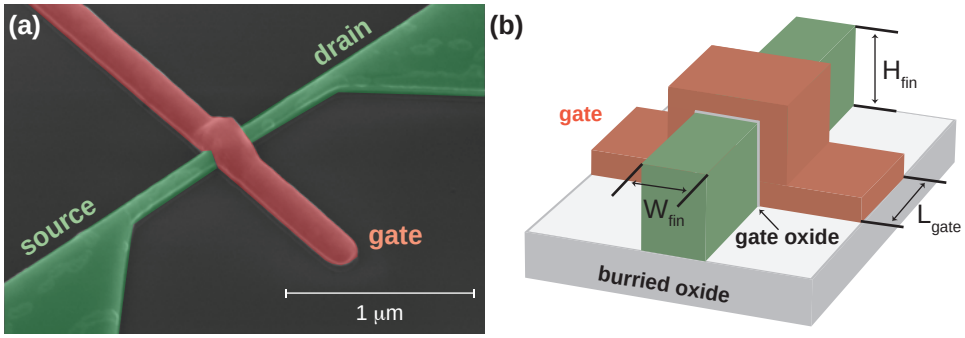

Figure 3.1: FinFET structure. **(a)** False color scale scanning electron microscope image of a FinFET, showing the silicon channel nanowire between source and drain, with a gate nanowire wrapped around it. This SEM image has been provided by IMEC. **(b)** Schematic representation of the FinFET, showing the notation used for the dimensions of the channel.

100 nm poly-silicon. An oxide layer of 1 nm SiO_2 and 2.3 nm HfSiO separates the gate from the silicon channel. On both sides of the gate 35 nm wide nitride spacers are fabricated, before doping the source and drain regions with a large concentration of boron atoms. The channel of the FinFET is undoped, but a few dopant atoms can diffuse into the channel.[115] The dimensions of the channel are given by the height and width of the fin, H_{fin} and W_{fin}, and the length of the gate, L_{gate}, as shown in Fig. 3.1b. The fin height of these FinFETs is 40 nm, while the fin width and gate length vary from device to device. More details about the fabrication can be found elsewhere.[116]

3.1.2 Tri-gate transistor

The second type of transistor used in the experiments is referred to as tri-gate transistor. Although the geometry also consists of a gate wrapped around a silicon channel, these transistors have a channel with a width larger than the height, making tri-gate a more fitting name. They are fabricated by the Laboratoire d'électronique et de technologie de l'information (Leti) in Grenoble, France, on a CMOS platform using 300 mm SOI wafers. The transistors used for this work have a channel height of 11 nm and a background doping of boron in the channel with a concentration of 5×10^{17} cm^{-3}. A gate stack of 5 nm TiN and 50 nm poly-silicon is placed on top of the oxide layer consisting of 0.8 nm SiO_2 and 1.9 nm HfSiO, as is shown in Fig. 3.2a. On both sides of the gate 25 nm wide SiN spacers are fabricated. The substrate of the SOI wafer, which is separated from the channel by 145 nm of buried oxide, can be used as an extra gate, called back gate in the experiments. Due to a relatively low

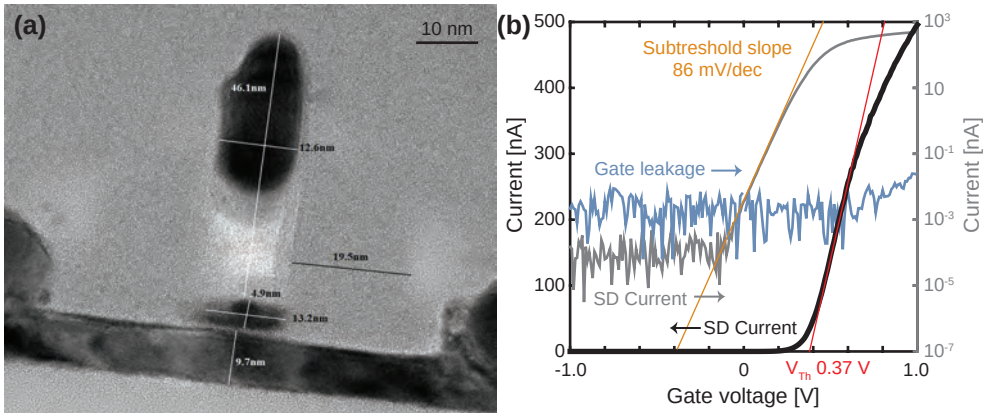

Figure 3.2: Tri-gate transistor. **(a)** Cut through the centre of the transistor, showing the measurements for a 12 nm long gate transistor. This TEM image has been provided by Leti. **(b)** Behavior of a typical tri-gate transistor with a gate length of 14 nm, channel width of 42 nm, and channel height of 11 nm, showing the source-drain current as a function of gate voltage on a linear and logarithmic scale, while also the gate leakage is shown on the logarithmic scale. A gate threshold voltage of 0.37 V and a subthreshold slope of 86 mV/dec were extracted.

boron doping concentration in the substrate of 5×10^{15} cm^{-3}, above-bandgap light was needed to induce charge carriers in the substrate in order to use it as a back gate at temperatures below 4.2 K.

Preliminary to the measurements at liquid helium temperatures shown in chapters 4 to 6, these transistors were characterized at room temperature. For these measurements a Cascade Microtech probing system was used and about 50 transistors with varying geometries were tested. These transistors were taken from the same wafer as the transistors used in chapters 5 and 6. The measurement of the transistor with a 42 nm wide and 14 nm long channel, shown in Fig. 3.2b, represents a typical room temperature performance. The measured source-drain current is shown as a function of gate voltage at a source voltage of 5 mV, both on a linear and on a logarithmic scale. The threshold voltage V_{Th} is defined as the zero-current crossing point of a linear fit to the linear part of the transistor current curve. The exponential decrease in current below the threshold voltage is visible on the logarithmic scale, and the reciprocal value of the slope of this decay is referred to as subthreshold swing. Additionally, the leakage current from the gate is measured and shown on the same logarithmic scale.

An overview of the characteristics of the probed set of transistors, with gate lengths and channel widths ranging from 10 nm to 10 μm and a fixed channel height of 11 nm, is shown in Figs. 3.3 and 3.4. The short channel

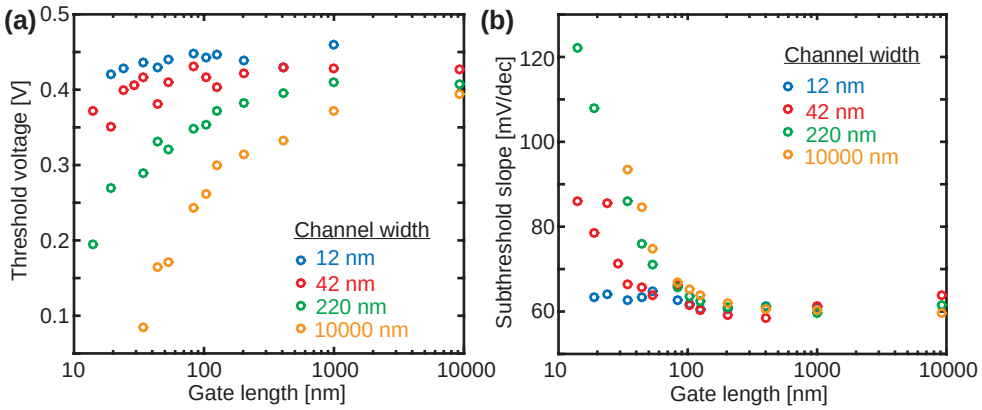

Figure 3.3: Threshold voltage and subthreshold slope. **(a)** The threshold voltage for a set of tri-gate transistors with different gate lengths, shown on the x-axis, and channel width, shown with different colors. **(b)** The subthreshold slope for the same set of transistors.

effect on the transistor behavior is found in the dependence of the threshold voltage and subthreshold swing on the gate length, as shown in Fig. 3.3. The threshold voltage, shown in Fig. 3.3a, is lower for transistors with a short gate length, which indicates that the threshold is not exclusively set by the work function of the gate. This reduced gate control is especially visible for the wide channel transistors. In contrast the tri-gate structure ensures a good gate-control for narrow channel transistors even when scaled down to lengths

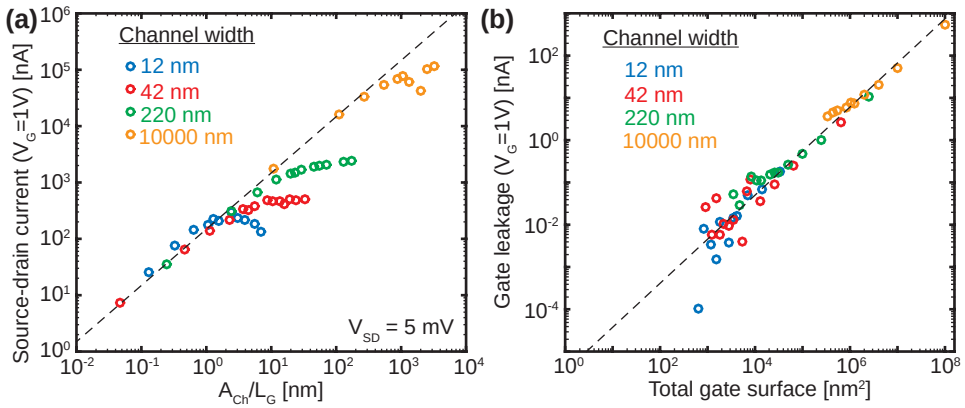

Figure 3.4: Source-drain current and gate leakage. **(a)** The source-drain current at 1 V gate voltage and 5 mV source-drain voltage for a set of tri-gate transistors with different gate lengths and channel widths, shown as a function of the cross section of the channel, A_{Ch}, divided by the gate length. The dashed line shows the resistivity of the open channel. **(b)** The gate leakage for the same set of transistors as a function of the total gate surface. A fit of the data reveals a gate leakage of 5×10^3 A/m^2, shown by a dashed line.

around 20 nm. The subthreshold swing, shown in Fig. 3.3b, has a similar dependence on gate length as the threshold voltage, as it is directly dependent on the gate control. The minimum subthreshold swing is bound by the thermal energy ($S_{s-th} > ln(10)k_BT/e$), which is about 60 mV/dec at 300 K. This lower bound of the subthreshold swing is reached for the longer transistors and down to the shortest gate lengths for the narrow channel transistors.

In Fig. 3.4a the source-drain current at a gate voltage of 1 V and a source-drain voltage of 5 mV is shown as a function of the cross section of the channel, divided by the gate length. The transistors with longer gates, which have reached the saturation region at 1 V, have a linear current behavior, indicating a resistivity of the open channel of 3×10^{-3} Ωcm. The transistors with smaller gate lengths do not have a completely open channel at a gate voltage of 1 V, instead a rise in the source-drain current is still visible at this gate voltage, see for example Fig. 3.2b. Fig. 3.4b shows the gate leakage as a function of the total gate surface surrounding the transistor. A clear linear behavior reveals a constant gate leakage of 5×10^3 A/m^2, and indicates the homogenous quality of the high-κ dielectric layer.

3.1.3 Differences between FinFETs and tri-gate transistors

Some differences between the fabrication schemes of the FinFETs and tri-gate transistors are reflected in the measurements. The undoped channel of the FinFET, compared to the boron doped channel of the tri-gate transistor, gives a smaller chance to measure a single boron atom and a minimal chance of finding a pair of atoms. Furthermore, only the substrate of the SOI wafer of the tri-gate transistors could be used as a back gate. Certain measurements presented in this thesis require the use of a back gate, making the tri-gate transistor the only choice for these measurements. Other effects in the single boron measurements, such as different tunnel couplings, heavy-light hole splittings, and spin-selective tunneling, are found to be sample specific. The number of measurements performed for this thesis are not sufficient to conclude if there is any general difference in these measurement characteristics between the FinFETs and tri-gate transistors.

3.2 Transport measurements

The primary measurement technique to identify single acceptor atoms is measuring the electronic transport through a transistor at or below liquid

helium temperature of 4.2 K. This section presents the standard transport experiments carried out for this thesis to resolve the electrical properties of single acceptors.

3.2.1 Single hole transport

In transistors with gate lengths below ∼100 nm hole transport via individual impurity atoms located in the channel can occur and can be detected at liquid helium temperatures. Because the electronic states of these atoms are located in the band gap of silicon, the transport of the first electrons or holes in the transistors can often be ascribed to transport via these impurity atoms.[27,57,59,117] This is generally followed by transport through multiple quantum dots, created either due to the roughness of the Si/SiO_2 interface,[118] or in the corners of the transistor channel between the barriers induced by the spacers.[119]

The classical effect of Coulomb repulsion results in a charging energy (E_C) needed to charge a localized site with an additional charged particle, like a hole. Charged particles that reside closer together due to a stronger confinement potential, experience a larger charging energy. The Coulomb potential of a shallow acceptor atom strongly confines a hole in all directions, leading to a large charging energy. For a boron atom, $E_C = 44$ meV in bulk silicon, and represents the difference in the binding energy of the first and second hole.[71,120] However, perturbations to the confinement potential due to for instance a nearby interface or local electric field, can strongly influence the charging energy.[57,121] In general, the total energy needed to add a hole to a localized site, the addition energy, consists of the charging energy and the level spacing between the energy level of the added hole and highest occupied energy level, Δ. However, for shallow acceptors only two holes can be bound to the atom, which will fill the same energy level with opposite spin and therefore the level spacing is not observable in a measurement of the addition energy of the atom.

The effects of the Coulomb repulsion on transport measurements are well understood.[122] Here the hole transport via an individual impurity atom in a transistor is described for the low temperature limit, $k_B T \ll E_C$, and the weak coupling regime, $h\Gamma \ll E_C, \Delta$, where the tunnel coupling to the source and drain does not exceed the relevant energy scales of the atom. This regime is the most relevant for single acceptor atoms in transistors due to their large charging energy and level spacings in the order of several tens of meVs, compared to

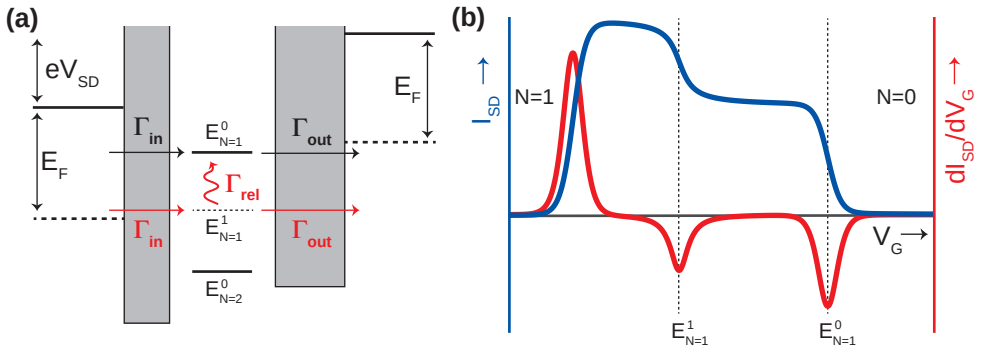

Figure 3.5: Single hole transport. **(a)** Schematic presentation of the sequential hole tunneling process via the first hole ground state $E^0_{N=1}$ (black) and excited state $E^1_{N=1}$ (red). Note that hole transport via the excited state can either follow a relaxation path to the ground state before tunneling out of the atom or tunnel directly from the excited state, depending on the ratio of the tunnel and relaxation rates. **(b)** Typical source-drain current (blue) and trans conductance dI_{SD}/dV_G (red) as a function of gate voltage, when single hole tunneling is possible through both the ground state and an excited state. In this example the ground state shows a thermal line broadening, while the excited state has a lifetime broadened line shape.

tunnel rates which are typically ranging from a few tens of MHz to a few tens of GHz for detectable atoms.[123] If the phase information of the hole is lost while traversing the transistor, because of a weak tunnel coupling compared to the phase coherence time, the hole transport can be described by a sequential hole tunneling process, as schematically shown in Fig. 3.5. This is the transport behavior observed in most of the experiments presented in this thesis.

In the case where only a single energy level of the atom contributes to the transport, i.e. when the source-drain bias voltage is smaller than the level spacing ($eV_{SD} < \Delta$), and assuming sequential tunneling, the occupation of this atomic level (P_0) is described by the following master equation:

$$dP_0/dt = \sum \Gamma_{in}\ [1 - P_0] \quad - \quad \sum \Gamma_{out}\ [P_0], \tag{3.1}$$

where the density of states is included in the tunnel-in rates (Γ_{in}) and tunnel-out rates (Γ_{out}). The filling of the source and drain reservoirs at the energy of the atomic level determine if holes can tunnel in or out of the atom. The distribution of holes in the reservoirs can be described using the Fermi-Dirac distribution:

$$f_h(E) = 1 - f_e(E) = 1 - \frac{1}{e^{(E-E_F)/k_BT} + 1}, \tag{3.2}$$

where E_F is the Fermi energy. At a low temperature, this results in a sharp transition from occupied states to unoccupied states, where an occupied hole

state is needed to tunnel in, and an unoccupied state is needed to tunnel out. Using Eq. 3.1 it can easily be observed that if the energy level is below the Fermi energy of both the source and drain, when the tunnel-in rate is zero, the energy level will be empty in the steady-state solution ($dP_0/dt = 0$). Similarly, if the energy level is above the Fermi energy of both the source and drain when the tunnel-out rate is zero, the energy level will be occupied in the steady state solution. In both situations there is no hole transport possible through the transistor, where the current is described by $\Gamma_{out}P_0$. Only when the energy of the atomic level falls between the Fermi energy of the source and drain reservoir, hole transport is possible. The difference between the Fermi levels of the source and drain is set by the source-drain bias voltage as eV_{SD}, as shown in Fig. 3.5a, called the bias window. If the atomic level is far from the Fermi energy of either lead and inside the bias window the maximum steady state current is found by solving $dP_0/dt = 0$ in Eq. 3.1:

$$I_{\max} = e\frac{\Gamma_{in}\Gamma_{out}}{\Gamma_{in} + \Gamma_{out}}. \tag{3.3}$$

Both the heavy-light hole degeneracy and the spin degeneracy are of importance for acceptor atoms, and are taken into account in the tunnel rates. Any tunnel-in rate is multiplied by the degeneracy of the energy level, to account for the possibility to tunnel to multiple quantum states, whereas any tunnel-out rate is not altered as the hole comes from a single quantum state. As a result of the degeneracy of the atom energy levels and the often observed asymmetry of tunnel barriers, different current maximum are found for the different polarities of the bias voltage. In the limit of a strong barrier asymmetry, $\Gamma_{\mathrm{source}} \ll \Gamma_{\mathrm{drain}}$ or $\Gamma_{\mathrm{source}} \gg \Gamma_{\mathrm{drain}}$, the degeneracy can be found as the ratio of $I_{\max}$ found at positive and negative bias voltages.

Furthermore, the density of states of the atomic level has an effect on the measured current. The density of states of the atomic level originates from the tunnel coupling to the source and drain, given by the time-energy uncertainty relation, resulting in a Lorentzian lineshape:

$$\mathrm{DOS}(E) = \frac{1}{2\pi}\frac{\Gamma}{(E - E_0)^2 + \Gamma^2/4}, \tag{3.4}$$

where E_0 is the energy of the atomic level. The lineshape of the steps in current and peaks in differential conductance ($\mathrm{dI/dV}_{SD}$) and trans conductance ($\mathrm{dI/dV}_G$) is given by the combination of the Fermi-Dirac distribution in the reservoirs and the Lorentzian broadening of the atomic level. In Fig. 3.5b the thermally broadened limit, $k_BT \gg h\Gamma$, is illustrated as a Fermi-Dirac

broadening of the $E^0_{N=1}$ resonance and the lifetime broadened limit, $h\Gamma \gg k_B T$, is illustrated as a Lorentzian broadening of the $E^1_{N=1}$ resonance.

When multiple energy levels of an atom lie within the bias window, additional transport paths for the hole to traverse the transistor are available. In the case of two energy levels, three first order transport processes are possible, which are illustrated in Fig. 3.5a: i) the hole tunnels in and out via the ground state of the atom, ii) the hole tunnels in and out via the excited state of the atom, and iii) the hole tunnels in via the excited state, relaxes to the ground state and tunnels out from the ground state. This can be described by the master equations for the ground state (P_0) and excited state (P_1):

$$dP_0/dt = \sum \Gamma^0_{in}\,[1 - P_0 - P_1] \;-\; \sum \Gamma^0_{out}\,[P_0] \;+\; \Gamma_{rel}\,[P_1], \tag{3.5}$$

$$dP_1/dt = \sum \Gamma^1_{in}\,[1 - P_0 - P_1] \;-\; \sum \Gamma^1_{out}\,[P_1] \;-\; \Gamma_{rel}\,[P_1]. \tag{3.6}$$

The maximum current through the transistor can again be established by finding the steady state solution to these differential equations, and is strongly dependent on whether a tunnel rate or the relaxation rate is dominant. In the limit of a fast relaxation rate ($\Gamma_{rel} \gg \Gamma$), the extra energy level merely increases the tunnel-in rate:

$$I_{\max} = e\frac{(\Gamma^0_{in} + \Gamma^1_{in})\Gamma^0_{out}}{\Gamma^0_{in} + \Gamma^1_{in} + \Gamma^0_{out}}. \tag{3.7}$$

This typically applies to the case of a large level spacing, like for the atomic orbital energy levels. In transistors with asymmetric barriers, this only leads to a significant increase in current if $\Gamma_{in} \ll \Gamma_{out}$. For this reason, in such transistors the addition of excited states in the bias window is usually only detectable in one of the transport directions.

3.2.2 Signatures of a single acceptor

The single atom in the transistor can be modelled in the simple electrostatic picture shown in Fig. 3.6a. The potential on the atom is controlled by the voltages on the top and back gate as well as the voltages on the source and drain. By changing any of these voltages, the energy levels of the atom can be moved in and out of the bias window. The ratio by which the potential on the atom changes by adjusting one of the electrodes potentials, follows from the capacitive model:

$$\Delta V_{\text{atom}} = \frac{C_i}{C_{\text{tot}}}\Delta V_i = \alpha_i \Delta V_i, \tag{3.8}$$

where i represents any of the electrodes and $C_{\text{tot}} = C_S + C_D + C_{TG} + C_{BG}$. The factor α is called the lever arm.

The signatures of an individual acceptor atom are visible in a map of the current measured between the drain and ground as a function of the voltages applied to the gate and source, as illustrated in Fig.3.6b. The charging energy, which separates the energies where the first and second hole can be bound to the acceptor, defines the Coulomb blockade regions of zero current in this transport diagram, which are called Coulomb diamonds. In each successive diamond an extra hole is trapped on the atom. The height of the first diamond indicates the source-drain voltage where the energy levels of the first and second hole are found on each side of the bias window and the current can not be blocked anymore by moving the potential of the atom. This voltage directly relates to the charging energy, which is given by:

$$E_C = \frac{e^2}{C_{\text{tot}}}. \tag{3.9}$$

The width of the diamond scales with the height of the diamond, with a proportionality of α_{TG}. A measurement of a charging energy above ∼25 meV is a strong indication of hole transport via an atom in the transistor, since quantum dots formed in the channel have typical charging energies ranging from 5 to 20 meV.

The exact shape of the diamond depends at which voltages the atomic levels enter and exit the bias window. In the capacitive model presented here the drain electrode is grounded, therefore the size of the bias window is solely dependent on V_S. The potential of the atom changes both by adjusting the top gate voltage and the source voltage, which leads to the specific slopes of the diamonds. Here the positive slope represents the tunneling from and to the source reservoir given by $C_{TG}/(C_{\text{tot}} - C_S)$. The negative slope represents the tunneling from and to the grounded drain reservoir given by C_{TG}/C_S. The measurement of the relative capacitive coupling of the atom to the different electrodes gives an idea of the location of the atom within the channel of the transistor.

The presence of excited states within the bias window results in a step in the current. The height and even the sign of this step strongly depend on the tunnel rates and relaxation rates present in the probed system. The most common signature is a positive step at either the positive or the negative V_S region, which indicates a system with asymmetric barriers and a fast relaxation time as described before. The excited state energies can be directly readout by the size of the bias window set by V_S, as shown in Fig. 3.6b. The measured

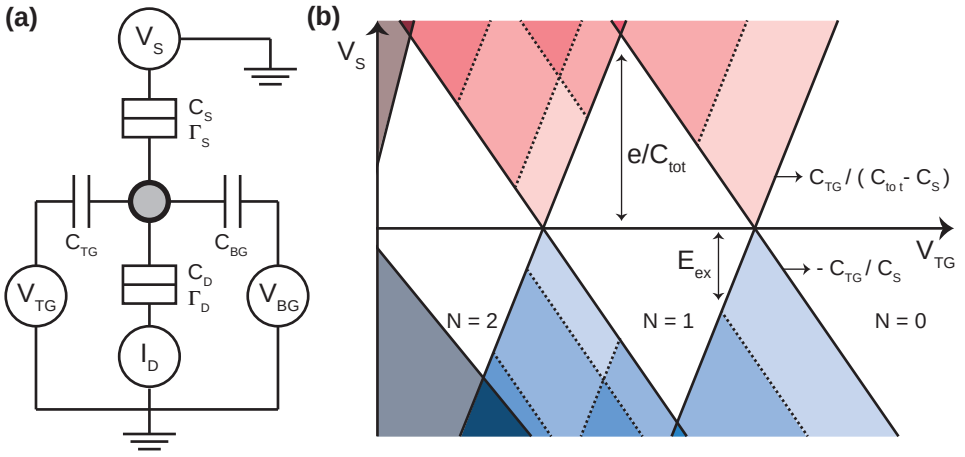

Figure 3.6: Coulomb blockade. **(a)** Electrostatic representation of an individual atom capacitively coupled to four electrodes and tunnel coupled to the source and drain. **(b)** Depiction of a stability diagram, which shows the hole transport as a function of the voltages applied to the gate and source. The effect of Coulomb blockade causes the diamond shaped regions of zero current, where in each successive diamond an extra hole is bound to the atom. The features are linked to the capacitive couplings in the system and the energy spectrum of the atom.

excited state spectrum is also a good indicator of the presence of an acceptor atom, as the excited state spectrum of an acceptor atom is irregular compared to the more evenly spaced orbital levels of a quantum dot.

3.2.3 Signatures of a double acceptor system

The measurement of hole transport by sequential tunneling in series via two atoms located in the channel of the transistor, reveals information about both atoms and their coupling. The transport through two atoms is analogous to the transport through a double quantum dot system, which has been studied extensively.[124] Essential to a double acceptor measurement is individual control over the potential on each atom. In a transistor this is usually achieved by the difference in capacitive coupling of the atoms to the different electrodes. In the example shown in Fig. 3.7 the difference in capacitive coupling to the top gate and back gate is used to achieve separate control over each atom.

Hole transport becomes possible when the required potential to add a hole to one atom is in resonance with the potential to add a hole to the other atom, and they both are within the bias window, as schematically shown in Fig. 3.7a. In this case the depicted transport process shows the addition of the first hole to the left atom and the second hole to the right atom, when the bias voltage

condition is such that the transport direction is from the left atom to the right atom. In the case of sequential hole transport, this process consists of three individual tunneling processes: i) a hole tunnels from the source to the left atom (Γ_{in}), ii) a hole tunnels between the two atoms (Γ_{int}), and iii) a hole tunnels from the right atom to the drain (Γ_{out}). The tunnel rate between the acceptor atoms does not only depend on the tunnel barrier between the atoms, but also on the availability of a quantum state in the other atom for the particular spin state of the hole. For an even number of holes this can lead to the Pauli spin blockade effect, where two holes can form a triplet state when located on different atoms, which is not available for both holes on the same atom. Depending on the tunnel rates in the system and the spin-flip rate, this effect can strongly reduce the current in the positive bias direction compared to the negative bias direction.

As the potential on each atom is dependent on the charge on the other atom through a mutual capacitive coupling, two transport paths are created. In one of the transport paths the processes i) and iii) occur with one hole less on the other atom as compared to the other transport path. For the scenario in Fig. 3.7a this can be described by denoting the charge occupation of both atoms as (N_L, N_R) during the transport as $(0,1) \rightarrow (1,1) \rightarrow (0,2) \rightarrow (0,1)$ for the first path and $(1,2) \rightarrow (1,1) \rightarrow (0,2) \rightarrow (1,2)$ for the second path. In both transport paths the hole tunneling between the two atoms changes the charge

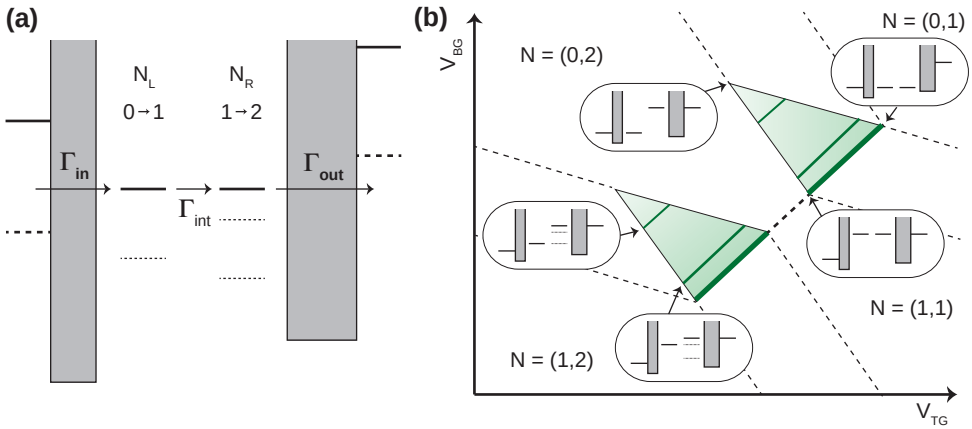

Figure 3.7: Double acceptor transport. **(a)** Schematic presentation of the sequential hole tunneling process via two atoms in the bias window of the transistor.**(b)** Series transport through two atoms in a transistor results in bias triangles in the top gate - back gate map. The alignment of the energy levels at the corners of a triangle and the resonances with excited states are schematically represented.

occupation by (1,1) → (0,2), while a reversed source-drain bias voltage would reverse this transition to the (0,2) → (1,1) transition. The potential at which this transition is resonant forms a line in a map of two of the applied voltages, like the top gate - back gate map shown in Fig. 3.7b. At a small applied bias voltage, the signals from both resonant transport paths form the two dark green lines in this map where hole transport is possible. When off-resonant tunneling between the atoms occurs, and both relevant energy levels are in the bias window, hole transport appears when no extra energy gain is needed to tunnel between the atoms. In this scenario, the tunneling to the left atom should occur at a lower potential than the tunneling to the right atom. This results in a typical triangular shape of the off-resonant current, as can be seen in Fig. 3.7b. Within these so-called bias triangles, other resonances might occur when excited states of one of the atoms are aligned with either the ground state or an excited state of the other atom. In Fig. 3.7b two resonances are shown as thin dark green lines corresponding to the ground state of the left atom aligning with the excited states of the right atom.

3.3 RF reflectometry measurements

An rf-gate reflectometry measurement technique was used to reveal charging events that can not be measured in transport experiments, thereby probing more of the atoms residing in the transistor channel. This technique relies on a resonator, consisting of an inductor and capacitor, which is attached to one of the gates, and has been demonstrated for several semiconductor systems.[125–129] Charging events in the transistor which slightly change the resonant conditions of this resonator can be sensed in the reflected signal. This section explains the working principles of the rf-gate reflectometry technique.

3.3.1 Charge transition sensing

A resonant circuit is created by attaching a surface-mount inductor, with an inductance L, to one of the electrodes, and the parasitic capacitance of this electrode, C_p, creates a tank circuit with a resonant frequency f_0 given by:

$$f_0 = \frac{1}{2\pi\sqrt{LC_p}}. \tag{3.10}$$

To operate as a charge transition sensor, the circuit is driven at a frequency f_{dr}, close to the resonance frequency f_0, and the reflection of this circuit, Γ_{LC},

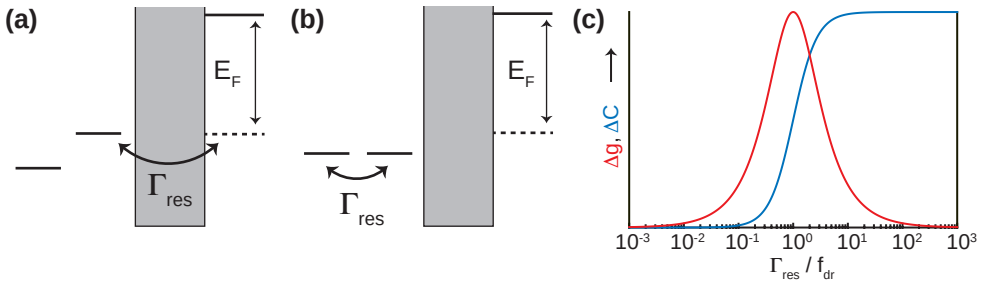

Figure 3.8: RF reflectometry. **(a)** Resonant tunneling between an atom and one lead causes a change in the reflection of the resonant circuit dependent on the tunnel coupling Γ_{res}. **(b)** The same holds for resonant tunneling between two atoms. **(c)** Maximum change in conductance and capacitance of the circuit as a function of the ratio between the tunnel coupling and the driving frequency.

is measured using a homodyne detection scheme. The reflection is given by:

$$\Gamma_{LC} = \frac{Z - Z_0}{Z + Z_0}, \tag{3.11}$$

where Z_0 is the impedance of the transmission line, which is 50 Ω in the experiments presented in this thesis, and Z is the complex impedance of the resonant circuit. This frequency dependent impedance is minimized at the resonance frequency, and can be expressed as the impedance coming from the inductance, capacitance, and any parasitic resistance of the circuit, like the resistance of the coils of the inductor. The resistance in the circuit causes damping of the resonator, and a change of this resistance can be measured as a change of the quality factor (Q-factor) of the resonance.

The resonant tunneling of holes in the channel of the transistor can be driven by the ac voltage of the resonator, which changes the capacitance and the resistance of the electronic circuit, depending on the tunnel rate of the holes. The resonant tunneling can occur between an atom and one of the reservoirs, as shown in Fig. 3.8a, or between two atoms, as shown in Fig. 3.8b. The effect of hole tunneling is discussed in three different scenarios: $f_{dr} \gg \Gamma_{res}$, $f_{dr} \sim \Gamma_{res}$, and $f_{dr} \ll \Gamma_{res}$. In the case of $f_{dr} \gg \Gamma_{res}$, i.e. the driving frequency of the resonator is much faster than the tunnel rate of the holes, on average no charge is transferred during a period of the resonator and the resonance is unaffected by the hole tunneling. In the case of $f_{dr} \sim \Gamma_{res}$, one charge transfer occurs on average every period of the resonator, however off-resonant tunneling has a substantial contribution, leading to dissipation in the circuit. In the case of $f_{dr} \ll \Gamma_{res}$, the resonant hole tunneling is dominant, and the charge transferred in the transistor induces a change in capacitance due to the

dipole coupling to the resonator. The maximum change in conductance and capacitance, found when two levels are in resonance, are given by:

$$\Delta g = \frac{\alpha^2 e^2}{4k_B T} \frac{\Gamma_{res}}{1 + \Gamma_{res}^2 / f_{dr}^2}, \tag{3.12}$$

$$\Delta C = \frac{\alpha_\Delta^2 e^2}{4k_B T} \frac{1}{1 + f_{dr}^2 / \Gamma_{res}^2}, \tag{3.13}$$

where α_Δ refers here to the difference in relative capacitive coupling of the hole in the two charge configurations involved in the resonant tunneling process. The Δg and ΔC are shown as a function of the ratio between the tunnel rate and driving frequency in Fig. 3.8c.

A change in capacitance primarily results in a shift in the resonant frequency, whereas a change in conductance primarily produces a change in quality factor. Depending on the chosen driving frequency f_{dr}, these effects are measured as either a change in the amplitude or phase of the reflected signal, which are defined in terms of the in-phase (I) and quadrature (Q) detected signals:

$$Ae^{i\phi} = I + iQ. \tag{3.14}$$

As the amplitude and the phase change drastically around the resonant frequency, the highest sensitivity to charge tunneling can be achieved by driving the system close to the resonant frequency. Furthermore, the sensitivity increases if the parasitic capacitance of the circuit is kept to a minimum, leading to a larger relative change in capacitance by the addition of a quantum capacitance.

3.3.2 Comparison transport and reflectometry measurements

The two measurement techniques presented in this section and used in the experiments in this thesis have different boundary conditions and therefore reveal complementary information about the atoms located in the transistor. Transport measurements require the total tunnel rate ($\Gamma_{in}\Gamma_{out}/(\Gamma_{in} + \Gamma_{out})$ to

Table 3.1: Comparison of the bandwidth and sensitivity of three rf reflectometry detection techniques reported in literature.[128,130–134]

Detection technique	bandwidth [MHz]	sensitivity $[e\sqrt{Hz}]$
rf-gate	20 [130]	4×10^{-5} [128]
rf-SET	1 [131]	1×10^{-6} [132]
rf-QPC	20 [133]	$5 \times 10^{-6}\ e/h$ [134]

be large enough to give a detectable current. Typical transport measurements are performed using a 10 Hz bandwidth, where a noise floor of $\sim$ 100 fA is reached. This gives a lower bound for the total tunnel rate of $\sim$ 500 kHz. In contrast, the rf reflectometry measurements start to become sensitive when the tunnel coupling approaches the resonant frequency of the LC-circuit, which is typically chosen to be between 100 MHz and 1 GHz. Although this regime is about 3 orders of magnitude higher than in transport measurements, there is no requirement for the hole to traverse the transistor in reflectometry measurements. This allows for the identification of atoms which are not detected by transport experiments.[127] In general, transport measurements probe atoms located in the centre of the transistor, where both the tunnel-in and tunnel-out rate are sufficient for the detection of a current. Reflectometry measurements typically probe atoms located near one of the reservoirs, or near another atom, to ensure a sufficient resonant tunnel rate to be detected in the reflection of the LC-circuit. The sensitivity and bandwidth of the rf-gate reflectometry technique reported in the literature is compared to the state-of-the-art charge detection techniques of the rf-QPC and rf-SET in table 3.1.

3.4 Conclusion

The tri-gate transistors used in the experiments in this thesis were characterized at room temperature, and showed the typical behavior of state-of-the-art nano-scale transistors, including short channel effects and a minimum sub-threshold slope around 60 mV/dec. This demonstrates the ideal thermionic transport, confirming the high device quality as expected from the industrial fabrication process. The experiments presented in this thesis are performed using both dc transport and rf gate reflectometry measurement techniques, which provide complementary information about the charge and spin degrees of freedom of acceptor atoms in silicon transistors. The transport measurements reveal the energy spectrum and the charging energies of individual acceptor atoms located near the centre of a transistor. In addition, the rf gate reflectometry technique allows to probe charge transitions which do not add to the current flow through the transistors, such as transitions occurring on only one side of the transistor or between two localized states inside the channel.

chapter 4

Single acceptor atom

This chapter presents the study of the electric and magnetic properties of the quantum states of a single hole bound to a single acceptor atom in silicon. Single-hole transport reveals the signatures of an individual boron atom, which is embedded in the channel of a CMOS transistor. The measured charging energy and excited state spectrum of this atom are comparable to the known values for boron in bulk silicon. Furthermore, the Zeeman effect on the acceptor ground state, studied using magneto-transport spectroscopy, shows a splitting in four states, which is unique for a single hole bound to an acceptor in a bulk semiconductor. The two lowest spin states are heavy ($|m_j|$=3/2) and light ($|m_j|$=1/2) hole-like. The identification of a bulk-like energy spectrum and magnetic field dependence of a boron atom in a nano-transistor is remarkable and demonstrates that it is possible to access both heavy and light holes states in nano-structures. The measured Landé g-factors, $|g_{hh}| = 0.81 \pm 0.06$ and $|g_{lh}| = 0.85 \pm 0.21$ for heavy and light holes respectively, are lower than the bulk value, which shows the influence of the local environment on the confinement potential. The Zeeman effect is further investigated by measuring the dependence of the Landé g-factor on the direction of the magnetic field and on the strength of an applied electric field.

Part of this chapter is published as:

- J. van der Heijden, J. Salfi, J.A. Mol, J. Verduijn, G.C. Tettamanzi, A.R. Hamilton, N. Collaert and S. Rogge, *Probing the spin states of a single acceptor atom*, Nano Letters **14**, 1492-1496 (2014).

4.1 Introduction

The promise of single atoms in semiconductors for quantum technologies is driven by their well-defined confinement potential. Most properties of dopant atoms in semiconductors have been studied in ensemble measurements in the bulk regime. However, single atoms in nano-structures are needed for the possible applications, such as quantum information processing or quantum sensing. Therefore the investigation of the influence of a nano-device on a single atom, like nearby interfaces, local strain, strong electric fields, and the proximity of defects, is essential.

For single boron atoms in silicon nano-structures the perturbation of the confinement potential by the environment can have a beneficial effect on the properties vital for quantum applications, such as the dipole coupling strength and coherence time.[93,109] The spin states of confined holes in nanostructures are predominantly built up from heavy and light holes, in a way which is strongly dependent on the symmetry of the confinement potential. The Coulomb potential of an acceptor atom does not break the cubic symmetry of the silicon lattice and therefore preserves the degeneracy of heavy and light holes.[73,87] In contrast, in a two-dimensional hole gas, the heavy holes form the lowest energy states,[135,136] while in an ideal one-dimensional structure with cylindrical confinement these consist of light holes.[137] Furthermore, the confinement of self-assembled or gate-confined quantum dots also leads to a considerable splitting between the heavy and light holes, making the heavy holes the lower lying states.[138,139]

In a similar way, the bulk fourfold degenerate acceptor ground state can be split in two Kramers doublets by an electric field, strain or a nearby interface.[73,87] These split Kramers doublets have been observed in ensembles of boron dopants in intentionally strained silicon,[76] for single acceptors in silicon Schottky barriers subject to random strains and electric fields[88] and for acceptor atoms nearby a vacuum interface.[89] A large energy splitting between the heavy and light hole states makes them unsuitable to drive electrically, because of a large Larmor frequency and a short relaxation time.

As an alternative to gate-defined quantum dots in both III-V[106,139–142] and group IV[143–149] material systems, the spin states of acceptors also couple to oscillating electric fields, forming favourable two-level systems for electrically controllable qubits.[107,150] Ensemble acceptor measurements have demonstrated that a large (∼0.3 Debye) dipole coupling exists between the states of heavy (m_j=±3/2) and light (m_j=±1/2) holes bound to acceptor atoms,[75] which

is predicted to increase under the right local conditions for the acceptor.[93] Moreover, due to the symmetric confinement of a hole by the Coulomb potential of an acceptor in an unstrained crystal, the light hole and heavy hole manifolds are degenerate.[73,87] A finite magnetic field lifts this degeneracy, such that a heavy and light hole state form the lowest-energy spin states of the acceptor. A qubit composed of these two levels is characterized by a magnetic field dependent Larmor frequency and relaxation rate, which have suitable values for qubit operations (e.g. a Larmor frequency of 4 GHz with a relaxation rate of 6 μs at $\sim$0.3 T).[107]

In this chapter a single atom transistor is probed where single hole tunneling through an acceptor dopant is controlled by a gate electrode. Magneto-transport spectroscopy was used to study the spin properties of the single hole bound to the acceptor atom. The results are analysed in terms of the lowest order Zeeman effect:

$$E_Z = g_1' \, m_j \, \mu_B \, B, \tag{4.1}$$

where E_Z is the Zeeman energy, g_1' the linear part of the Landé g-factor, m_j the total angular momentum, μ_B the Bohr magneton and B the magnetic field. Higher order corrections, including a m_j^3 term and a dependence on the direction of the magnetic field compared to the crystallographic directions, as described in chapter 2, are found to be negligible.[75] In this experiment the magnetic field dependent hole transport spectroscopy shows that the ground state splits into four well defined spin states. Previously only observed in ensemble measurements on acceptors in unstrained silicon,[75,78,81,151] the availability of this fourfold degenerate ground state for a single acceptor in a nano-transistor, is promising to form a single qubit that can be electrically manipulated with local gates. The observation of this fourfold degeneracy in a single-hole transistor is nontrivial, as previous measurements have shown a splitting between the heavy and light hole Kramers doublets due to local strain, electric fields and a nearby interface.[28,88,89] Finally, the influence of the magnetic field rotation and applied electric field were studied to demonstrate the possible control over the acceptor states.

4.2 Experimental setup

In this chapter measurements on two different transistors are reported. The main part of the chapter discusses electrical transport measurements on a FinFET, as described in chapter 3 and of which a detailed description is given

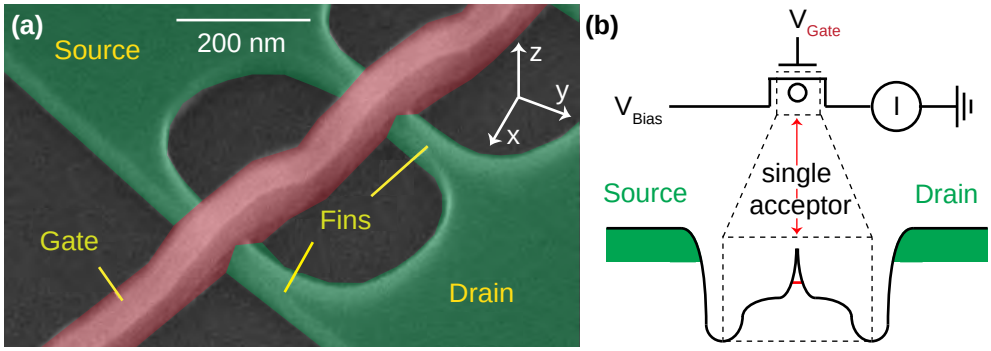

Figure 4.1: Experimental setup. **(a)** Scanning electron microscope image of a multi-channel p-type fin field effect transistor (FinFET), similar to the one used to detect a single boron atom. Fabrication details can be found in the text and elsewhere.[116] This SEM image has been provided by IMEC. **(b)** Schematic view of the direct current measurement setup (top) and the potential profile through the channel of the transistor (bottom), where a single acceptor is located in the middle of the channel. Voltages are applied to the source (V_{Bias}) and gate (V_{Gate}) electrodes and the current is measured between the drain and the ground.

in the next paragraph. The experiments discussed in the last section, section 4.6, make use of a tri-gate transistor and the rf reflectometry measurement technique.

As illustrated in Fig. 4.1a, the silicon FinFET used in the main part of this chapter has two undoped fins connecting p-type (boron doped) source and drain regions. The two fins are positioned 200 nm apart from each other and have a fin height of 40 nm and a width of 25 nm. A gate nanowire is wrapped around each channel, covering them on three sides. The width of this gate nanowire is 40 nm and defines the channel length. An oxide layer consisting of 1 nm SiO_2 and 2.3 nm of HfSiO separates the channels from a gate stack of 5 nm TiN and 100 nm poly-silicon, which is enclosed by 35 nm wide nitride spacers. These spacers create potential barriers, allowing single hole transport through quantum dots, which are formed under the gate in the corners of the channel,[27,57] as shown in Fig. 4.2a. In one of the channels a boron atom is present, as schematically shown in Fig. 4.1b, which is assumed to be diffused from either the source or drain electrode. Experimental indications of dopant diffusion from the leads into the channel, have been observed in similar devices with n-type leads.[27,57,152,153] This mechanism has recently been confirmed by atom probe tomography.[115]

The electrical transport measurements were performed in a dilution refrigerator at a base temperature of 10 mK. The current was measured between

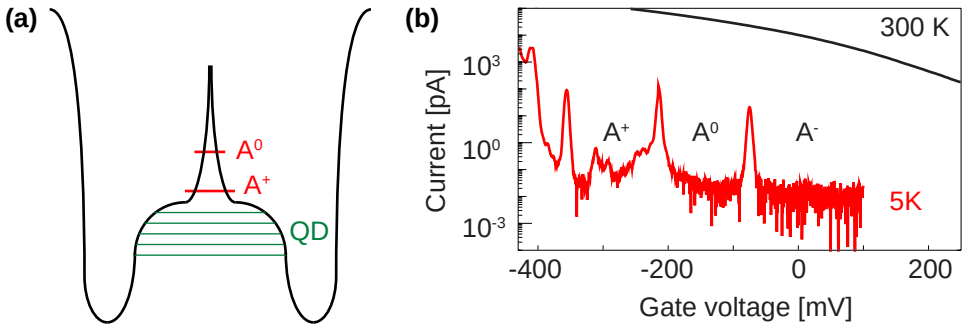

Figure 4.2: Single hole transport. **(a)** Energy states in the channel of the FinFET. In red the states of the boron atom, where the ground state of the neutral atom A^0 has a binding energy E_b of 46 meV,[71] while the ground state of the positively charged atom A^+ has a binding energy of 2 meV.[120] Between the two potential barriers created by the spacers, gate-defined quantum dots are formed in each top-corner of the transistor channel. The evenly spaced quantum dot energy states have a smaller charging energy and are shown in green. **(b)** IV traces of the single boron device at room temperature (black) and 5 Kelvin (red) at 5 and 1 mV bias voltage respectively. Two isolated current resonance peaks are the signatures of the transitions from the negatively charged acceptor (A^-) to the neutral acceptor (A^0) and from the neutral acceptor to the positively charged acceptor (A^+) by binding one and two holes to the boron atom respectively.

the drain and the ground using a low-noise current amplifier as a function of the voltage applied to the source (V_{bias}) and the gate (V_{gate}) electrodes, as shown in Fig. 4.1b. Furthermore, a vector magnet was used to supply the magnetic field. The nano-transistor used in this work provides the necessary tunnel coupling between the dopant and the leads to identify a single atom using direct current measurements.[27,59,88,154,155]

4.3 Single hole transport

With a boron atom present in the channel, two distinctive and well separated current peaks were measured (see Fig. 4.2b) as a result of single hole tunneling through the neutral (A^0) and positively charged (A^+) acceptor states. To detect the acceptor atom, a small voltage was applied to the source terminal, while the current is measured between the drain terminal and the ground as a function of the applied gate voltage. In all measured FinFETs several current peaks were detected at low temperature, and related to sequential hole tunneling through the gate induced quantum dots, before a conductive channel opens. The current peaks of the acceptor states appear before these quantum dot peaks. By using multi-channel devices the chance of finding a

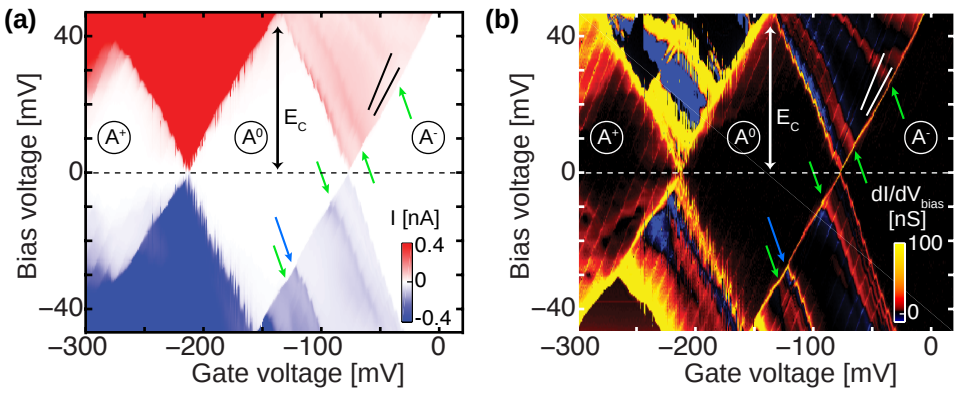

Figure 4.3: Coulomb blockade. **(a)** Measurement of the current as a function of the applied bias and gate voltages. A charging energy of 47 ± 1 meV is measured between the one and two hole states of the boron atom. The Coulomb diamonds are distorted by charging events of a nearby island, which is capacitively coupled to the boron atom. Black lines indicate the different slopes caused by the difference in capacitive couplings to the drain terminal between the atom and the nearby island. **(b)** Measurement of the differential conductance (dI/dV_{bias}) as a function of the applied bias and gate voltages. Colored arrows indicate lines of positive differential conductance in the first hole transport region, also shown in **(a)**. Green arrows indicate a change in the density of states of the drain reservoir. The blue arrow indicates where an excited state enters the bias window.

single acceptor is increased.

4.3.1 Charging energy

To investigate the electronic properties of the boron atom, a stability diagram was recorded by measuring the current as a function of the source-drain bias and gate voltage. Both the time-averaged current and the numerical differential conductance dI/dV_{bias} are shown in Fig. 4.3. The highest zero-bias resonance at $\sim$ -76 mV gate voltage was identified as the charging of the boron atom with the first hole to the A^0 state. The resonance at $\sim$ -210 mV gate voltage is identified as the transition to the A^+ state. Between these resonances the current is Coulomb blocked up to an observed charging energy of 47 ± 1 meV, which is in good agreement with the bulk charging energy of a boron acceptor (44 meV).[71,120]

Signatures of additional charging events, often observed in this batch of FinFETs, periodically disturb the shape of the Coulomb diamonds. This has been observed in similar devices and interpreted as the charging of an island, close to one of the leads.[156] In this measurement the island is located near the source electrode and the charging events occur every $\sim$10 mV in gate voltage.

The difference in coupling to the different terminals between the island and the acceptor is reflected in the slope of the conductance lines in the stability diagram. This slope is given by $C_g/(C_d + C_g)$ with C_d and C_g the capacitive coupling to the drain and gate leads respectively, as marked by black lines in Fig. 4.3a and by white lines in Fig. 4.3b. The slope of the lines created by the island is 1, which indicates the lack of capacitive coupling to the drain region, while the conductance lines of the boron atom have a smaller slope as it is capacitively coupled to the source, drain and gate leads. The conventional measurement of the charging energy, which is directly related to the bias voltage at the top of the Coulomb diamond (see Fig. 4.3), is not disturbed by these additional charging events. At this intersection, where both the A^0 and A^+ states are in the bias window, both states are affected in the same way by the charge state of the island. The observation of the same disturbances in the finite current regions of both the first and the second resonance, confirms that both resonances originate from the same object and thereby validates the measurement of the charging energy of the acceptor.

4.3.2 Excited state spectrum

In addition to the charging energy, the distinct excited state spectrum of a boron atom was observed. The presence of an excited state results in a step in current and a sharp positive differential conductance line at the negative bias voltage side, intersecting with the Coulomb diamond at -27 ± 1 mV bias voltage (see the blue arrows in Figs. 4.3a and b). At this intersection the ground and excited state are perfectly aligned with the source and drain reservoir energies respectively. For the same reason as for the charging energy, this bias voltage can be directly translated to an energy splitting of 27 ± 1 meV, which is close to the bulk value for the first excited state (23 meV) of a boron acceptor.[64] In contrast, broader differential conductance lines are found on both the positive and negative bias side parallel to the same edge of the Coulomb diamond, but without significant change in the current. These are likely a result of an energy-dependent density of states (DOS) in one of the leads,[157] here the drain reservoir, indicated with green arrows in Fig. 4.3. The observation of similar DOS signatures in the finite current region of the second resonance, confirms that this resonance is due to tunneling through the same object as the first resonance.

To understand why the positive differential conductance line, reflecting the presence of an excited state, was only observed in the negative bias

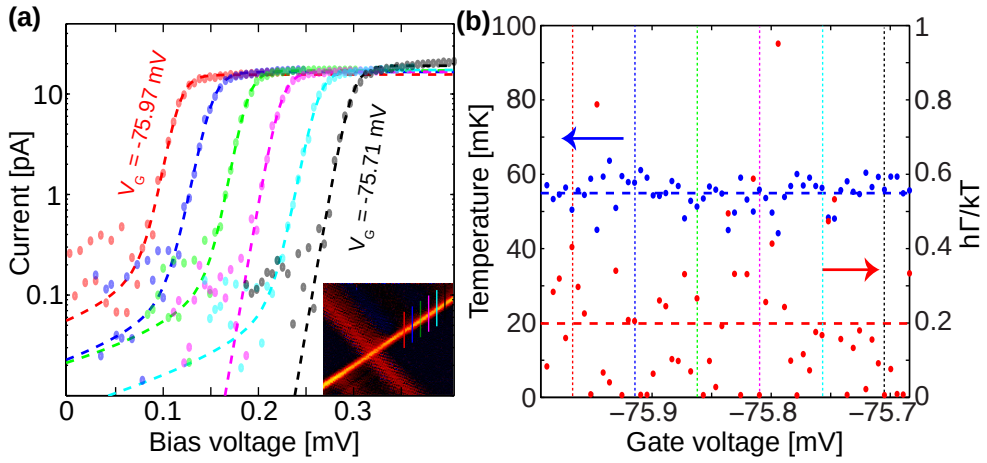

Figure 4.4: Hole temperature. **(a)** Six bias traces fitted to a temperature broadened Lorentzian peak. Inset: A close up of the zero bias crossing of the A^- to A^0 transition in Fig. 4.3b, which is not disturbed by the nearby defect and is used to determine the relative capacitive couplings to the three terminals. The positions of the six bias traces are shown in this stability diagram. **(b)** The extracted temperature (blue) and the relative lifetime broadening to this temperature (red) are shown for all traces used to establish the hole temperature. With colored dotted lines the positions of the traces in **(a)** are shown.

voltage region of the stability diagram, two possible scenarios are discussed: single hole tunneling with (i) asymmetric tunnel barriers and (ii) symmetric tunnel barriers. At the bias voltage where an excited state becomes available, the tunnel rate into the boron atom increases. Consequently, the positive differential conductance lines will always run parallel to the tunnel-in edge of the Coulomb diamond. In case (i) the excited state only leads to a step in the current, and therefore a sharp positive differential conductance line, when it increases the slow tunnel rate, which is the current defining rate. In case (ii) the current is set by a combination of both tunnel rates and this would result in positive differential conductance lines when the hole tunnels both from the source and the drain.[57] The observation of only one excited state line at the negative bias side, without a counterpart at the positive bias side, is in agreement with the case (i) of asymmetric tunnel barriers.

4.3.3 Hole temperature

The exact temperature of the holes in the experiment depends, not only on the temperature reached in the dilution refrigerator, but also on the thermalization of every connection to the transistor. To extract the hole temperature,

the Fermi-Dirac distribution of the holes in the leads of the transistor was obtained from the experiments. Sixty bias traces were fit to a thermally broadened Lorentzian line shape by taking the convolution of the Fermi-Dirac and Lorentzian line shape as reported by Foxman et al.:[158]

$$I = A \int \frac{1}{e^{(\alpha V_g - E_{\mathrm{res}} - E)/kT} + 1} \; \frac{h\Gamma/2\pi}{(h\Gamma/2)^2 + E^2} \; dE \tag{4.2}$$

Here A is an arbitrary amplitude, V_g is the gate voltage, α is a conversion factor (in this case α =1-α_s = 0.63 meV/mV), E_{res} is the resonance energy, Γ is the full-width half-maximum of the Lorentzian line shape and E is the hole energy over which the integral is taken. To get the conversion factor from the voltage to energy scale, the capacitive coupling of the boron acceptor to the three terminals was determined. By using an undisturbed section of the stability diagram (see the inset of Fig. 4.4a) the conversion factors for the gate and source voltage are determined as $\alpha_g = e\ C_g/C_t = 0.42 \pm 0.02$ meV/mV and $\alpha_s = e\ C_s/C_t = 0.37 \pm 0.01$ meV/mV respectively, where $C_t = C_g + C_s + C_d$.

Six of those fits are shown in Fig. 4.4a. The temperature and the ratio of the lifetime broadening to the thermal broadening, extracted from each of these fits, are shown in Fig. 4.4b. By fitting the data over this range of gate voltages to the thermally broadened Lorentzian, a hole temperature of 55 ± 8 mK and a small lifetime broadening of $h\Gamma/kT \sim 0.2$ were found. From Fig. 4.4a it is apparent that the fit of the lifetime broadening is mainly set by the noise floor of the measurement. Therefore this value of the lifetime broadening should be regarded as an upper bound. The hole temperature determines the differential conduction peak shape and is later used in the analysis of the Landé g-factors.

4.4 Zeeman effect of the boron ground state

To study the degeneracy of the ground state manifold of the acceptor, the splitting of the A^- to A^0 transition was measured in a magnetic field. A bias trace at -75 mV gate voltage was measured as a function of magnetic field. The magnetic field was applied parallel to the top plane of the silicon chip and with a $19 \pm 5^\circ$ angle to the axis perpendicular to the [110] direction of the current flow, defined as the x-axis in Fig. 4.1a. As the ground state is expected to shift towards a higher gate voltage when a magnetic field is applied, traces were taken at a gate voltage higher than the zero-field zero-bias crossing.

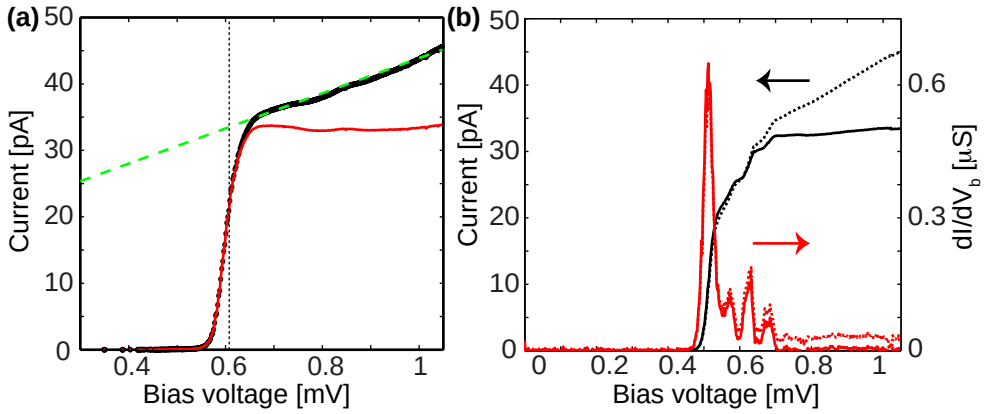

Figure 4.5: Effect of density of states in the lead electrodes. **(a)** The change of density of states in the leads determines the change in current when the energy states of the acceptor are not entering nor leaving the bias window. This dependence on density of states was extracted from the measured current (black) of a bias trace at zero magnetic field and a gate voltage of -75 mV. A linear approximation was used to fit the density of states behavior (green) and the measured current is divided by this linear function (red), which was normalized at the position of the current step. **(b)** For a bias trace at 0.7 Tesla, both the current (black) and the differential conductance (red) before (dotted lines) and after (solid lines) correcting for the density of states are shown.

4.4.1 Influence of density of states

The current steps originating from spin-excited states and a positive differential conductance induced by the changing density of states of the leads are superimposed. This DOS effect was subtracted from the raw data before fitting the magnetic field dependence to a linear Zeeman effect. The bias trace at zero magnetic field is shown in black in Fig. 4.5a. Because of the visibly positive linear slope of this trace after the current step, the density of states was approximated by a linear function, which was normalized at the position of the conductance peak (green). For the fit of the magnetic field dependence, all bias traces were divided by this linear approximation of the density of states, as shown in Fig. 4.5a for the trace at zero magnetic field (red) and in Fig. 4.5b for the trace at 0.7 T (black). In Fig. 4.5b the shift of the differential conduction is also visible. The original data is shown as dotted lines and the density of states corrected data as solid lines.

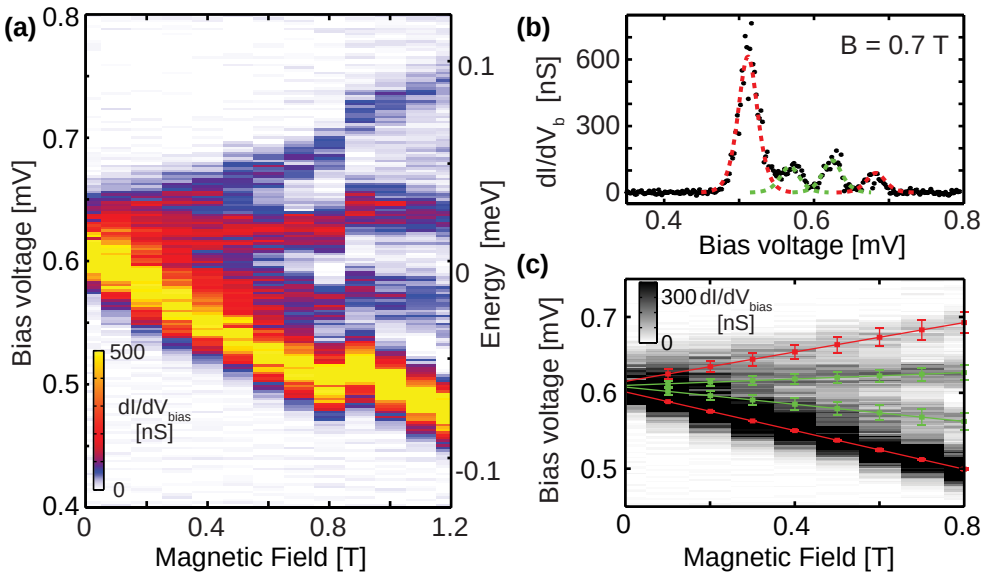

Figure 4.6: Zeeman splitting of the A^0 ground state. **(a)** Magnetic field dependence of the A^0 state at a gate voltage of -75 mV. The numerical differential conductance shown here is calculated after correcting the data for the DOS background. Between the 0.8 and 0.9 T a clear shift is observed, which is caused by a change of the charge state of a nearby defect. **(b)** The conduction peaks between 0 and 0.8 T are fit to four thermally broadened peaks, with a linear dependence on the magnetic field and constant peak heights. The trace at 0.7 T is compared to this fit. **(c)** The fit results with 95% intervals displayed on top of the differential conductance data. The splitting between the heavy (red) and light (green) hole-like doublets are used to calculate the g-factors.

4.4.2 Zeeman splitting of the A^0 ground state

The A^0 ground state splits into four spin states under the applied magnetic field, as shown in Fig. 4.6a. This confirms that the symmetry expected for an acceptor in bulk silicon is preserved for the single boron atom in this nano-transistor. Between 0.8 and 0.9 T, a change in the charge occupation of a nearby defect causes a small shift in the data shown in Fig. 4.6a. At higher magnetic fields, the current steps of the excited states decrease in amplitude, because of the increasing relaxation rates.

The Zeeman-type interaction is approximated as a linear function $E_Z = g m_j \mu_B B$ for each of the four states, where μ_B is the Bohr magneton, B the magnetic field and m_j the projection of the total angular momentum in the direction of the magnetic field. The effects of electric field and strain are not taken into account as they are, although not precisely known, small compared to the Zeeman interaction as evidenced by the fourfold degenerate

acceptor ground state. Thermally broadened peaks are used to approximate the conductance peaks, using the earlier determined hole temperature, as shown in the trace at 0.7 T in Fig. 4.6b. As the tails of the conductance peaks overlap, it can not be excluded that some of these peaks have extra broadening due to a finite lifetime of the states. However to find the relative positions of the peaks the thermal fit is sufficient. A fit to the linear Zeeman model for the data up to 0.8 T is shown in Fig. 4.6c with 95% confidence intervals. A ΔE_Z of 0.141 ± 0.010 meV/T was found between the ground state and third excited state (red fits in Figs. 4.6b and 4.6c) and a ΔE_Z of 0.049 ± 0.012 meV/T was found between the first and second excited states (green fits in Figs. 4.6b and 4.6c), using the $1 - \alpha_s$ factor to convert the voltage scale to energy. To calculate the g-factors and compare them to the values found in electron paramagnetic resonance measurements,[75] the assumption made by Köpf and Lassmann[75] that the four boron states are constructed from only light or heavy holes, with m_j= +3/2, +1/2, -1/2 and -3/2 respectively, was followed. The g-factors for the $\Delta m_j = 3$ (red) and $\Delta m_j = 1$ (green) cases are $|g_{\Delta m_j=3}| = 0.81 \pm 0.06$ and $|g_{\Delta m_j=1}| = 0.85 \pm 0.21$ respectively.

The g-factors found in this nano-structure are significantly smaller than the g-factors found for boron in bulk silicon, whose absolute value ranges from 1.08 to 1.18 depending on the direction of the magnetic field with respect to the crystal axes.[75] The lower g-factor can be associated with a change in the shape of the orbital, which influences the Zeeman splitting due to the presence of spin-orbit coupling. This change in g-factor is remarkable, since the heavy and light hole doublets are not split within the accuracy of the experiment, meaning that the distortion does not significantly break the cubic symmetry of the crystal. In this nano-scale transistor, with a channel of 25 by 40 by 40 nm, it is believed that the dominant contribution to the observed reduction of the g-factors is the effect of the nearby Si/SiO_2 interfaces (at most ∼12.5 nm away).

In the same batch of devices, acceptors with a twofold degenerate ground state, a nearby first excited state, and a second excited state with a lower energy splitting than the bulk value of 23 meV, were measured, which correspond to acceptor atoms positioned very close to the interface.[89,159] By comparing these measurements to observations of single donor atoms in similar devices,[57,119] which generally show that the atomic charging energies and level spacings are affected by a nearby interface, the measurement of the fourfold degenerate ground state is regarded as an uncommon case.

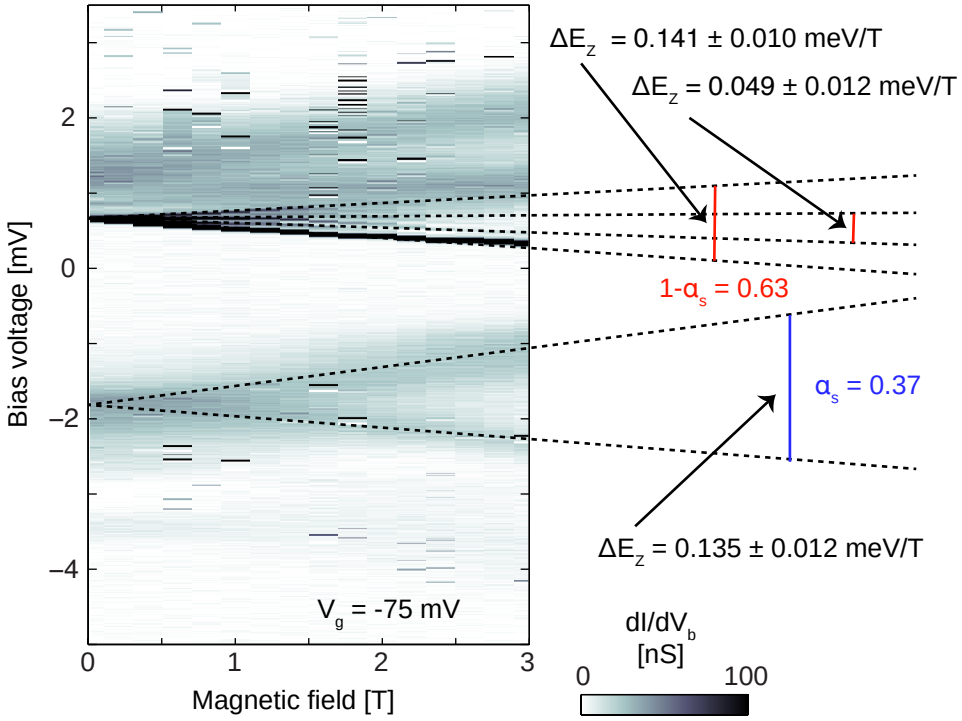

Figure 4.7: Zeeman splitting in reversed bias regime. On the left side the differential conductance is shown as a function of bias voltage and magnetic field at a gate voltage of -75 mV. On the right side the lines following the visible positive differential conduction lines are extended for both the positive and negative bias voltage sides. The energy splitting per Tesla is shown for these lines, making use of the correct conversion factors α_s and 1-α_s.

4.4.3 Negative bias direction

To support the measurement of the Zeeman splitting, the magnetic field dependence for the reversed polarity of the bias voltage (holes tunneling from the drain instead of the source to the atom) was also investigated. The splitting of the A^0 state into four states is visible on the positive bias voltage side in Fig. 4.7. At the negative bias voltage a splitting in two lines is visible. All the energy splittings between the excited state lines, extracted using the appropriate conversion factors (1-α_s for positive bias and α_s for negative bias), are presented in the right side of Fig. 4.7. As mentioned before, at the positive bias side the splitting between the ground and third excited state is 0.141 ± 0.010 meV/T and the splitting between the first and second excited state is 0.049 ± 0.012 meV/T. At the negative bias voltage side an energy splitting of 0.135 ± 0.012 meV/T is measured. This splitting is in good agreement with the splitting found between the heavy hole states at the positive bias

voltage. This indicates that in the negative bias direction only the heavy hole excited states are observed, while the light hole states are not. This could be caused by the large broadening of the positive differential conductance lines, which make the signatures of light hole states difficult to distinguish. Another possible explanation is the presence of a heavy-light hole splitting at the end of the drain lead, due to some additional confinement. A confinement potential can act as a spin-filter such that only heavy holes can tunnel to the acceptor from the drain. In this scenario, the magnetic field dependence of this confinement potential in or near the drain lead could also explain the slightly asymmetric splitting of the heavy holes in the negative bias direction and the strong density of states behavior from the drain lead as shown in Fig. 4.5. The observation of the heavy hole excited state in the negative bias region over the full magnetic field range agrees with the model of asymmetric barriers and an increase of the slow tunnel-in rate in this bias condition. The observed change in current in the positive bias region indicates that the excited states must affect the tunnel-out rate in this region. The tunnel-out rate is only affected if the tunnel-out process from the excited state plays a role, which indicates that the relaxation rate between the excited state and the ground state has to be slower than this tunnel-out rate. This would explain the disappearance of the excited state lines in the higher magnetic field region, as the relaxation rates of the spin-excited states are expected to increase with magnetic field.

4.5 Magnetic field directional dependence

The dependence of the Zeeman splitting of the A^0 ground state on the direction of the applied magnetic field gives additional information about the origin of the observation of non bulk-like g-factors. The bias voltage trace at a magnetic field of 1 T applied along the x-axis, shown in Fig. 4.6a, was used as the starting point for this experiment. From this point the magnetic field was rotated 360° around the y-axis (see Fig. 4.1a) using a vector magnet.

The numerical differential conduction in Fig. 4.8a, shows a change in Landé g-factor as a function of the magnetic field direction, which is symmetric around 180° as expected for the rotational symmetry of silicon. Fig. 4.8b shows the g-factor dependence on the rotation of the magnetic field direction for the heavy and light hole states, assuming pure $\pm 3/2$ and $\pm 1/2$ states, giving Δm_j=3 and Δm_j=1. At 0° (i.e. with the magnetic field aligned with the x-axis), g-factors of $|g_{\Delta m_j=3}| = 0.81 \pm 0.02$ and $|g_{\Delta m_j=1}| = 0.74 \pm 0.06$ were found. The $|g_{\Delta m_j=1}|$ is smaller than the g-factor found in the low magnetic

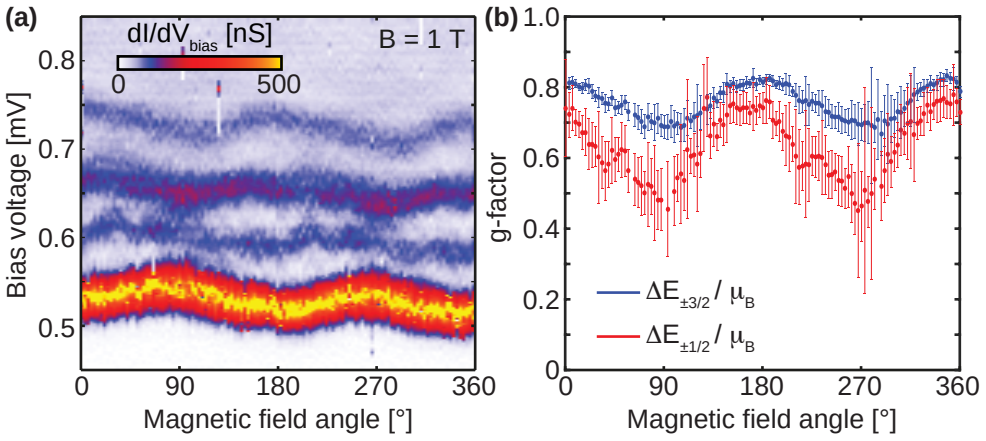

Figure 4.8: Landé g-factor dependence on magnetic field direction. **(a)** Directional dependence of the Zeeman effect on the A^0 state at a gate voltage of -75 mV and a magnetic field of 1 T, showing the numerical differential conductance. The magnetic field is rotated starting from the x-direction in 360° around the y-axis (axes are shown in Fig. 4.1a). **(b)** The dependence of the Landé g-factors, assuming Δm_j=3 and Δm_j=1, on the angle of the magnetic field. The energy differences between the two heavy hole and the two light hole states is calculated from four independent conductance peak fits, combined with the known lever arm 1-α_s.

field region, shown in Fig. 4.6. This is most likely caused by changes in the local environment of the atom, indicated by the nearby charge shift observed between 0.8 and 0.9 T. The smallest g-factors, $|g_{\Delta m_j=3}| = 0.70 \pm 0.05$ and $|g_{\Delta m_j=1}| = 0.48 \pm 0.08$, are found around a 90° rotation of the magnetic field.

This directional dependence of the Landé g-factor is compared to the dependence found for boron in bulk silicon.[75,78,79] By using the values for g_1' and g_2' reported by Köpf and Lassmann,[75] g-factors ranging from 1.13 to 1.14 for Δm_j=3 and from 1.08 to 1.18 for Δm_j=1 are calculated, in agreement with other experiments.[78,79] This gives a maximum relative change of 1 % for Δm_j=3 and 8 % for Δm_j=1. In the experiment presented here the maximum relative change in g-factor is found to be 14±8 % for Δm_j=3 and 35±16 % for Δm_j=1. Similar to boron atoms in bulk silicon, the magnetic field rotation has a stronger effect on the light hole states than the heavy hole states. However, the effect of the magnetic field rotation is significantly stronger in this experiment, highlighting the effect of the nano structure on the confinement of the hole.

From the measurement of the magnetic field directional dependence, information about the local environment of the atom can be deduced. A larger g-factor suggests a better alignment of the magnetic field with the quantization

axis of the confined holes. This quantization axis is set by the confinement symmetry of the hole, which depends on the local strain, electric field or the presence of a nearby interface. A possible explanation of the directional dependence observed here, is the influence of one of the Si/SiO_2 interfaces on the side of the channel, since the maximal g-factor is found near the x-direction. A full spherical rotation of the magnetic field should give a better description of the local environment of the atom.

4.6 Electric field dependence of Landé g-factor

The effect of the strength of the electric field on the first and second hole states of a single boron atom was investigated. In these experiments a tri-gate transistor was used with channel dimensions of 104 by 42 by 11 nm (length - width - height) and a background channel boron doping of 5 x 10^{17} cm^{-3}, fabricated on a SOI wafer. For this specific device 10 nm wide Si_3N_4 spacers are formed next to the gate. The experiments are performed at a temperature of 4.2 K, where the silicon substrate can be used as a back gate without the use of any light source. A 330 nH surface-mount inductor is attached to the top gate, and forms a tank circuit together with the $\sim$ 1 pF parasitic capacitance of this gate. This LC-circuit is driven by an rf signal close to the resonant frequency of 290 MHz. The input power was chosen just below the threshold where the observed charging lines start to broaden. This maximizes the signal to noise ratio, while maintaining thermally broadened line widths.

Many charge transitions were observed as a change in the amplitude of the reflected signal from the tank circuit, as shown in Fig. 4.9a. This experiment focussed on the two clear transition lines observed at top gate voltages less negative than -400 mV, i.e. in the low energy regime, and indicated as A^0 and A^+ in Fig. 4.9. These two charge transition lines have a similar slope and shift of amplitude in the reflected signal, as shown in Fig. 4.9a. Exactly two lines share these similarities in the low energy regime and are therefore attributed to the charging of one and two holes on a boron atom. In contrast, quantum dots would produce more lines as they are able to bind more than two holes. The top gate voltage where the charge transition was observed only changed when a voltage was applied to the drain electrode, and not to the source electrode (see Fig. 4.9b). This indicates that the boron atom is located in the proximity of the drain electrode.

The magnetic field dependence of the first and second hole transitions of the boron atom were measured for three different electric fields applied in the

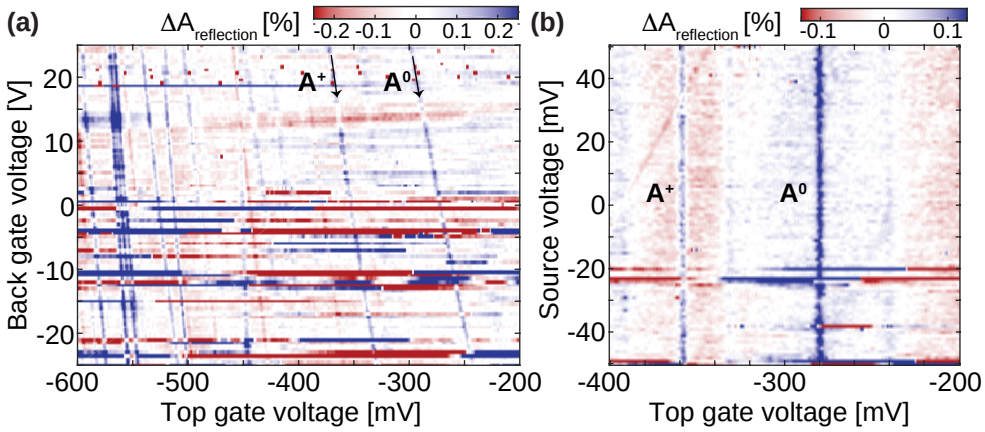

Figure 4.9: Charge transitions with rf reflectometry readout. **(a)** Charge transitions in a silicon tri-gate transistor measured as a change in the reflected amplitude of a tank circuit as a function of the voltages applied to the top and back gates. Two charge transitions are identified by the addition of the first hole (A^0) and second hole (A^+) to a boron acceptor in the transistor. **(b)** The same transitions, now as a function of the applied source and top gate voltages. As these charge transitions are independent of the source voltage, they are identified as originating from the tunneling of holes between the drain electrode and a boron atom.

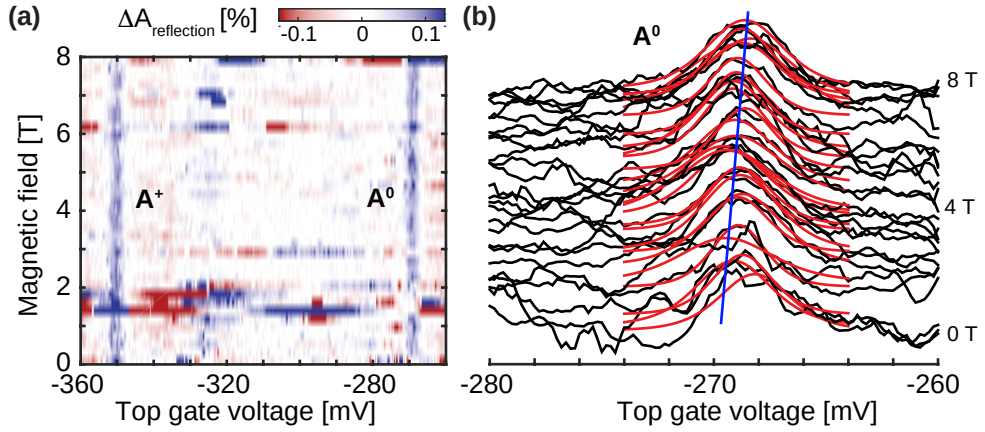

Figure 4.10: Electric field dependence of the Zeeman effect. **(a)** Magnetic field dependence of the first and second hole charge transitions of the boron atom with an applied drain voltage of 10 mV and at a 0 V back gate voltage. **(b)** The first hole transition is fitted to a thermally broadened line shape, using the liquid helium temperature of 4.2 K, for magnetic fields ranging from 0 to 8 T (red lines). The width of the peaks gives a relative capacitive coupling of the atom to the top gate of $\sim$ 0.4 meV/mV. The peak positions are used to linearly fit the Zeeman effect (blue line).

Table 4.1: Electric field dependence of the Landé g-factor. Measurements like the one shown in Fig. 4.10 give effective g-factors g^* for both the first and second hole state of the acceptor at three different electric fields. The calculated g-factor and the heavy (λ) and light (κ) hole fractions of the ground state are shown.

V_{drain}	Δ E-field	$\|g_1^*\|$	$\|g_2^*\|$	g	λ^2	κ^2
10 mV	67 kV/m	0.71	0.73	0.72	0.49	0.51
0 mV	0 kV/m	0.94	0.78	0.86	0.59	0.41
-30 mV	-200 kV/m	1.42	0.63	1.03	0.88	0.12

transport direction, set by drain voltages of 10 mV, 0 mV and -30 mV. In Fig. 4.10 the charge transitions of the atom at a 10 mV drain voltage and 0 V back gate voltage are shown for applied magnetic fields up to 8 T, perpendicular to the transport direction. This drain voltage results in a $\sim$ 10 mV shift in top gate voltage of the transition lines compared to those shown in Fig. 4.9. The transitions were fitted as temperature broadened reflectometry signals.[129] From these fits the lever arm of the top gate was established to be 0.40 meV/mV for the A^0 and 0.39 meV/mV for the A^+ transitions. This supports the interpretation of these signals as originating from the same confinement site, located close to the drain reservoir. A linear magnetic field dependence was extracted from the peak positions in gate voltage, shown in Fig. 4.10b, using the calculated lever arms. The results of the measurements for three different drain voltages are presented as $|g^*| = |g\, m_j|$, see table 4.1.

The combination of the magnetic field dependence of both the first and second hole are used to extract the effect of the electric field on the g-factor and on the total angular momentum of the hole states separately. The charging energy of the atom is estimated at 32 meV, using the difference in top gate voltage of the first and second hole transitions and the top gate lever arm of 0.40 meV/mV. Because this charging energy is lower than the bulk value for a boron atom, the assumption that the holes are pure $\pm 3/2$ and $\pm 1/2$ states is not valid for this particular atom. For the small electric field applied perpendicular to the magnetic field in this experiment, the quadratic field effect can be neglected and the $m_j = +3/2$ state is mixed with the $m_j = +1/2$ state, while the $m_j = -3/2$ state is mixed with the $m_j = -1/2$ state. These states are written as:

$$\lambda\ |-3/2> + \kappa\ |-1/2>, \tag{4.3}$$

$$\lambda\ |-1/2> + \kappa\ |-3/2>, \tag{4.4}$$

$$\lambda \; |+1/2> + \kappa \; |+3/2>, \tag{4.5}$$

$$\lambda \; |+3/2> + \kappa \; |+1/2>, \tag{4.6}$$

where $\lambda^2 + \kappa^2 = 1$. In the case of $\lambda = 1$ and $\kappa = 0$, the pure $\pm 3/2$ and $\pm 1/2$ states are recovered. If the small cubic dependence of the g-factor on total angular momentum, g_2', is neglected and an equal g-factor is assumed for both the heavy and light holes, the state defined in equation 4.3 is the ground state with an effective g-factor of:

$$g_1^* = -3/2 \; g \; \lambda^2 - 1/2 \; g \; \kappa^2. \tag{4.7}$$

The effective g-factor for the second hole is given by:

$$g_2^* = -1/2 \; g \; \lambda^2 - 3/2 \; g \; \kappa^2. \tag{4.8}$$

Using Eqs. 4.7 and 4.8 the g-factor, λ, and κ were calculated. The mixing decreases as the drain voltage becomes more negative. In this voltage direction the g-factor increases, due to the perturbation of the local environment of the acceptor atom. The acceptor states can be changed from completely mixed states at 10 mV drain voltage to states with a predominantly heavy hole and light hole character at -30 mV drain voltage. These findings are summarized in table 4.1.

4.7 Conclusion

In this chapter the addressing of single boron atoms in nano-scale transistors, using both electrical transport and rf gate reflectometry measurements, was shown. This study demonstrates the possibility to have a bulk-like atom in a nano-structure in terms of charging energy, excited state spectrum and the fourfold degeneracy of the acceptors ground state. This observation validates the prospect of controlling both heavy and light hole states of acceptors in nano-devices. The control over the heavy and light hole character of the acceptor states and the Zeeman effect on these states was investigated by the study of their dependence on the magnetic field direction and the strength of the electric field. These results demonstrate that electrostatic control of a single acceptor can be obtained in a nano-scale transistor, without losing the unique signature of the Coulomb confinement, i.e. a fourfold degenerate ground state.

chapter 5

Coupled acceptor atoms

Two level systems with strong spin-orbit coupling are of particular interest for scalable quantum information technologies as they can be controlled by alternating electric fields and coupled to cavity modes or phonons. A possible realization of such a spin-orbit qubit is based on the strong spin-orbit coupling between the heavy and light hole states of an acceptor atom in silicon. In this chapter the study of the interaction between the heavy and light hole states is presented. This study is based on measurements of coupled boron atoms in a tri-gate transistor, using both the rf gate reflectometry and transport measurement techniques. In the Pauli spin blockade regime of two holes bound to the acceptors, the heavy-light hole splitting and heavy-light hole mixing are probed by the investigation of the relaxation time of this two-hole system. The heavy-light hole relaxation rate is found to follow the expected $(\hbar\omega)^3$ behavior and is strongly influenced by the heavy-light hole mixing. Furthermore, the two-hole excited state spectrum is measured by magneto-transport spectroscopy and shows a change in quantization axis around 1 T. This indicates a g-factor of around 1 for both acceptors in the high magnetic field limit.

Part of this chapter is in preparation as:

- J. van der Heijden, T. Kobayashi, M.G. House, J. Salfi, S. Barraud, R. Laviéville. M.Y. Simmons and S. Rogge, *Spin-orbit induced spin dynamics of two coupled atoms in silicon.*

5.1 Introduction

The unique and highly tunable spin system of single acceptor atoms in silicon, consisting of heavy and light hole states, is largely unexplored. Due to the strong spin-orbit coupling between the heavy and light holes, acceptor atoms form potential spin-orbit qubits.[93,107,109] These qubits are advantageous for their all-electrical qubit control by local gates[102,149] and their long-range qubit coupling via the interaction with microwave cavities[104] and phonons.[160] These promising properties have recently led to an increasing number of studies of confined holes in silicon, both theoretically[93,109,161,162] and experimentally.[91,117,147–149]

Until now, experiments on boron ensembles have only probed the spin dynamics of the heavy and light hole states in specific cases, such as the highly strained acceptor system.[112] The main complication for these measurements is the inhomogeneous broadening of the resonance signal, originating from the splitting and mixing of the acceptor states by local strains and electric fields. This can be resolved by addressing individual acceptor atoms which can be measured using scanning tunneling spectroscopy[89,91] or in transport experiments on Schottky barriers[28,88] and CMOS transistors.[117] The study of single acceptors in silicon offers the possibility to probe these atoms in the presence of small strains and electric fields, the conditions expected to be needed for the realization of a robust spin-orbit qubit,[93,109] which remains a difficulty to measure in ensembles of acceptor atoms.

In this chapter the investigation of the spin dynamics of two holes on two boron atoms in a silicon tri-gate transistor are presented. In this structure the interactions between the heavy and light hole states are measured using a combination of hole transport[117,147,148] and rf gate reflectometry techniques,[126–129] as shown in Fig. 5.1. The double acceptor transport measurements give information about the excited state spectrum, which relate directly to the light-heavy hole splitting (Δ_{LH}) and the exchange coupling between light and heavy holes (J_{LH}). The spin state of the double hole system is probed at the crossover point between one hole on each acceptor (the (1,1) state) and both holes on one acceptor (the (2,0) state). When these two states are on resonance, a hole can tunnel between the two acceptors, creating a superposition of both states, which is detected as a frequency shift in the reflection of the LC-circuit coupled to the top gate.

5.2 Experimental setup

The silicon tri-gate transistor, as shown in Fig. 5.1, is fabricated using standard CMOS technology, similar as previously reported[128,148,163] and outlined in chapter 3. The channel, defined by the top gate, is 11 nm high, 42 nm wide and 54 nm long. On both sides of this gate, 25 nm long Si_3N_4 spacers form barriers to the highly doped source and drain regions. With a background boron doping of $5 \times 10^{17}/cm^3$, about 10 boron atoms are expected in the transistor channel and about 10 boron atoms under the spacers. In a dilution refrigerator at a base temperature of 40 mK, hole transport and rf gate reflectometry measurements give complementary insights in the static and dynamic behavior of the two-hole system of interest.

The noise floor of the transport measurement (∼100 fA) allows to detect currents with a total tunnel rate down to 500 kHz. A surface mount 270 nH inductor, attached to the top gate, forms a tank circuit together with a parasitic capacitance of ∼0.3 pF, as shown in Fig.5.1. Tunnel events in the transistor with a tunnel rate higher than or equal to the resonant frequency of 583 MHz result in a change of the reflected amplitude and phase of this

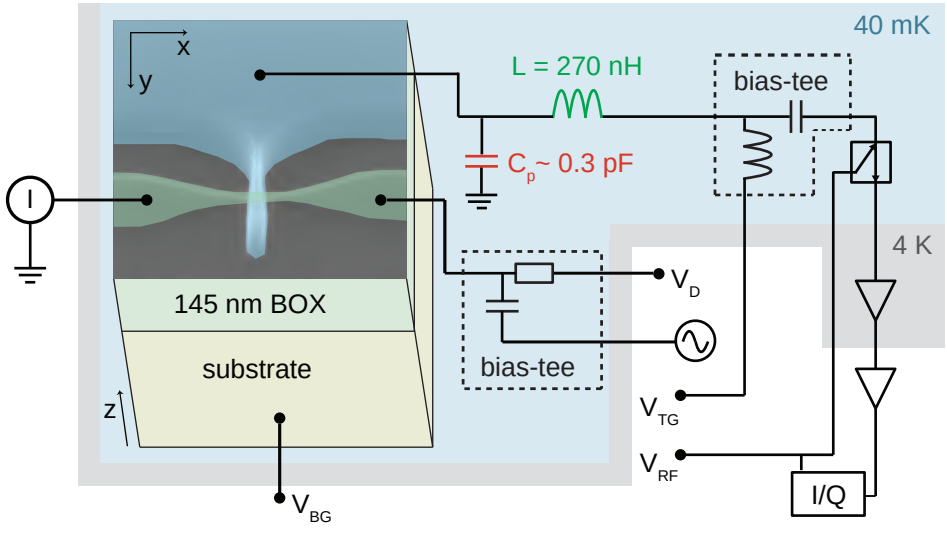

Figure 5.1: Experimental setup. SEM image of the used tri-gate transistor in the schematic diagram of the experimental setup for transport and rf gate reflectometry measurements. A tank-circuit is connected to the top gate in a homodyne detection setup, where a bias-tee allows for the rf and dc control of this gate. Another bias-tee is connected to the drain electrode, which allows to address the acceptors with microwaves. The silicon substrate is used as a global back gate. The SEM image has been provided by Leti.

resonator, as explained in chapter 3. Furthermore, low intensity light was directed to the silicon chip through an optical fibre to enable the use of the substrate as a back gate.

5.3 Identification of coupled acceptors

The charging of a boron atom is observed as a phase or amplitude shift of the reflected rf signal, caused by a change in admittance of the LC-circuit when a hole tunnels in the transistor channel. In Fig. 5.2 the measured hole transport at a low bias voltage is shown (blue color) as a function of the top gate and back gate voltages. Reflectometry shifts at energies lower than the transport signal onset, which is further to the top right of Fig. 5.2, indicate the resonant tunneling between a single lead and a localised site in the channel. In this map of top and back gate voltages, a line in the reflectometry signal corresponds to the equipotential of the localised site with the Fermi level of the lead, where the slope equals the capacitive coupling ratio between the top and back gate (α_{TG}/α_{BG}). Multiple lines with equal slopes (indicated by grey arrows in Fig. 5.2) imply the charging of several charge states of a quantum dot, formed unintentionally at the Si/SiO_2 interface.[118] In contrast, a boron

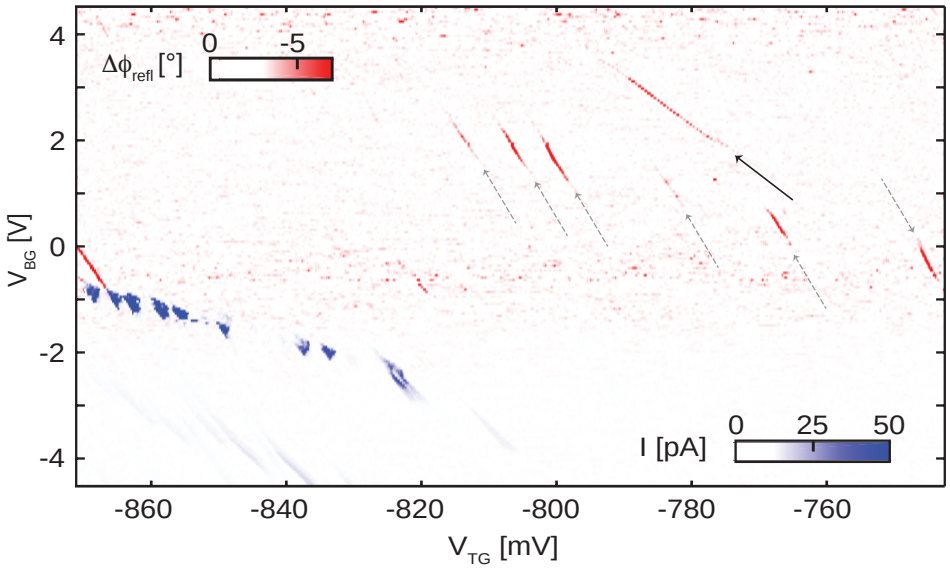

Figure 5.2: Top gate versus back gate stability diagram. The change in the reflected phase from the tank circuit (red) is compared to the measured current (blue), both at 1 mV V_D. The signals of an acceptor (black arrow) and an unintentional quantum dot (grey arrows) are identified.

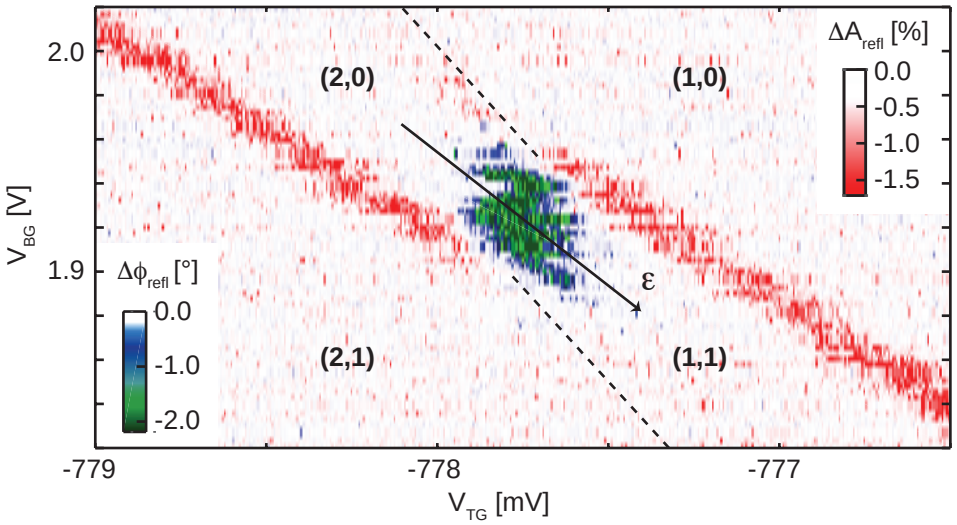

Figure 5.3: Charge stability diagram of two coupled acceptors. The reflected amplitude (red) and phase (blue/green) response showing a break in the acceptor-drain charging, caused by the charging of a nearby second acceptor atom. The different charge regimes are labelled for clarity.

atom would produce at most two charging lines, as it can only bind one or two holes. The boron atom studied here, is identified by a single line (indicated by a black arrow in Fig.5.2), which corresponds to the charging of the first hole onto this acceptor atom.

The signature of the charging of another boron atom nearby is seen as a sudden electrostatic shift in the charging signal of the acceptor, as shown in Fig. 5.3. A negative phase response in the reflectometry signal is found within the break of the line, which indicates the tunneling of holes between the two atoms. The tunneling of holes between this second acceptor and either the source or drain is not detected, which suggests a tunnel rate for this transition which is reasonably smaller than the resonance frequency of the tank circuit ($\Gamma \ll 583MHz$). In Fig. 5.3 dashed lines are drawn where the charging of the second acceptor is expected and the charge configurations of the two acceptors, as explained later in this chapter, are shown in this charge stability diagram.

5.3.1 Estimation of tunnel rates

The frequency response of the reflected signals reveals more information about the tunnel rates involved in both the acceptor-lead tunneling and the inter-acceptor tunneling. In Figs. 5.4a and 5.5a the amplitude and phase response around the resonance of the LC circuit are shown (black lines) and compared

to the slightly shifted signals when holes can either tunnel between the drain and one acceptor (blue lines) or between the two acceptors (red lines). The measured shift from the unperturbed resonance is shown as a function of frequency and drain voltage in Figs. 5.4b and 5.5b, where V_{BG} and V_{TG} are chosen such that V_D cuts through the middle of the inter-acceptor transition and the broken acceptor-drain tunnel signal shows up both on the left and the right side. A clear difference in frequency response is found between the acceptor-drain and the inter-acceptor tunnel signals, which is further illustrated by line-cuts through both signals as shown in Figs. 5.4c and 5.5c.

The difference in response of the LC-circuit can be explained by a difference in tunnel rate between these two processes,[129] as explained in chapter 3. In the case where the tunnel rate is much faster than the resonance frequency ($\Gamma \gg \omega$) of the LC-circuit, the tunnel process will predominantly add a capacitance to the circuit (dispersive response), which shifts the resonance to a lower frequency. In the case where the tunnel rate is of the order of the resonance frequency ($\Gamma \sim \omega$) of the LC-circuit, the tunnel process will predominantly add impedance to the circuit (dissipative response). Depending on the pre-existing matching conditions of the circuit, the added impedance can either increase or decrease the Q-factor of the resonator.

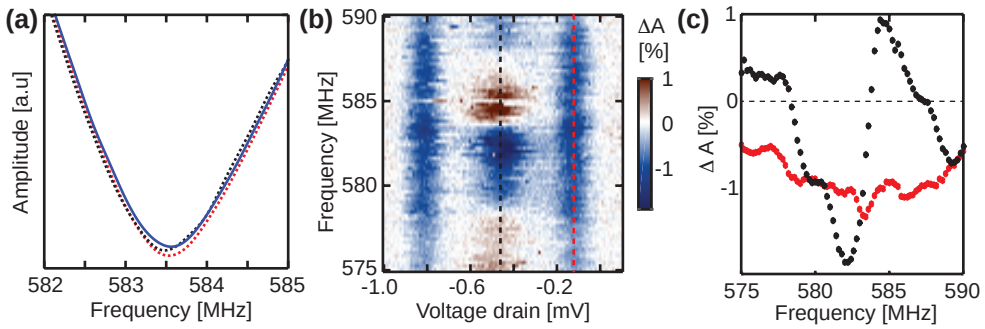

Figure 5.4: Amplitude change of reflection. **(a)** Amplitude response of the tank circuit as a function of frequency when: i) no resonances are found in the transistor (blue line), ii) holes tunnel between one acceptor atom and the drain (dotted red line), iii) holes tunnel between the two acceptor atoms (dotted black line). **(b)** Shift of the resonators response in amplitude, compared to the black line in **(a)**, as a function of frequency on a line cut through the (1,1)-(2,0) transition. Here V_{BG} is 1.93 V and V_{TG} is -777 mV, where V_D is used to sweep through the two acceptor-drain lines (left and right) and the inter-acceptor line (middle), as shown in Fig. 5.3. The distinct different frequency dependence of these tunnel processes is explained by the difference in tunnel rate for these transitions. **(c)** Amplitude shift for the line-cuts on the black and red dotted lines in **(b)**.

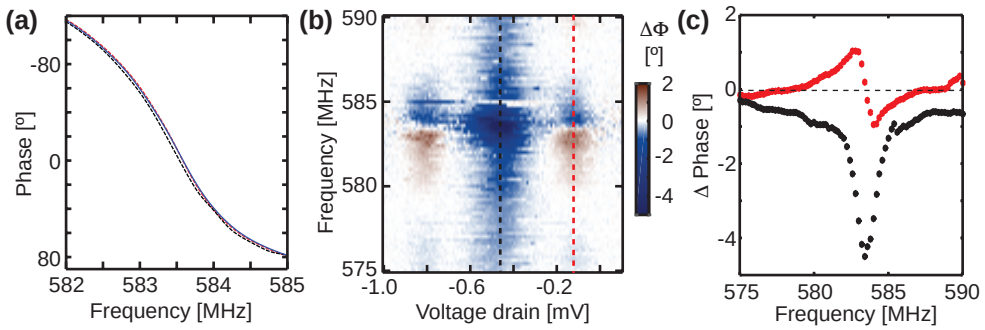

Figure 5.5: Phase change of reflection. **(a)**, **(b)** and **(c)** are identical to Fig. 5.4, only now showing the phase response of the tank circuit.

The acceptor-drain transitions show a reflected phase shift which changes polarity around the resonant frequency, while maintaining a negative reflected amplitude shift. This demonstrates an increase in Q-factor of the circuit, which therefore implies a tunnel rate comparable to the resonant frequency of 583 MHz. The inter-acceptor transition shows a negative reflected phase response, peaked around the resonance, while the reflected amplitude shift changes polarity at this point. This demonstrates a shift in resonant frequency, which therefore implies a tunnel rate much faster than the resonant frequency.

5.3.2 Estimation of capacitive coupling

The relative capacitive coupling of the acceptor to the drain and top gate is found by fitting the line shape of the acceptor-lead reflectometry signal. The hole temperature is estimated from the quantum dot transport at ∼300 mK, which gives $k_bT \gg \hbar\Gamma$ for the acceptor-lead tunneling process and thereby justifies a thermally broadened fit.[129] This gives a relative coupling to the top gate (α_{TG}) and drain (α_D) of 0.50±0.01 and 0.41±0.02 respectively, and places this atom roughly halfway between these electrodes, under the Si_3N_4 spacer. The second boron atom is likely to be located closer to the centre of the channel, as it is only observed through the inter-acceptor tunnel process, where the tunneling to both the source and drain is too slow to be detected.

5.4 Pauli spin blockade

The signature of Pauli spin blockade is the disappearance of the reflectometry inter-acceptor tunnel signal when a magnetic field is applied along the axis of the top gate nanowire (y-direction in Fig. 5.1a), as shown in Fig. 5.6a.

This indicates the presence of an even number of holes in the two-acceptor system. The inter-acceptor tunnel signal is therefore attributed to a (1,1)↔(2,0) transition, since a maximum of two holes can be bound to a boron atom in silicon. The exact occupation of the two atoms, extracted from pulsed experiments (discussed later), is shown in Fig. 5.3.

To model the spin blockade, the theoretical framework introduced for the two-hole system of coupled acceptors in chapter 2 is used. A distortion of the silicon cubic symmetry at the acceptor site lifts the degeneracy of heavy and light holes,[88,89] which in this experiment creates heavy hole ground states for both atoms. Note that the energy splitting to the light holes, Δ_{LH}, can be different for the two acceptors. The total energy of the two-hole system is constructed from the single particle energies plus the exchange energy J between the holes. In the (1,1) region the two holes are located on different atoms, therefore $\Delta_{LH} \gg J$ is assumed. The energetically lowest states in this region are the heavy hole singlet (S_{HH}) and triplet (T_{HH}) states. Here X_{HH} denotes the presence of two heavy holes, whereas a combination of one light and one heavy hole would be written as X_{LH}. In the (2,0) region the two holes are bound to the same boron atom and $J \gg \Delta_{LH}$. The six lowest states in this region are then composed of combinations of different spin states, making

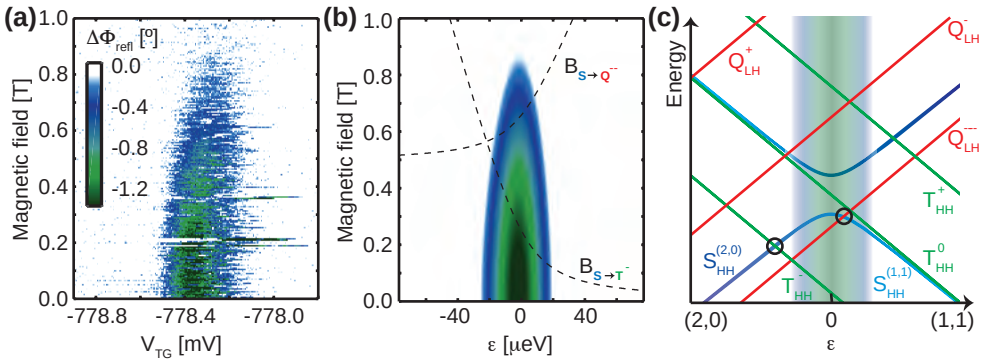

Figure 5.6: Pauli spin blockade. **(a)** Measured magnetic field dependence of the inter-acceptor tunneling phase response. The disappearance of the signal is caused by hole spin blockade and reproduced using Eqs. 5.3 and 5.4 in **(b)**. Dashed lines show the magnetic field dependence of the singlet crossing points with the triplet ($B_{S\to T}$) and quadruplet ($B_{S\to Q}$) states. **(c)** The energy diagram of two holes bound to two acceptors at a finite magnetic field as a function of detuning energy. The shift in reflected phase is found for the holes tunneling between the (2,0) and (1,1) S_{HH} states around the zero detuning point. The $S_{HH} - T^{-}_{HH}$ and $S_{HH} - Q^{--}_{LH}$ crossings are marked with black circles.

the heavy hole singlet (S_{HH}) the ground state. Four states consisting of one heavy hole and one light hole, form a quadruplet (Q_{LH}) found Δ_{LH} higher in energy. The exchange interaction between heavy and light holes J_{LH} splits this quadruplet in a singlet and triplet state.[93] Finally, the light hole singlet (S_{LL}) is found another Δ_{LH} higher in energy. The energy diagram as a function of detuning is shown in Fig. 2.3. As a reminder, the (1,1) states are given by:

$$\begin{aligned} S_{HH} &= \frac{1}{\sqrt{2}}\left([\Uparrow,\Downarrow] - [\Downarrow,\Uparrow]\right), \\ T^{-}_{HH} &= [\Downarrow,\Downarrow], \\ T^{0}_{HH} &= \frac{1}{\sqrt{2}}\left([\Uparrow,\Downarrow] + [\Downarrow,\Uparrow]\right), \\ T^{+}_{HH} &= [\Uparrow,\Uparrow]. \end{aligned} \tag{5.1}$$

And the (2,0) states are given by:

$$\begin{aligned} S_{HH} &= \frac{1}{\sqrt{2}}\left([\Uparrow\Downarrow] - \Downarrow\Uparrow]\right), \\ Q^{--}_{LH} &= \frac{1}{\sqrt{2}}\left([\Downarrow\downarrow] - [\downarrow\Downarrow]\right), \\ Q^{-}_{LH} &= \frac{1}{\sqrt{2}}\left([\Downarrow\uparrow] - [\uparrow\Downarrow]\right), \\ Q^{+}_{LH} &= \frac{1}{\sqrt{2}}\left([\Uparrow\downarrow] - [\downarrow\Uparrow]\right), \\ Q^{++}_{LH} &= \frac{1}{\sqrt{2}}\left([\Uparrow\uparrow] - [\uparrow\Uparrow]\right), \\ S_{LL} &= \frac{1}{\sqrt{2}}\left([\uparrow\downarrow] - [\downarrow\uparrow]\right). \end{aligned} \tag{5.2}$$

Using this framework, the magnetic field dependence of the reflectometry inter-acceptor tunnel signal is calculated, as shown in Fig. 5.6b. The shift in phase response of the reflected signal can be ascribed to the effective addition of a quantum capacitance (C_Q) to the LC-circuit,[126] which is linearly dependent on the curvature of the lines as function of detuning, as shown in the finite magnetic field energy versus detuning diagram in Fig. 5.6c. Only the lower (upper) singlet branch has a significant positive (negative) contribution to this capacitance, where the phase shift ($\Delta\phi$) depends on the occupation of these states given by the Boltzmann distribution:

$$\Delta\phi = C_Q \frac{e^{\left(-E_{S^-}/kT\right)} - e^{\left(-E_{S^+}/kT\right)}}{\sum e^{(-E_i/kT)}}, \tag{5.3}$$

with C_Q given by:

$$C_Q = \frac{1}{2}\alpha_\Delta^2 e^2 4t^2 \left(\epsilon^2 + 2t^2\right)^{-3/2}, \tag{5.4}$$

where E_{S_-} and E_{S_+} represent respectively the bonding and anti-bonding singlet states and E_i describes the energies of all the states involved. α_Δ represents the difference in capacitive coupling between each acceptor to the top gate, e is the electron charge, and t and ϵ are the tunnel coupling and the detuning between the acceptors respectively. A tunnel coupling of 4.3±0.3 GHz is estimated by identifying the microwave frequency at which holes are most efficiently excited from the bonding to the anti-bonding state,[163] as shown in chapter 6. Finally a α_Δ of 0.14, extracted from transport measurements, which are discussed later in this chapter, is used as an input for Eqs. 5.3 and 5.4 to model the Pauli spin blockade (see Fig. 5.6b). This gives a $S_{HH} - T^-_{HH}$ zero detuning crossing point at 0.25±0.05 T and a difference in effective Landé g-factor ($g* = g\Delta m_j$) between the T^-_{HH} and S_{HH} states of 1.2±0.3. The $S_{HH} - Q^{--}_{LH}$ crossing is also taken into account in the model, however it has only a small effect on the outcome of the model, which makes it difficult to extract the same values for the Q^{--}_{LH} state.

The Pauli spin blocked tunneling of holes between two acceptors can be used as a readout mechanism for the spin state of a hole bound to a single acceptor. This readout scheme, first introduced by Koppens et al.,[164] is performed at a finite magnetic field where the Pauli spin blockade is observed. In the (1,1) region, where the (1,1) T^-_{HH} is the ground state, independent control of the hole spins is possible. The flipping of one of these spins, by an electrically driven spin manipulation, and subsequent pulsing to the zero detuning readout point, prepares the system in either the S_{HH} or T^0_{HH} state. The occupation of the S_{HH} state is measured as a phase shift of the rf gate reflectometry signal, which can therefore be used as the readout of the spin flip process of the single hole spin.

5.5 Relaxation rates in the two-hole system

The inter-acceptor tunnel signal, which disappears in a magnetic field (Fig. 5.6a), is recovered by applying a voltage pulse to the drain electrode. This recovered signal is shown in Fig. 5.7a, where the time-averaged amplitude and phase response of the reflected signal are displayed for an applied voltage pulse of 0.8 mV to the drain for 40 out of every 200 ns at a magnetic field of 1.5 T. At this magnetic field, the break in the line of the acceptor-lead tunnel signal is displaced by the Zeeman-energy of the T^-_{HH} ground state. The recovered reflected phase shift caused by the inter-acceptor tunnel process indicates the occupation of the S_{HH} state at the zero detuning point, which is utilised to explore the

spin dynamics of the two-hole system using time resolved spectroscopy of the reflected signal. Fig. 5.7b shows the time dependence of the phase response at a magnetic field of 1.5 T with a voltage pulse applied between the ϵ_0 and ϵ_1 points, marked in Fig. 5.7a, and averaged over $\sim 10^6$ pulse sequences. An exponentially decaying signal is observed, corresponding to the relaxation of the S_{HH} state with a relaxation time T_1 of 390±40 ns.

Fig. 5.8a shows the inverse of the obtained T_1 times as a function of magnetic field. The distinct behavior of the dependence of the relaxation time on magnetic field is interpreted by considering different relaxation processes between the S_{HH} state and lower energy states, as schematically shown in Fig. 5.8b. The T^-_{HH} crosses the S_{HH} state at a magnetic field $B_{S\to T^-}$ of ~0.25 T, leading to the decrease of the reflected phase signal in Fig. 5.6a. At magnetic fields higher than $B_{S\to T^-}$ the S_{HH} state relaxes to the (1,1) T^-_{HH} state with a relaxation rate $\Gamma_{S\to T}$. This process requires a heavy hole spin-flip, which is, similar to the light hole relaxation discussed in chapter 2, expected to have a $(\hbar\omega)^5$ dependence and is considered as a relatively slow relaxation process. It is found that this relaxation does not significantly contribute to the measured relaxation rate. Furthermore, the (2,0) Q^{--}_{LH} state crosses the S_{HH} state at a magnetic field $B_{S\to Q^{--}}$. At magnetic fields above $B_{S\to Q^{--}}$, the relaxation from the S_{HH} state to the Q^{--}_{LH} state, $\Gamma_{S\to Q}$, involves a heavy to light hole relaxation. This relaxation process dominates for magnetic fields above 1.5 T and follows the expected $(\hbar\omega)^3$ behavior,[93,107] as outlined in chapter 2. The

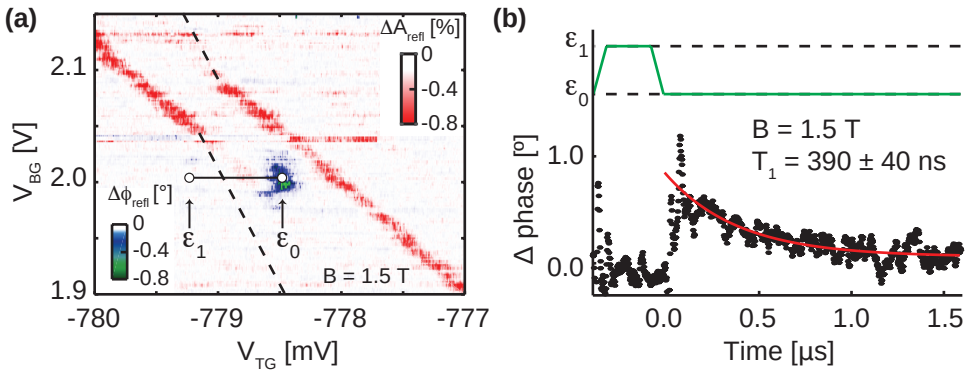

Figure 5.7: Initialization pulse and time dependent measurement. **(a)**Time averaged rf reflectometry amplitude (red) and phase (blue) measurement for a 0.8 mV, 5 MHz pulse with 20-80 duty cycle, applied to the drain, at a magnetic field of 1.5 T. **(b)** The time dependent phase signal for a pulse between the points ϵ_0 and ϵ_1, where the pulse sequence is shown at the top.

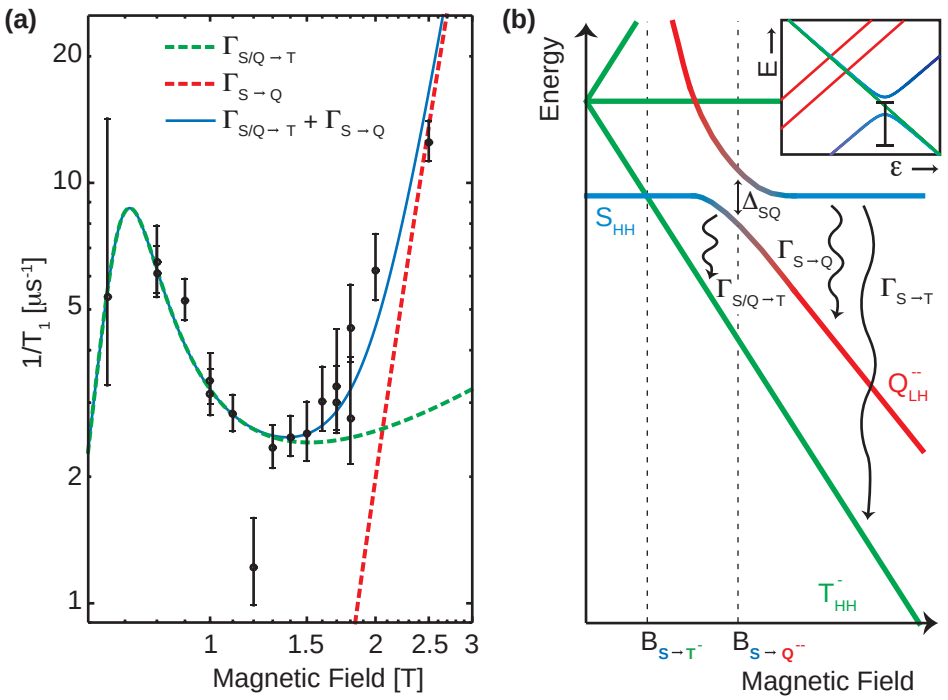

Figure 5.8: Relaxation times and mechanisms of the two-hole system. **(a)** Magnetic field behavior of the relaxation rate ($1/T_1$) in a range of 0.6 to 2.5 T. **(b)** Schematic view of the relevant relaxation rates in this system at the zero detuning point (see inset). The data in **(a)** is fitted by combining Eqs. 5.5 (red dashed line) and 5.6 (green dashed line) to get the total relaxation rate (blue solid line).

energy splitting $\hbar\omega$ for this relaxation is described as function of the magnetic field relative to the crossing point $B_{S\to Q--}$ and the mixing of the S_{HH} and Q^{--}_{LH} states represented by Δ_{SQ}. This relaxation rate is given by:

$$\Gamma_{S\to Q} = A_{SQ}\left(\sqrt{|B - B_{S\to Q--}|^2 + \Delta^2_{SQ}}\right)^3, \tag{5.5}$$

where A_{SQ} is the relaxation amplitude between the S_{HH} and Q_{LH} states. In the vicinity of $B_{S\to Q--}$ the mixing of the S_{HH} and Q^{--}_{LH} states, caused by heavy-light hole mixing, strongly influences the relaxation to the T^{-}_{HH} state. The partial light hole character of this mixed state gives rise to a light-heavy hole relaxation with a $(\hbar\omega)^3$ dependence. Here the energy splitting is approximated as a linear function of the magnetic field relative to the crossing point $B_{S\to T^-}$. Furthermore the relaxation amplitude depends on the light-hole character in the mixed state, which has a maximum at the mixing

point $B_{S\to Q^{--}}$. This relaxation rate is given by:

$$\Gamma_{S/Q\to T} = \frac{A_{QT}(B - B_{S\to T^-})^3}{|B - B_{S\to Q^{--}}|^2 + \Delta_{SQ}^2}, \tag{5.6}$$

where A_{QT} is the relaxation amplitude between the Q_{LH}^{--} and T^-HH states. This relaxation dominates this experiment below 1 T. The full magnetic field dependence of the relaxation rates (T_1^{-1}) is fitted by the sum of Eqs. 5.5 and 5.6, shown as a blue solid line in Fig. 5.8a. From this fit $B_{S\to Q^{--}}$ is extracted as 0.66±0.03 T and Δ_{SQ} as 0.17±0.02 T, when the $B_{S\to T^-}$ found from the Pauli spin blockade measurement is used as an input parameter.

5.6 Excited states of the two-hole system

5.6.1 Zero magnetic field measurement

Hole transport measurements provide the full two-hole excited state spectrum, which cannot be obtained with rf reflectometry measurements due to insufficiently slow tunnel rates to give a signal using this measurement technique. In Fig. 5.9a the transconductance signal (dI/dV_{TG}) as a function of V_{TG} and V_{BG} at a drain voltage of 10 mV shows a bias triangle (dashed lines), demonstrating sequential hole tunneling via both acceptors in series. The bias triangle starts to emerge at source-drain voltages above 3 mV, indicating that this sequential tunnel process is blocked in the low bias regime. The slope of the edges of the triangles are given by the ratio between the coupling to the top gate and back gate. The slope of the base line of the triangle comes from the difference in the coupling to the top and back gate, which was used earlier to estimate α_Δ in Eq. 5.4.

The specific bias direction gives a transport direction for the holes from the drain to the source. From the rf gate reflectometry experiments, as shown in Fig. 5.3, it is deduced that the acceptor with a charge transition from 0 to 1 hole has a stronger tunnel coupling to the drain (detectable with rf reflectometry) than the acceptor with a charge transition from 1 to 2 holes (not detectable with rf reflectometry). It follows that the probed sequential tunneling involves the (1,1)→(2,0) transition, where the two bias triangles are formed by the two possible charge transfer processes:

$$\begin{aligned}(1,0) \to (1,1) \to (2,0) \to (1,0),\\ (2,1) \to (1,1) \to (2,0) \to (2,1).\end{aligned} \tag{5.7}$$

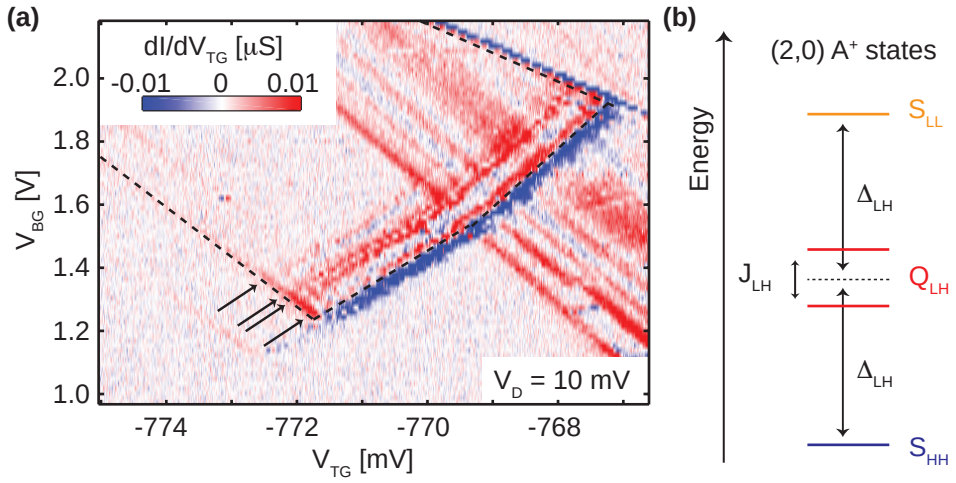

Figure 5.9: Sequential transport of coupled acceptors at zero magnetic field. **(a)** Transconductance dI/dV_{TG} as a function of the top and back gate voltages at a 10 mV V_D. The bias triangle, marked by dashed lines, shows three excited states parallel to the baseline. **(b)** Corresponding energy states of the A^+ state, as outlined in chapter 2.

At zero magnetic field the (1,1) S_{HH} and T_{HH} states are nearly degenerate. All higher lying (1,1) excited states include at least one light hole and are therefore expected to have a short relaxation time. For this reason the observed ground state and excited states, marked by arrows in Fig. 5.9a, are associated with the (2,0) energy spectrum shown in Fig. 5.9b. This spectrum is similar to the one reported for two holes bound to two closely located acceptors.[91] Furthermore, this energy spectrum does not show the regular spaced excited state spectrum as expected for a quantum dot. Consequently, the second confinement site has to be a second acceptor atom. From this spectrum a Δ_{LH} of 110±10 μeV and a J_{LH} of 36±5 μeV are extracted. This shows the first addressability of individual acceptors with a heavy-light hole splitting in the few hundred μeV range, which is of particular interest as it matches the regime where robust spin-orbit qubits have been proposed.[93]

5.6.2 Finite magnetic field measurement

The magnetic field dependence of the transition energy spectrum is studied by measuring the transconductance at V_{BG}=1.4 V, a cut through the bias triangle, in an increasing magnetic field in the y-direction, as shown in Fig. 5.10. The slope of the baseline of the triangle (dV_{TG}/dB) changes twice, around 250 mT

and 500 mT, as marked by the arrows. The first change in slope indicates the $S_{HH} - T^{-}_{HH}$ crossing at $B_{S\to T^-}$, in agreement with the spin blockade measurement in Fig. 5.6a. The second change in slope corresponds to the $S_{HH} - Q^{--}_{LH}$ crossing at $B_{S\to Q^{--}}$, in agreement with the origin of the observed relaxation rates in Fig. 5.8. It is noted that in the transport measurement this crossing does not occur at the zero detuning point but at the detuning where the (1,1) T^{-}_{HH} and the (2,0) S_{HH} are in resonance. This causes this crossing to appear at a lower magnetic field compared to the $B_{S\to Q^{--}}$ found earlier.

The magnetic field behavior of the (1,1)→(2,0) transition lines, shown in Fig. 5.10, describe the magnetic field dependence of the excited states of the (1,1) and (2,0) configurations. At zero magnetic field, Δ_{LH} reflects the effect of the local environment on the confinement of the two holes. Either the proximity of an Si/SiO_2-interface, the local strain or the presence of an electric field can break the cubic symmetry of silicon and give rise to this heavy-light hole splitting. However, the direction of the resulting quantization axis for the hole spins is unknown, making it impossible to predict the exact Zeeman interaction in the low magnetic field range.

In a large magnetic field, the Zeeman energy becomes the dominant en-

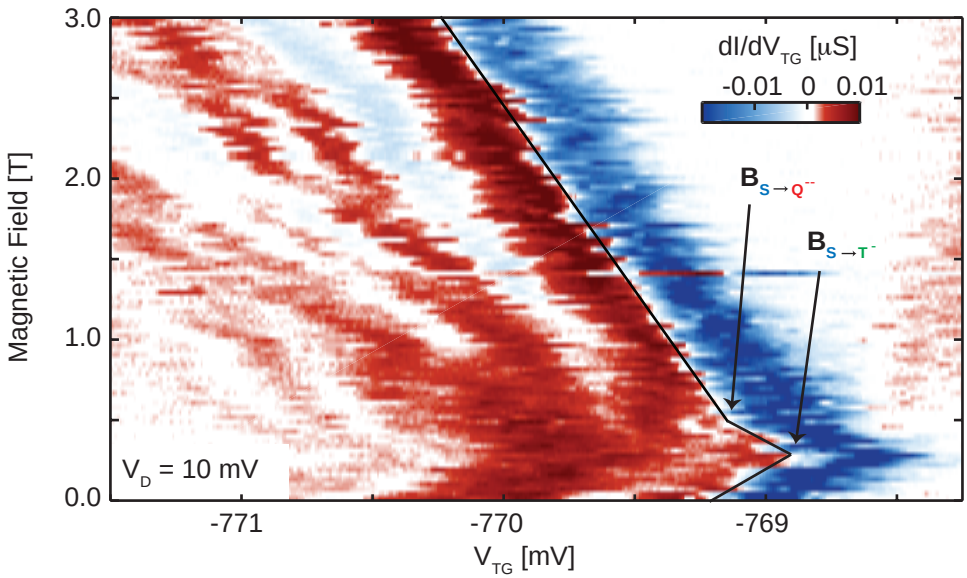

Figure 5.10: Magnetic field dependence of sequential transport of coupled acceptors. The transconductance at 1.4 V V_{BG} is shown. Arrows indicate shifts of the baseline at the points of the $S_{HH} - T^{-}_{HH}$ and $S_{HH} - Q^{--}_{LH}$ crossings.

ergy scale and a quantization of the angular momentum in the y-direction is considered. If the perturbation in this direction is small, the heavy and light hole states at high magnetic field can be described by a total angular momentum of $\pm 3/2$ and $\pm 1/2$ respectively. This results in a total angular momentum of {3, 0, -3} for the T_{HH} states and {2, 1, -1, -2} for the Q_{LH} states, where all singlet states have a zero total angular momentum. Under these assumptions, all possible (1,1)→(2,0) transitions can be simulated, as shown in Fig. 5.11, where the relevant Landé g-factors and the heavy-light hole splitting in the y-quantization axis (Δ_{LH}^{y}) are input parameters. The slopes of the measured (1,1)→(2,0) transition lines, shown in Fig. 5.10, are used to estimate the g-factors of both acceptor atoms, while the zero-field crossing points gives an estimate of Δ_{LH}^{y}. For the double occupied acceptor, a $g_{3/2}$ of 0.85 and a $g_{1/2}$ of 1.07 with a Δ_{LH}^{y} of 30 μeV are extracted, using α_{Δ} to convert the voltage scale to an energy scale. For the single occupied acceptor only the heavy hole g-factor, estimated at 1.05, contributes to the T_{HH} states. Furthermore, it is noted that the excited state line corresponding to the crossing of the (1,1) T_{HH}^{-} and the (2,0) S_{HH} disappears at a magnetic field around 2 T. This indicates that this transition, expected to be spin-blocked, is still partially allowed at low magnetic fields. At high magnetic fields, however, the mixing of the hole states diminishes and this transition becomes spin-blocked.

In the analysis of the magnetic field behavior of this transition, only the lowest (1,1) heavy hole manifold is considered. This is justified, as the T_{HH}^{-} has the strongest decrease in energy due to the Zeeman interaction and is therefore the ground state in the (1,1) region at magnetic fields above the $S_{HH} - T_{HH}^{-}$ crossing. It is recognized that some of the excited states from the higher lying manifolds will also decrease their energy due to the Zeeman interaction and thereby possibly cross states from the heavy hole manifold, yet this has no significant effect on the presented measurements. The lifetime of the excited states in these higher lying manifolds are expected to be short, due to the available light to heavy hole relaxation process. The observation of only one change of (1,1) ground state (the $S_{HH} - T_{HH}^{-}$ crossing), supports the fact that heavy holes form the lowest manifold, where in the case of a light hole ground state, a minimum of two changes of ground state are expected.

The observed g-factors in the high magnetic field limit are close to those found for bulk boron acceptors.[75,79] The effective g-factor in the low magnetic field limit can be calculated from the singlet-triplet crossing and is found to be three times as small under the same assumptions for the total angular momentum. Such a reduction of the g-factor when a magnetic field is applied

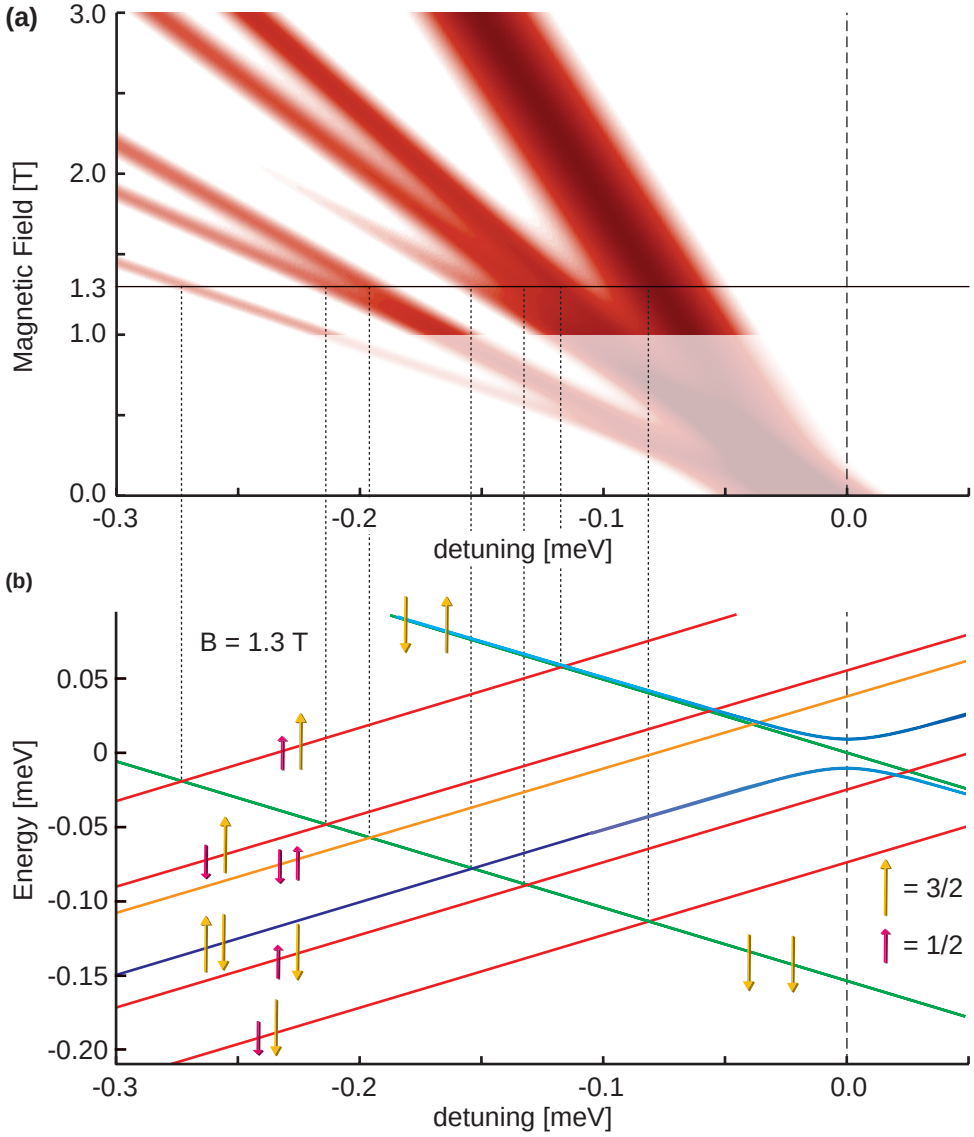

Figure 5.11: Simulation of magnetic field dependence. Comparison of the magnetic field dependence to a model describing the high magnetic field limit. Top panel: Overview of the (1,1)→(2,0) transitions at a magnetic field of 1.3 T, with the S_{HH} (blue), T_{HH} (green), Q_{LH} (red) and S_{LL} (orange) displayed. The total angular momentum of the two holes are indicated with arrows. Bottom panel: Full magnetic field behavior of the transition points.

in a different direction than the quantization axis, has been observed for holes in quantum dots[148] and predicted for holes bound to acceptors,[93] as described in chapter 2.

5.7 Conclusion

In conclusion, the spin dynamics of single acceptor atoms in silicon have been measured. RF reflectometry allows for the detection of holes tunneling between two boron atoms. Here the two-hole system is detected, where the signatures of Pauli spin blockade are measured when a magnetic field is applied. From time resolved spectroscopy, using a pulse detection technique, the relaxation time in the two-hole system is measured as a function of magnetic field. Here the heavy-light hole relaxation dominates, showing the expected $(\hbar\omega)^3$ behavior, which is the first experimental detection of this relaxation process for acceptor atoms. Furthermore, the mixing between heavy and light hole states has a strong influence on the relaxation process, which is measured as a hotspot-behavior. Furthermore, the complex magnetic field behavior of the two-hole excited states was probed using transport measurement techniques. In zero magnetic field the light-heavy hole splitting was measured at 110$\pm$10 μeV and the light-heavy hole exchange was measured at 36$\pm$5 μeV. By applying a finite magnetic field a change in quantization axis of the total angular momentum of the holes is observed. In the high magnetic field limit, the light-heavy hole splitting is reduced to 30 μeV and the g-factors of the two acceptors are found to be around 1, close to the known bulk value. The understanding of this two-hole system, in terms of the heavy-light hole splitting and especially the heavy-light hole mixing, is essential to create electrically driven acceptor qubits.

chapter 6

Microwave spectroscopy

Probing dopant systems in silicon using microwaves gives valuable insights into tunnel couplings, relaxation times and coherence times. Here, this approach allowed to extract the tunnel coupling between two coupled acceptors, by the resonant excitation of the two-hole system from a bonding to an anti-bonding state. A tunnel rate of 4.3 ± 0.3 GHz was directly measured, without prior knowledge about the g-factor or gate coupling. Furthermore, a single acceptor is probed in a Landau-Zener-Stückelberg interferometry configuration, and interferences in the rf gate reflectometry readout are measured. The acceptor-drain charge transition shows a coherence time around 60 ps. Another double acceptor system is probed by transport spectroscopy and photon-assisted tunneling between the two boron atoms in the single hole transport process is detected.

6.1 Introduction

Some of the most interesting single dopant systems in silicon operate at energy scales in the microwave frequency range. For two-level systems based on the spin states of individual atoms in silicon the relaxation rate generally increases with a power-law dependence on energy splitting.[165] Therefore systems with small energy splittings are preferable to realize long-lived qubit states. However, a lower bound is usually determined by the individual readout of both states, set by the finite temperature of the system. Experiments in dilution refrigerators are usually performed with electron and hole temperatures around 100 mK, where $k_B T/h$ corresponds to about 2 GHz, leading to promising quantum two-level systems in the microwave range.

For single impurity atoms in silicon, the Zeeman splitting reaches the GHz range at magnetic fields above ∼100 mT. Microwave spectroscopy is therefore a valuable tool to study these spin states. For donor atoms, the spin states can be manipulated with a microwave magnetic field, whereas for acceptors, due to the spin-orbit interaction, the transitions between the spin states can also be driven by microwave electric fields. Furthermore, for individual acceptor atoms, the heavy-light hole splitting is often found in the microwave range if the electric field and strain in the vicinity of the acceptor is not too large. For systems with multiple atoms or an atom coupled to one or more reservoirs, tunnel couplings within the system represent an important energy scale.

In this chapter the effect of microwave electric fields on the tunnel processes of different systems is presented. First in the coupled acceptor system introduced in chapter 5, holes were driven resonantly between the bonding and anti-bonding state of the heavy hole singlet. Then the tunneling of holes between one of these acceptors and the drain lead was investigated with Landau-Zener-Stückelberg interferometry. Finally, another system of two coupled acceptors was studied, where photon-assisted tunneling processes were induced by a microwave electric field.

6.2 Probing the tunnel coupling between two acceptors

The tunnel coupling between the two acceptors, presented in chapter 5, was measured by microwave spectroscopy. To estimate the tunnel coupling between the two acceptor atoms the resonance between the bonding (S^b_{HH}) and anti-bonding (S^a_{HH}) singlet heavy hole states was measured, similar to the

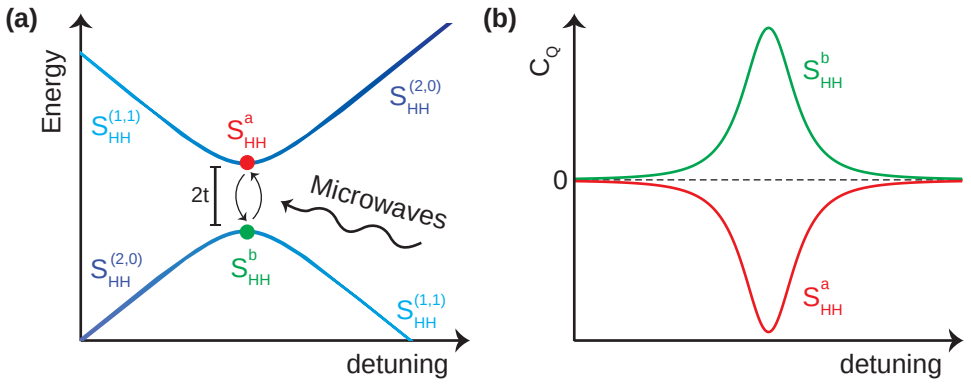

Figure 6.1: Microwave spectroscopy to estimate the tunnel coupling. **(a)** Schematic diagram of the two hole system, showing only the heavy hole singlet state. The microwaves drive the transition between the bonding (S^b_{HH}) and anti-bonding state (S^a_{HH}). **(b)** The quantum capacitance of the bonding (green) and anti-bonding (red) state as a function of detuning.

measurement of two electrons on a hybrid donor-quantum dot system.[163] The energy difference between the bonding and anti-bonding states is equal to twice the tunnel coupling when the (1,1) and (2,0) singlet states are brought in resonance, as shown in Fig. 6.1a. The energy of these states as a function of detuning is described by:

$$\begin{aligned} E_{bonding} &= E_0 - \sqrt{\epsilon^2 + (2t)^2}, \\ E_{anti-bonding} &= E_0 + \sqrt{\epsilon^2 + (2t)^2}. \end{aligned} \tag{6.1}$$

As shown in Eqs. 5.3 and 5.4, the quantum capacitances for the system in the bonding and the anti-bonding state are of opposite sign, as shown in Fig. 6.1b. Because of the polarization of this system at low temperature ($\sim$ 300 mK), the positive quantum capacitance of the bonding state dominates and results in the negative phase shift as presented in chapter 5. A microwave driven resonance decreases the polarization of the system and causes a decrease in the phase shift of the reflected signal.

A bias-tee coupled to the drain lead, shown in Fig. 5.1, is used to apply microwaves to the double acceptor system. In this experiment the inter-acceptor signal is continuously probed with rf gate reflectometry, while the microwaves are also continuously applied to the drain. The splitting of the acceptor-drain signal is used as a calibration to keep the input power for the acceptor system constant during the experiment by compensating for any frequency dependent losses in the connections and coaxial lines. This splitting depends linearly on the microwave power applied at the drain, as shown in

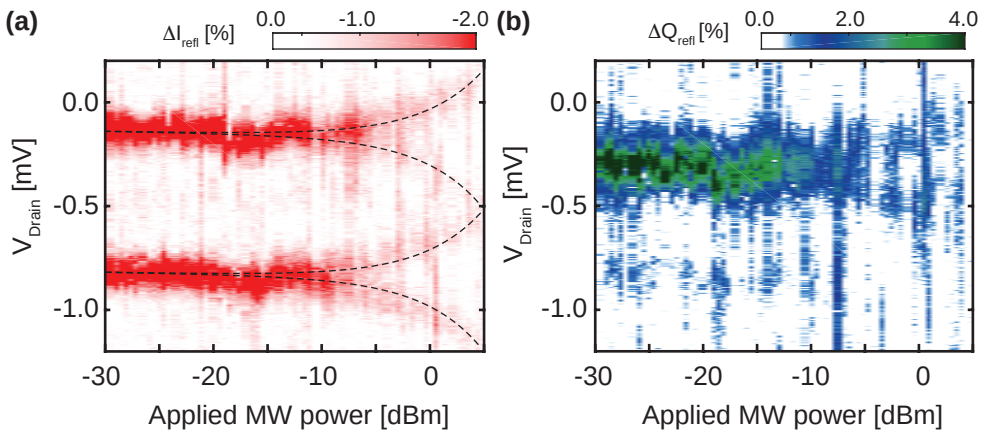

Figure 6.2: Reflectometry signal dependence on microwave power. **(a)** Shift in the I channel signal of the rf gate reflectometry readout at 7.6 GHz as a function of the applied microwave power, which shows the microwave induced broadening of the acceptor-drain resonance. **(b)** Shift in the Q channel of the rf gate reflectometry readout at 7.6 GHz as a function of the applied microwave power. This shows the decrease in the inter-acceptor tunneling, caused by the decreased population of the S^b_{HH} state and the increased population of the S^a_{HH} state.

Fig. 6.2a. This measurement is used to calibrate the system for a. An input power corresponding to a 50 μV splitting of the acceptor-drain signals is chosen as the reference point for every frequency. The applied power to reach this condition is shown in Fig. 6.3a.

The typical response of the inter-acceptor tunnel signal is shown in Fig. 6.2b. The phase shift of the inter-acceptor tunneling signal at the reference power, $\Delta\Phi$, is compared to the phase shift without any applied microwaves, $\Delta\Phi_0$. The ratio $\Delta\Phi/\Delta\Phi_0$ is shown as a function of the microwave frequency in Fig. 6.3b. The decrease in this ratio is fitted to a Gaussian function (red line in Fig. 6.3b). A centre frequency of this resonance is found at 8.6±0.6 GHz, corresponding to a tunnel coupling between the atoms of 4.3±0.3 GHz. The width of this resonance indicates a T_2^* of $\sim$ 200 ps for the bonding and anti-bonding states. This value is similar to the one found for a two-electron system on a hybrid donor-quantum dot in a similar tri-gate transistor.[163]

This direct measurement of the tunnel rate between the two acceptor atoms is particularly useful as it does not rely on prior knowledge of the g-factor and the gate coupling to both acceptors. Because for acceptors in silicon the g-factors strongly depend on the local environment of the atoms, in contrast to the g-factors of donor atoms, the tunnel rate can not easily be extracted from a spin blockade measurement. The tunnel rate determined by the microwave

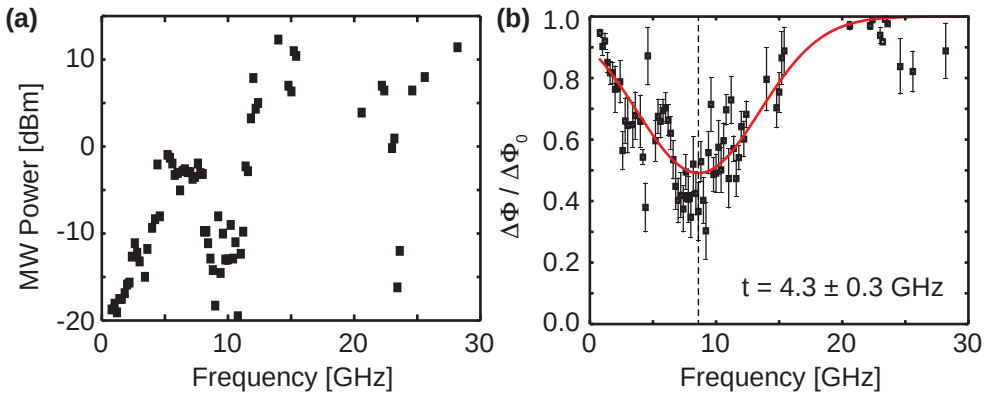

Figure 6.3: Estimation of the tunnel coupling. **(a)** The applied microwave power to achieve a 50 μV splitting of the acceptor-drain signal. **(b)** The change in phase shift of the inter-acceptor tunnel signal as a function of microwave frequency, using the microwave power as specified in **(a)**. The resonant decrease in signal is fitted with a Gaussian function. A tunnel coupling of 4.3 GHz between the atoms is extracted.

spectroscopy is ∼10 times the rf driving frequency of the LC-circuit coupled to the gate and confirms that this resonance mainly adds a quantum capacitance to this circuit.

6.3 Landau-Zener-Stückelberg interferometry

Landau-Zener (LZ) tunneling is the quantum mechanical effect to diagonally cross an avoided crossing between two energy levels that repel each other, as shown in Fig. 6.4a. The probability of such an event, P_{LZ}, is given by:

$$P_{LZ} = exp\left(-2\pi\frac{\Delta^2}{4\hbar v}\right), \tag{6.2}$$

where Δ is the energy spacing between the two levels at the avoided crossing point (zero detuning point), and v is the speed of crossing, given by $d\epsilon/dt$.

When a system is driven by microwaves, multiple LZ transitions can occur at an avoided crossing. The phase difference between the path where a LZ transition occurs and the path where the LZ transition does not occur causes interference patterns in the probability amplitudes found after multiple passages of the avoided crossing. These Stückelberg oscillations can be measured by the so-called Landau-Zener-Stückelberg (LZS) interferometry. The chance of finding the system in the diabatic excited state P_{ex} at a certain detuning ϵ depends on the energy splitting Δ, the speed and frequency of the crossings,

the population and phase coherence times T_1 and T_2:[166]

$$P_{ex}(\epsilon, A, \omega) = \frac{1}{2}\sum_n \frac{\Delta^2 J_n^2}{\frac{1}{T_1 T_2} + \frac{T_2}{T_1}(n\omega - \epsilon)^2 + \Delta^2 J_n^2}, \tag{6.3}$$

where A and ω are the amplitude and frequency of the microwave drive and J_n is the n-th Bessel function as a function of A/ω. An example in the interference pattern of the probability to find the system in the diabatic excited state is shown in Fig. 6.4b. LZS interferometry has been measured in a variety of systems, including transport measurements on single dopants in silicon transistors,[167] and rf gate reflectometry measurements on quantum dots in silicon transistors.[168]

For the coupled-acceptor system shown in chapter 5, LZS interferometry was measured for the acceptor-drain tunnel process. This microwave spectroscopy measurement was performed far detuned from the (1,1)-(2,0) crossing of the two acceptors. As a fast phase decoherence is expected for the drain reservoir, it is likely that the probed transition occurs instead between the boron atom and a confined state which is strongly coupled to the drain reservoir. No clear signature of LZS interferences was found for the tunneling of holes between the two acceptor atoms, possibly caused by an overlapping effect of the LZS fringes of the acceptor-drain signal in this region, thereby obscuring the LZS interference pattern of the inter-acceptor tunneling.

The measurement is performed by applying a continuous 23 GHz microwave with varying power. Fig. 6.5 shows the measured phase shift of the rf gate

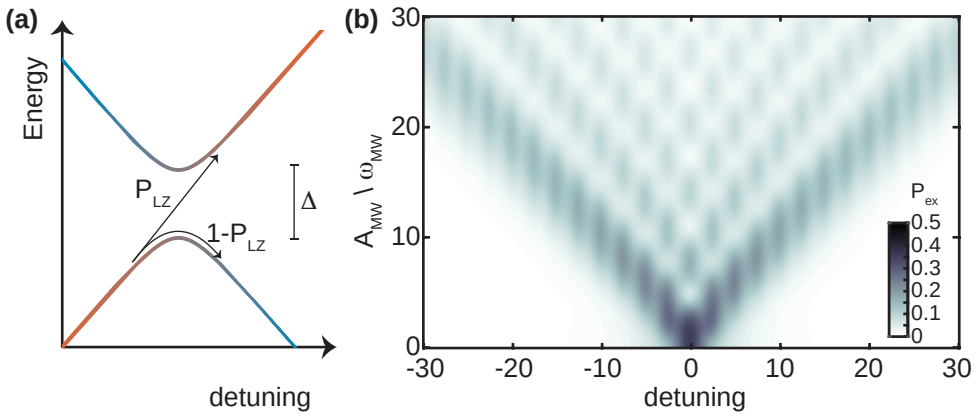

Figure 6.4: Landau-Zener-Stückelberg interferometry. **(a)** The Landau-Zener transition has a probability P_{LZ} to occur between the two levels. **(b)** Landau-Zener-Stückelberg interferometry pattern showing the chance of finding the system in the diabatic excited state, given by Eq. 6.3, where $T_1 = T_2 = \frac{\sqrt{3}h}{\Delta}$.

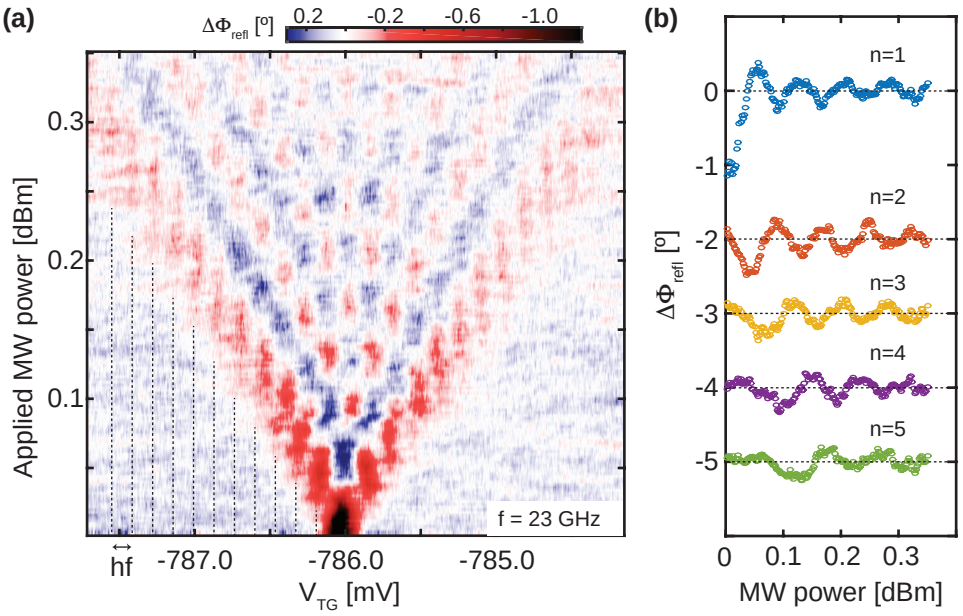

Figure 6.5: Acceptor-drain transition for 23 GHz microwaves. **(a)** Phase shift of the rf reflectometry signal as a function of the top gate voltage and the applied microwave power, showing the Landau-Zener-Stückelberg interferometry pattern. **(b)** Cuts through figure **(a)** showing the oscillating patterns for the first five photon transitions. The traces of the n=2 to n=5 photon transitions are offset by -n°.

reflectometry signal as a function of gate voltage. The LZS interference pattern seen in Fig. 6.5a shows up to 12-photon transitions, indicated by dotted lines. An n-photon transition only occurs if the microwave power is high enough to reach the avoided crossing. This leads to the typical V-shape appearance and gives an independent measure of the microwave amplitude at the acceptor-lead system.

The observation of both positive and negative phase shift in the interference pattern, shown in Fig. 6.5b, correspond to both positive and negative quantum capacitance. This can be explained by the positive and negative quantum capacitance in the upper and lower state of the avoided crossing, as shown in Fig. 6.1b, and observed in other reflectometry LZS interferometry measurements.[168,169]

At lower microwave frequencies the phase coherence is not preserved between each passage of the avoided crossing. This leads to the disappearance of the LZS interference pattern, shown in Fig. 6.6. The LZS interference pattern appears when the driving frequency is equal to T_2^*, which is found to be around 17.5 GHz in this experiment. This corresponds to a phase-coherence time

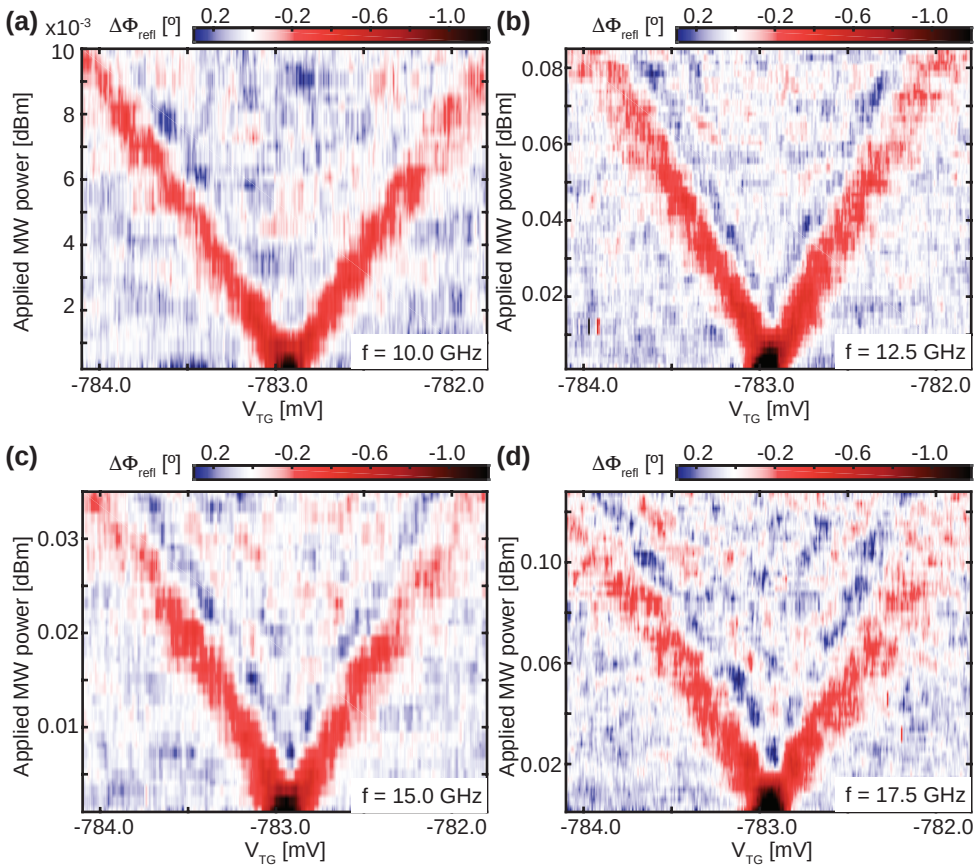

Figure 6.6: Frequency dependence of Landau-Zener-Stückelberg interferometry. The LZS interferometry patterns for four different microwave frequencies: **(a)** 10 GHz, **(b)** 12.5 GHz, **(c)** 15 GHz, and **(d)** 17.5 GHz.

around 60 ps for the acceptor-lead system, which is comparable to the coherence time found for quantum dots in a similar transistor.[168] A possible dephasing mechanism comes from charge noise in the system. This has been identified as a likely source of decoherence in other systems consisting of a single charge in a double quantum dot, such as GaAs quantum dots,[170] donors in silicon,[167] and quantum dots in carbon nanotubes,[171] for which phase coherence times in the 100 ps range have been measured. An estimate of the charge noise that could lead to this decoherence time is given by $\sqrt{2}h/T_2^* \sim 0.1$ meV.

6.4 Photon-assisted tunneling in transport spectroscopy

In addition to the rf gate reflectometry measurements, the effect of microwaves on dc transport measurements was studied. A tri-gate transistor with a channel

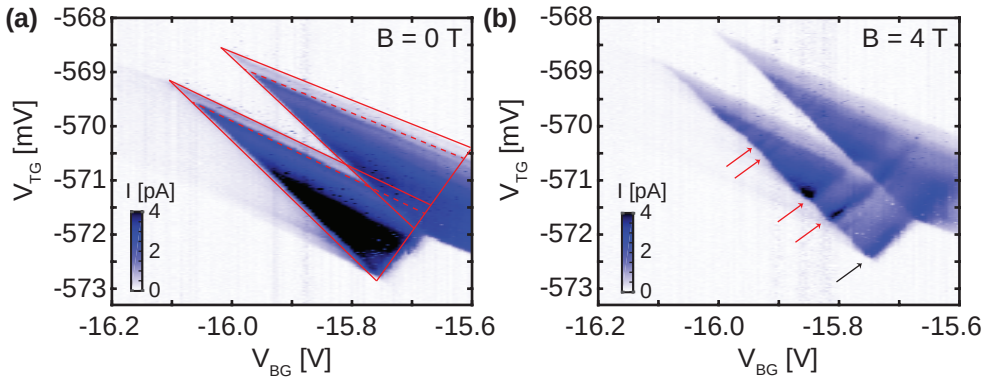

Figure 6.7: Double acceptor transport. **(a)** Current map as a function of the voltages applied to the top gate and back gate, with a 1.5 mV bias voltage applied. Bias triangles are indicated by red lines. An excited state is indicated by a dashed red line. **(b)** The same measurement in a magnetic field of 4 T, where excited state transitions (red arrows) are observed parallel to the baseline (black arrow).

width of 42 nm, a channel height of 11 nm, a gate length of 34 nm and a background boron concentration of 5×10^{17} cm^{-3} was investigated.

6.4.1 Single hole system of coupled acceptors

Bias triangles are observed in the dc transport measurement map, shown in Fig. 6.7a. It reveals a sequential tunneling through localized states as discussed in chapter 3. From the shape of the triangles, relative capacitive couplings to the top gate of α^1_{TG} 0.82 $\pm$ 0.02 and α^2_{TG} 0.60 $\pm$ 0.03 were found for the two localized states. Furthermore, the step in current parallel to one side of each triangle (marked with dashed lines in Fig. 6.7a), corresponds to a low-lying excited state. Because only one excited state is observed, this spectrum is attributed to a boron atom with a small light-heavy hole splitting. The Δ_{LH} extracted from the bias triangle is 140 $\pm$ 30 μeV.

To establish the origin of the second localized state in the transport process, the excited state spectrum was studied as a function of magnetic field. At a magnetic field of 4 T several excited state transitions appear as current oscillations parallel to the baseline of the bias triangle (indicated by arrows in Fig. 6.7b). The magnetic field dependence of the transition energies are found in a magneto-transport spectroscopy measurement presented in Fig. 6.8a. A total number of 6 excited state transitions are resolved, which is in agreement with a system consisting of two boron atoms, as outlined below.

The description of single acceptor atoms in silicon, introduced in chapter 2,

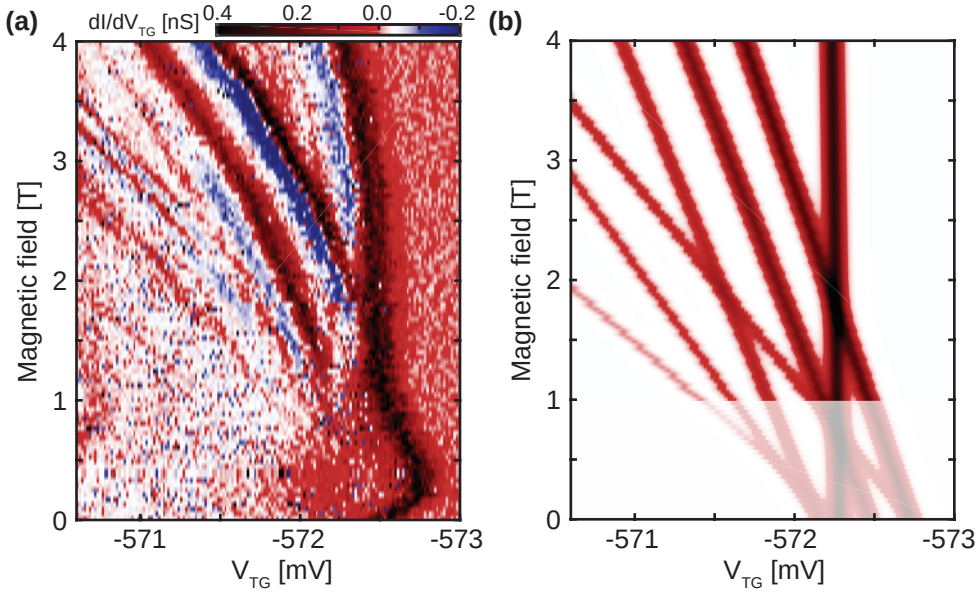

Figure 6.8: Magneto-transport spectroscopy. **(a)** Numerical transconductance (dI/dV_{TG}) as a function of magnetic field, showing the excited state transition spectrum within the bias triangle. **(b)** A simulation of the excited state transitions for a single hole on two coupled acceptors with different light-heavy hole splittings and different Landé g-factors.

was used to predict the excited state transitions of two holes bound to two acceptors in chapter 5. Here the single hole system is considered in the same manner. The four lowest states of a single hole bound to an acceptor are described by linear combinations of heavy and light hole states. For an applied magnetic field larger than the light-heavy hole splitting the ground state has a predominant heavy hole character for both acceptors. The transition between the ground states is expected to depend only weakly on the magnetic field, because of a possible difference in Landé g-factor. Transitions between the level of the first atom with a smaller Zeeman shift than the level of the second atom, will move inside the bias triangle. Under the assumption that the g-factor is similar for both atoms, six of these transitions are expected.

These six excited state transitions are modelled using different g-factors for the heavy and light hole states of both atoms and introducing a different light-heavy hole splitting for each atom, shown in Fig. 6.8b. In Fig. 6.8a the positions and slopes of the excited state lines, between 1 and 3 T, are used as an input for this model. Light-heavy hole splittings of 30 μeV and 110 μeV are found for the first and second acceptor respectively. The larger splitting is in agreement with the excited state found in the bias triangle at zero magnetic field. Effective g-factors ($g* = gm_j$) of 0.47 and 1.77 were found for the light

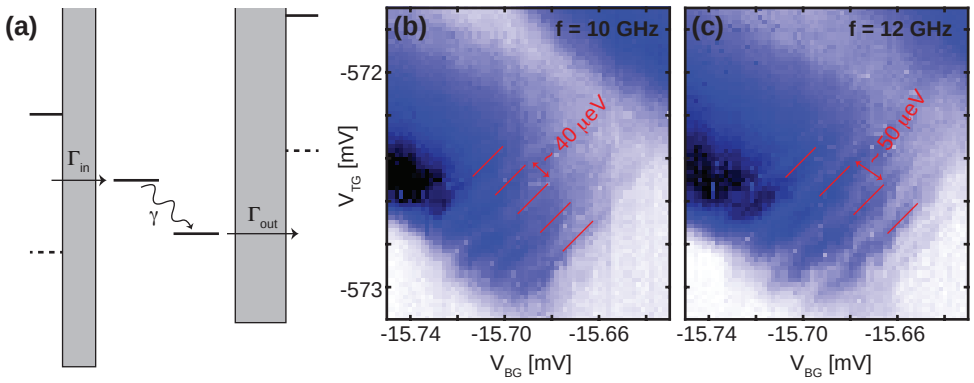

Figure 6.9: Photon assisted tunneling. **(a)** Schematic diagram of photon assisted tunneling, where the absorption of one photon allows for the tunneling between two atoms. **(b)** and **(c)** Photon assisted tunneling observed between the two coupled acceptors with an applied microwave power of -25 dBm and frequencies of 10 and 12 GHz respectively.

and heavy holes bound to the first acceptor and 0.72 and 1.72 for the second acceptor.

Furthermore, a deviation from the linear behavior is observed for fields above 3 T in Fig. 6.8a. Two different effects can explain this behavior. First, the quadratic Zeeman effect, neglected in the discussion presented in chapter 2, can be reconsidered as it could have an effect at the higher magnetic fields applied in this experiment. Secondly, a change in quantization axis of the total angular momentum of the hole can be the cause, as discussed for the two-hole system in chapter 5. It is interesting to note that the Zeeman energy of a state with an effective g-factor of 1 would be equal to the observed light-heavy hole splitting of 110 μeV around 2 T. This could be related to the deviation of the linear behavior observed at higher magnetic field.

6.4.2 Photon assisted tunneling

Signatures of photon assisted tunneling are found in the transport bias triangles measured by microwave spectroscopy. The tunneling process between the two acceptor atoms is assisted by the absorption of a photon, as shown in Fig. 6.9a. As shown in the case of Landau-Zener-Stückelberg oscillations, multi-photon processes can lead to the observation of an oscillating transport signal as a function of the detuning. In Fig. 6.9b and c these oscillations are shown for microwave frequencies of 10 and 12 GHz respectively. The different frequencies are expected to give a different energy spacing between the multi-photon processes. This effect was observed in this experiment and thereby confirms

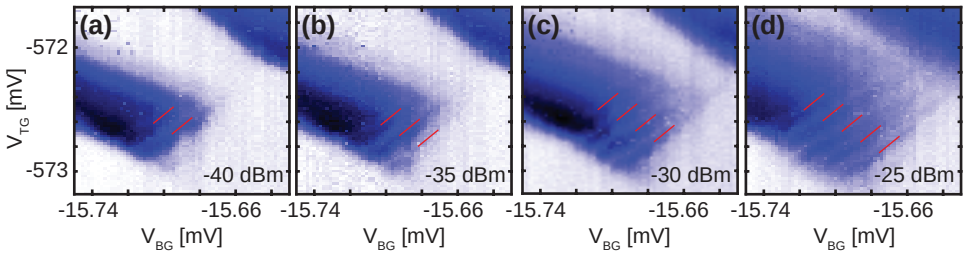

Figure 6.10: Power dependence of photon assisted tunneling. **(a)**, **(b)**, **(c)**, and **(d)** Four different microwave powers, from -40 to -25 dBm, are applied at a frequency of 10 GHz and an increasing number of photons are involved in the photon assisted tunneling as the microwave power increases.

the oscillations originate from photon-assisted tunneling.

The microwave power dependence of these oscillations is shown in Fig. 6.10. With increasing power, tunneling processes involving more photons become possible. At an applied power of -40 dBm only the 1 and 2 photon processes are observed, but at a 15 dBm higher power up to 5 photon processes are visible.

These photon assisted tunneling oscillations show that the two acceptor system can be manipulated with a microwave electric field applied by a local gate. The next step is to extend this microwave control to the coherent manipulation of single acceptor states in an electrically driven spin resonance experiment.

6.5 Conclusion

In this chapter the microwave spectroscopy of coupled boron atoms and a single boron atom coupled to an extension of a reservoir was analyzed. In these experiments, the microwaves were applied to gate electrodes, meaning that these gates are suitable to drive transitions between acceptor states as proposed for acceptor qubits. The resonant excitation between the bonding and anti-bonding state of a two-hole system enabled the direct measurement of the tunnel rate between two atoms, without prior knowledge about the g-factors or the gate couplings. Landau-Zener-Stückelberg interferometry in rf gate reflectometry measurements showed a coherence time around 60 ps for the charge transition between a single acceptor and the drain lead. Furthermore, photon assisted tunneling in transport measurements was used to probe the system of one hole bound to two acceptor atoms. All these microwave spectroscopy experiments provide the first steps towards realizing

an electrical coherent control over the spin states of a single acceptor atom.

chapter 7

Single-atom electron pump

Single-electron pumps based on isolated impurity atoms have recently been experimentally demonstrated. In these devices the Coulomb potential of an atom creates a localised electron state with a large charging energy and considerable orbital level spacings, enabling robust charge capturing processes. In these single-atom pumps, the confinement potential is hardly affected by the periodic driving of the system. This is in contrast to the often used gate-defined quantum dot pumps, for which a harmonic and strongly time-dependent potential leads to significantly different charge pumping processes. Here we describe the behavior and the performance of an atomic, single parameter electron pump. This is done by considering the loading, isolating and unloading of one electron at the time, on a phosphorous atom embedded in a silicon double gate transistor. The most important feature of the atom pump is its very isolated ground state, which can be populated through the fast loading of much higher lying excited states and a subsequent fast relaxation process. This leads to a substantial increase in pumping accuracy, and is opposed to the adverse role of excited states as observed for quantum dot pumps due to non-adiabatic excitations. The pumping performances are investigated as a function of dopant position, revealing a pumping behavior robust against the expected variability in atomic position.

Part of this chapter is published online as:

- J. van der Heijden, G.C. Tettamanzi and S. Rogge, *Dynamics of a single-atom electron pump*, arXiv:1607.08696.

7.1 Introduction

Quantized charge pumps can be used as single electron sources,[172–177] which have potential applications in electron quantum optics[178,179] and can be used as a new standard for the Ampere in quantum metrology[180,181] when they can be operated with a sufficiently high accuracy.[175,176,182–184] Essential to semiconductor electron pumps is to control the energy states of a quantum dot,[175,176,184,185] an impurity atom,[177,186,187] or both,[188,189] in order to capture, isolate, and emit a fixed number of electrons in every cycle of the electron pump. The most common charge pumps are based on quantum dots where the shape of the dot strongly depends on the ac driving voltage of the pump. Due to the drastic reshaping of the confinement potential for the electron during the pumping cycle, this type of charge pump is named the dynamical quantum dot pump. This dynamic behavior of the electron confinement is in sharp contrast with electron pumps based on single dopant atoms, where the electron confinement originates from the fixed 1/r Coulomb potential of the atom. This leads to a significantly different pumping process and requires a new model to accurately describe the single-atom charge pumps.

Recent improvements in electron confinement,[176,190] pulse shapes,[175] and readout techniques,[191,192] have led to highly accurate single-electron pumps based on dynamical quantum dots. The pumping process of these pumps has been studied extensively[193] and is accurately described by the universal cascade decay model.[194] The best performing pumps have achieved an uncertainty below 0.2 ppm at a driving frequency around 500 MHz.[184] Here back-tunneling processes, where the electron tunnels back to its source, are found to be the main source of systematic errors at these high pumping frequencies.[192,194] At even higher frequencies non-adiabatic excitations[195,196] start to play a detrimental role, as the fast ac driving voltage produces unwanted excitations in the quantum dot, which can substantially increase the back-tunneling rate and thereby decrease the accuracy of the electron pump.

Dopant atom electron pumps, using the fixed atomic potential as confinement, have the potential to lower these systematic errors. The Coulomb potential of a donor atom provides a highly localized electronic state, which isolates the electron during the pumping process and thereby reduces the chances of back-tunneling. Furthermore, the large energy spacing between the ground and excited states of an atom lowers the chance of non-adiabatic excitations. However, as an inevitable consequence of the fixed atomic confinement and isolated electronic state, the loading of the electron on the atom becomes a

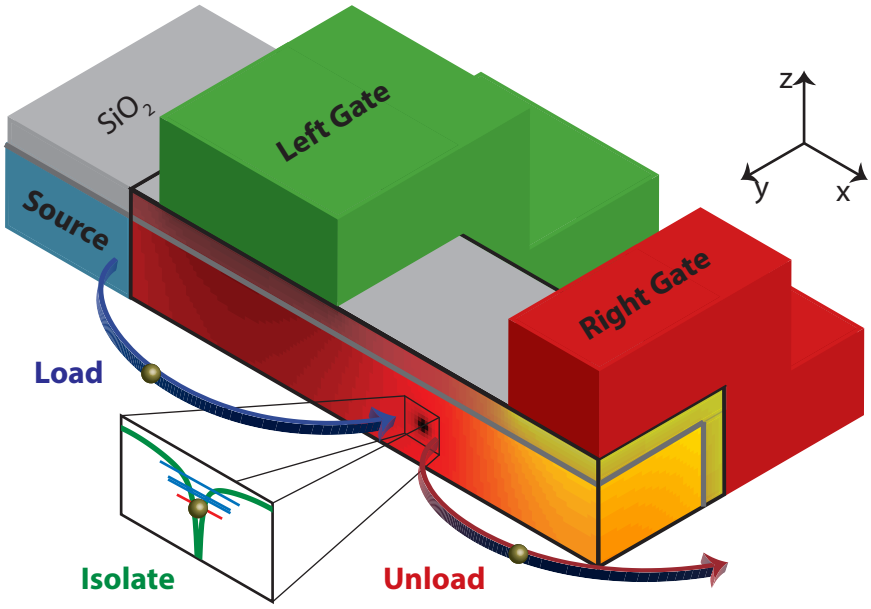

Figure 7.1: Single-atom electron pump. Schematics showing the electronic potential in a 3-D cut through the transistor, cut in half in the y-direction, and through the middle of the right gate in the x direction. The three crucial stages of the electron pump are indicated: the loading, isolating and unloading stage.

possible source of error. This sharply contrasts the behavior of dynamical quantum dots, where the accurate description based on the universal decay cascade model ascribes the pumping error to the ratio between the back-tunneling probabilities of N and N+1 electrons, leaving out any loading and unloading errors.[194]

To accurately describe the behavior of a single-atom electron pump (as schematically shown in Fig. 7.1), we present a model that takes into account the loading, back-tunneling and unloading processes as the three main stages of the pumping cycle, and capture all possible sources of systematic errors. It is found that the most accurate charge pumping is achieved only when multiple energy states of the atom contribute to the loading stage of the pump cycle. In this scenario the tunnel rate from the leads to the ground state of the atom is insufficient to load an electron. Instead an electron tunnels from the source to one of the excited states of the atom with greater efficiency, because of the higher tunnel rates associated with the spatially more extended excited states. After this initial step, the electron relaxes to the ground state, where, due to the slow tunnel rate between the ground state and the source, back-tunneling

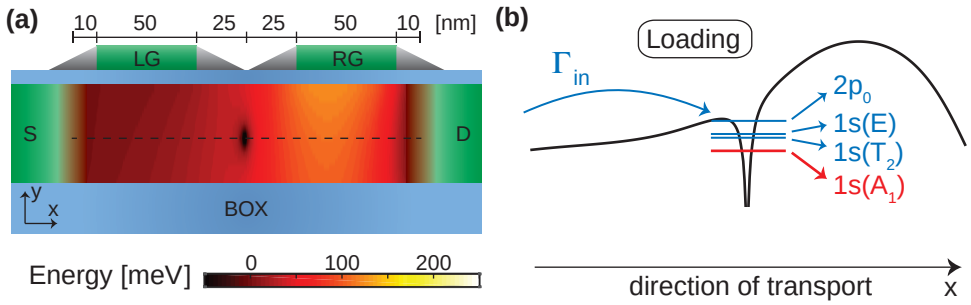

Figure 7.2: The loading stage. **(a)** Calculation of the potential profile in a cut through the middle, i.e. in the direction of the width, of the double gate transistor as used in this chapter, where one dopant atom is placed in the centre of the transistor channel with dimensions 170-50-20 nm (length-width-height). The voltages used to create this profile identify the loading stage in the pumping cycle. **(b)** A plot of the profile in the x (length) direction indicated with a dashed line is shown, indicating the tunnel-in rate which is relevant for the loading stage.

is substantially suppressed. This beneficial effect of the excited states for the single-atom pump clearly opposes their adverse role for dynamical quantum dot pumps.

An incomplete relaxation from the atomic excited states to the ground state is found to be the main source of error in the pumping process via atoms. This is further investigated by studying the influence of the pumping frequency and relaxation rates on the pumping accuracy. The last part of this work focuses on the influence of the donor position in this scheme and shows that the behavior of the single-atom electron pump is robust for displacements of the donor over a distance of 30 nm.

7.2 Single-atom electron pump model

In the following section a complete description of the single-atom electron pump model is given, by outlining the geometry of the pump, specifying the used postulates and providing the theoretical framework.

7.2.1 Device description

The model is directly compared to experiments on a single-atom electron pump. The specific geometry of this device, which has recently demonstrated single electron pumping[177] is used to calculate the tunnel rates, involved in pumping the electrons one-by-one through the transistor, for our model. As shown in

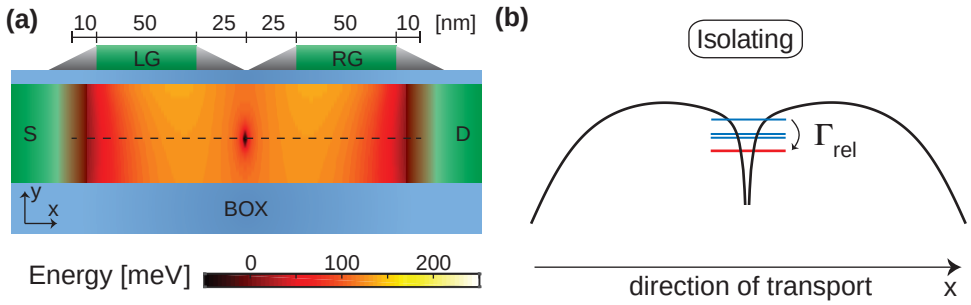

Figure 7.3: The isolating stage. **(a)** Calculation of the potential profile similar to Fig. 7.2. The voltages used to create this profile identify the isolating stage in the pumping cycle. **(b)** A plot of the profile in the x (length) direction indicated with a dashed line is shown, indicating one of the relaxation rates, which are critical in the isolating stage.

Figs. 7.2 to 7.4, both the left gate (LG) and right gate (RG) are 50 nm long and are separated by 50 nm. The source and drain are separated from the gates by silicon nitride spacers to get to a total channel length of 200 nm, however some diffusion of the source and drain dopants under the spacers is taken into account, which reduces the effective length to 170 nm. In our model, the width and height of the channel are taken to be 50 and 20 nm respectively and the dopant potential is initially placed in the centre of the transistor channel in all directions, i.e. length, width and height. The effect of changing the position of this potential along the length direction is discussed in the last section. For the experiments, the single-atom electron pump is mounted on a cold finger and measured at 4.2 K. A low noise battery operated measurement setup was used to measure the source/drain current and to apply dc voltages to the gates. Typical measurements were acquired at $V_{SD} \sim 0$ mV and by applying a sinusoidal rf input to the left gate via the bias-tee in a typical single parameter configuration.[177,193]

7.2.2 Model postulates

The energy spectrum of the phosphorous atom is, in our model, always assumed to be equal to the known bulk values[197] and fixed throughout the pumping cycle. Especially at a distance of 10 nm from the Si/SiO_2 interface (i.e. middle in the height direction, see black dashed lines in Figs. 7.2 to 7.4), this assumption is justified, as the excited state energies and charging energy are expected to approach the bulk values,[198,199] which has been experimentally confirmed.[41,200] Furthermore, we find a maximum electric field during the

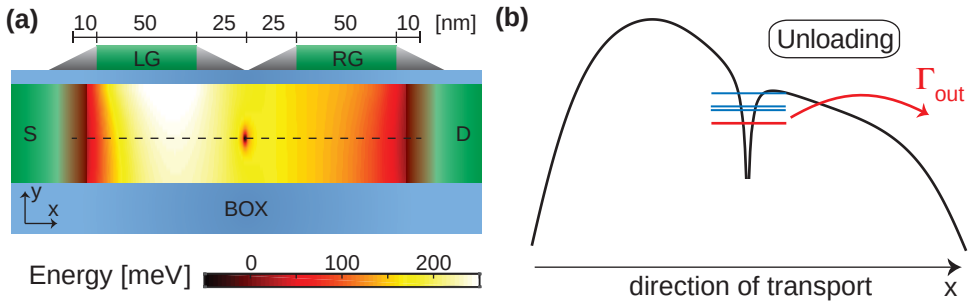

Figure 7.4: The unloading stage. **(a)** Calculation of the potential profile similar to Fig. 7.2 and 7.3. The voltages used to create this profile identify the unloading stage in the pumping cycle. **(b)** A plot of the profile in the x (length) direction indicated with a dashed line is shown, indicating the tunnel-out rate which is relevant for the unloading stage.

unloading stage of the pumping cycle of 4 MV/m, where in the more important loading stage the field never exceeds 3.5 MV/m. For these electric fields it has been shown that the excited state spectrum of a donor atom does not greatly change[57] and also the charging energy of the atom is stable.[121] The singlet $1s(A_1)$ state with a binding energy of 45.6 meV is used as the ground state in our model together with the lowest three excited states, being the valley-orbit triplet $1s(T_2)$ and doublet $1s(E)$ states separated by 11.7 and 13 meV from the ground state respectively and the $2p_0$ state separated by 34.1 meV. The binding energy of the second electron is taken to be 2 meV.[120]

Contrary to the decay cascade model, our model considers only the tunneling via the first electron state, i.e. the D^0 state, which restricts the voltages applied to the gates to values for which the energy level of a second donor-bound electron stays above the source and drain Fermi energy during the entire pump-cycle. The doubly occupied, negatively charged donor state is referred to as D^-. Although this restriction in gate voltage space denies the modelling of the pumping current regions that are related to more than one electron and likely does not include the complete voltage space where one electron is pumped, it still allows the capturing of the unique physics of a single-atom pump. This because the large charging energy of the donor atom allows the capturing of the first electron at a much lower energy and therefore much lower voltages than the second electron. Lastly, for single-impurity charge pumps, and in agreement with our theoretical approach, only the 1 electron plateau can be effectively used to estimate the accuracy of the pump.[188]

7.2.3 Theoretical framework

The model presented here is based on three consecutive calculation steps. First the potential profile in the channel is calculated by solving the Poisson equation, see Figs. 7.2 to 7.4. Second, this potential profile is used to estimate the tunnel rates between the different energy levels of the donor atom and the source and drain leads, see Fig. 7.5b, by using the Wentzel-Kramers-Brillouin (WKB) method, as in Eq. 7.1. And third, these tunnel rates are used in a rate-equation model, as in Eq. 7.2 to Eq. 7.4, to find the occupation probabilities of all the states during the pumping cycle, see Fig. 7.5c, which consequently gives the average amount of electrons transferred per cycle, as in Eq. 7.5.

The Poisson equation is solved by using the finite difference method for different combinations of voltages on the left and right gate, while keeping the source and drain leads grounded, consistent with the experimental situation. This solution gives the three-dimensional potential landscape in the transistor for each set of gate voltages, see Fig. 7.1. Subsequently the tunnel rates between the energy levels of the atom and the source and drain leads are calculated with the use of the one dimensional WKB method:

$$\Gamma_i(t) = \xi\Gamma_0 \int_0^{x_{dop}} e^{-2x\sqrt{U(x,t)-E_i(t)}\sqrt{\frac{2m^*}{\hbar^2}}}\, dx, \tag{7.1}$$

where $\Gamma_i(t)$ is the tunnel rate to or from energy state i at time t of the pumping cycle, $U(x,t)$ is the potential in the transistor at position x, as defined in Figs. 7.2 to 7.4 , and at time t. E_i is the energy of the considered donor state and m^* is the effective mass in silicon. The integral is taken from the end of either the source or drain lead, denoted by position 0, to the position of the dopant x_{dop}. Furthermore, ξ denotes the degeneracy of the state and Γ_0 is the attempt frequency, which symbolises the maximum tunnel rate in this system. An estimation of the attempt frequency for the donor is made by imagining an electron bouncing back and forth between two walls and counting the frequency with which it hits one of these walls. To get an estimation of the 'speed' we use the binding energy as a kinetic energy and the Bohr radius is used as the distance between the walls. This leads to a Γ_0 of $2E_b/\hbar$, which is close to 100 THz for the phosphorus ground state.

The behavior of the single-atom electron pump is described by the occupation probabilities of all the atomic states during the pump cycle. The estimated tunnel rates are used in a rate equation model to calculate the occupation probabilities of all the atomic energy states. The occupation probabilities are represented by the vector $P(t) = \begin{bmatrix} P_u(t) & P_0(t) & P_1(t) & P_2(t) & P_3(t) \end{bmatrix}$,

consisting of the probability for the atom to be unoccupied followed by the probabilities of one electron to be in the $1s(A_1)$, $1s(T_2)$, $1s(E)$, and $2p_0$ states at time t. The occupation probabilities during the pumping cycle are found by solving the following set of equations:

$$\sum_{i=u,0..4} P_i(t) = 1, \tag{7.2}$$

$$dP/dt = M(t) \times P(t), \tag{7.3}$$

$$M = \begin{pmatrix} -\sum\limits_{n=0..3} \Gamma_n^i & \Gamma_0^o & \Gamma_1^o & \Gamma_2^o & \Gamma_3^o \\ \Gamma_0^i & -\Gamma_0^o & \Gamma_1^r & \Gamma_2^r & \Gamma_3^r \\ \Gamma_1^i & 0 & -\Gamma_1^o - \Gamma_1^r & 0 & 0 \\ \Gamma_2^i & 0 & 0 & -\Gamma_2^o - \Gamma_2^r & 0 \\ \Gamma_3^i & 0 & 0 & 0 & -\Gamma_3^o - \Gamma_3^r \end{pmatrix}, \tag{7.4}$$

where Γ_n^i is the in-tunnel rate (i.e. from the source or drain to the atom state n), Γ_n^o the out-tunnel rate (i.e. from the atom state n to the source and drain) and Γ_m^r the relaxation rate of the donor excited state m to the $1s(A_1)$ ground state. The tunnel rates, as calculated by Eq. 7.1 with taking spin and valley degeneracies into account for the tunnel-in rates, are regarded as Γ^i if the energy of the donor state is below the Fermi level of the source and drain and Γ^o otherwise. For the source and drain contacts a Fermi-Dirac distribution of electrons at a temperature of 4.2 Kelvin is assumed. The rate equation is numerically solved using the explicit Runge-Kutta Dormand-Prince method.

The relaxation rates from the excited states to the ground state play an important role for the single-atom electron pump. Estimations of the relaxation rates from the $1s(T_2)$, $1s(E)$ states to the $1s(A_1)$ state are found in the 1 to 100 GHz range.[201–203] Relaxation from the $2p_0$ state is expected to follow a double relaxation process, where it first relaxes to either the $1s(T_2)$ or the $1s(E)$ state,[201,202] with an estimated relaxation rate of several tens of GHz.[204] The total relaxation rate from the $2p_0$ state is measured around 5 GHz.[205] To incorporate these findings in our model, only direct relaxations to the $1s(A_1)$ are included (see Eq. 7.4), where the relaxation rates are set to 10 GHz for all three excited states. As the pumping accuracy depends strongly on the assumed relaxation rates, the effect of a change in the relaxation rates is investigated later in the paper.

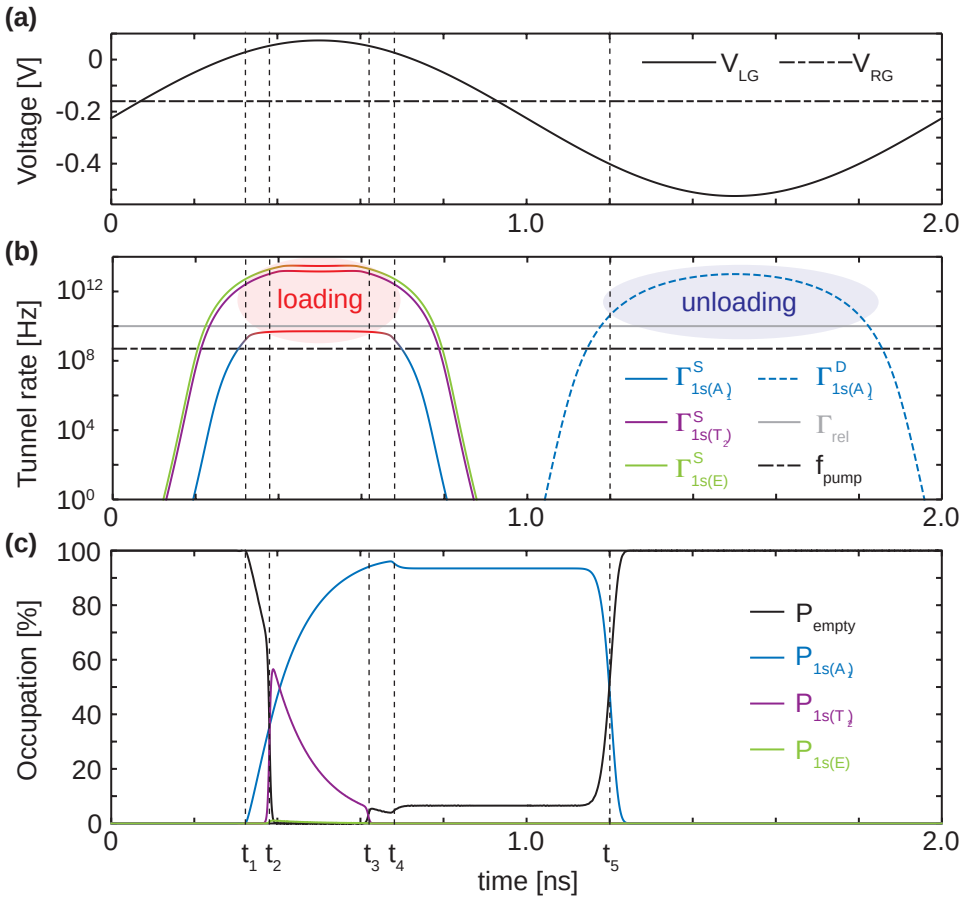

Figure 7.5: Typical pumping cycle. **(a)** Time dependence of voltages V_{LG} and V_{RG} during the cycle. **(b)** The relevant tunnel rates from the source (solid lines) and to the drain (dashed line) during the pumping cycle for the $1s(A_1)$ state (blue), the $1s(T_2)$ state (purple) and the $1s(E)$ state (green). When a state is below the Fermi level of the source, the line is colored red. A grey line shows the relaxation rates for the $1s(T_2)$ and $1s(E)$ states to the $1s(A_1)$ state and a black dashed-dotted line shows the pumping frequency. **(c)** The corresponding occupation probabilities for the relevant single electron states of the atom as a function of time, where five moments in the cycle are highlighted with t_1 to t_5, as discussed in the text.

7.3 Typical pump cycle

Next, the operation of the single-atom electron pump will be discussed by examining the time dependent voltages, tunnel rates and occupation probabilities during a typical pump cycle (as displayed in Fig. 7.5). This cycle is simulated with V_{RG} = -165 mV and V_{LG} = -220 mV, while a 300 mV ac voltage is added to the left gate, see Fig. 7.5a. Note that these are not the optimal conditions for the pump (on average, only 0.9 electrons are pumped per cycle), but it shows a pumping cycle where both the benefits of excited states are visible and possible error mechanisms are displayed. The phase of the driving voltage is chosen such that the cycle starts between the unloading stage (low V_{LG}) and loading stage (high V_{LG}), where the initial condition is chosen as $P_u(0) = 1$ and $P_{0..3}(0) = 0$. As this initial condition only holds if the unloading stage is complete, it is iteratively updated when the final state differs from the initial state.

In Fig. 7.5 the critical moments in the pump cycle of the single-atom electron pump are denoted with t_i, where i ranges from 1 to 5, and the dashed lines show the corresponding tunnel rates (Fig. 7.5b) and occupation probabilities (Fig. 7.5c). The loading stage starts at times t_1 and t_2, where the $1s(A_1)$ state starts to slowly load at t_1 and the $1s(T_2)$ quickly loads at t_2. At t_2 the $1s(E)$ state barely contributes to the loading process, as shown in Fig. 7.5c, which is due to the fact that the $1s(T_2)$ crosses the Fermi energy a short moment before the $1s(E)$ state and fills almost completely within that time, due to the high tunnel-in rate. The back-tunneling processes from the atomic states start at t_3 ($1s(T_2)$) and t_4 ($1s(A_1)$). The back-tunneling error from the $1s(A_1)$ ground state can only be reduced by lowering the tunnel rate from this state to the source. In contrast, the back-tunneling error from the ($1s(T_2)$) can be reduced by either a faster relaxation rate to the ground state, or a longer time ($|t_3 - t_2|$) to relax to the ground state. After t_4 the loading of electrons to the atomic ground state is finished and all other excited states are empty. Importantly, this model indicates that for a single-atom quantum electron pump, a large part of the occupation of the ground state originates from a loading process to the $1s(T_2)$ excited state and a subsequent relaxation, which is a completely different loading mechanism than the loading process of dynamical quantum dot electron pumps, for which this occupation happens mainly via a directly filling of the ground state. Finally, at t_5 the unloading of the electron from the ground state to the drain occurs.

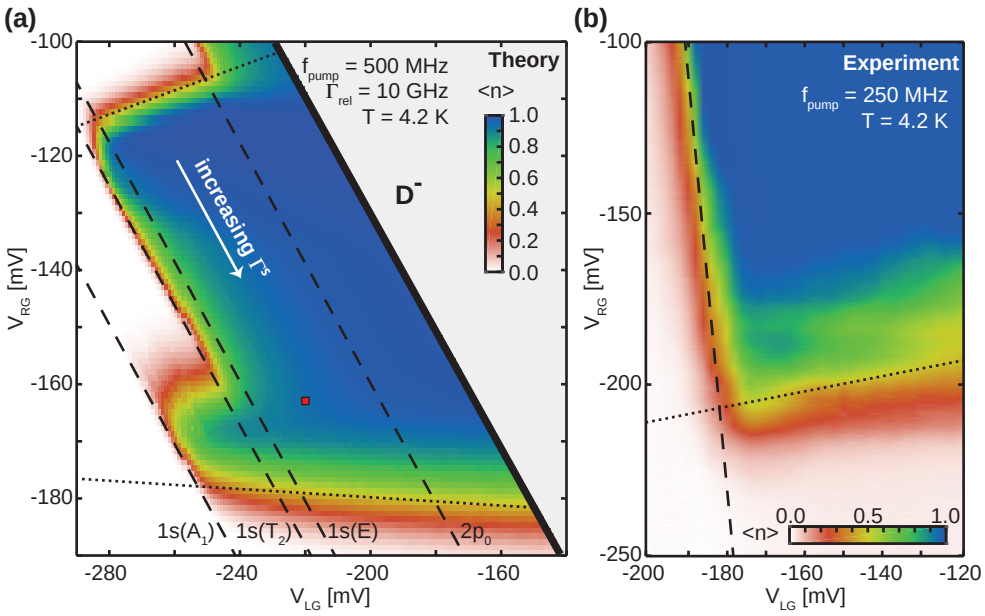

Figure 7.6: Comparison between theory and experiment in average number of pumped electrons. **(a)** Number of pumped electrons, $\langle n \rangle$, as a function of the dc voltages V_{LG} and V_{RG}, using an ac sinusoidal driving voltage on V_{LG} with a 300 mV amplitude and a 500 MHz frequency in the calculations. The red square corresponds to the pumping cycle as shown in Fig. 7.5. The solid, dashed and dotted lines indicate the boundaries of the pumping plateau, as discussed in the main text. **(b)** The model is compared with experimental data from a single-atom electron pump, which is operated with a 250 MHz and ∼100 mV driving signal. The left and bottom boundaries found in the model are also found in the experiment.

7.4 Comparison between the model and experiment

The total probability of pumping a single electron from the source to the drain, denoted as $\langle n \rangle$, can be estimated by only accounting for the electrons that go to and come from the drain (or source) in Eq. 7.3, which gives:

$$d\langle n \rangle / dt = \sum_{n=0..3} \Gamma_n^{o,d}(t) P_n(t) - \sum_{n=0..3} \Gamma_n^{i,d}(t) P_u(t) \tag{7.5}$$

Here $\Gamma_n^{o,d}$ and $\Gamma_n^{i,d}$ are the tunnel rates to and from the drain lead. In the visualisation of the data in Fig. 7.6 the average number of electrons pumped per cycle $<n>$, defined as $\frac{I_{SD}}{ef}$, is shown. Fig. 7.6a shows the average number of electrons per cycle as a function of the dc voltages on the left and right gates when a 500 MHz sinusoidal ac voltage with 300 mV in amplitude is added to the left gate, i.e. in a single parameter charge pumping configuration.

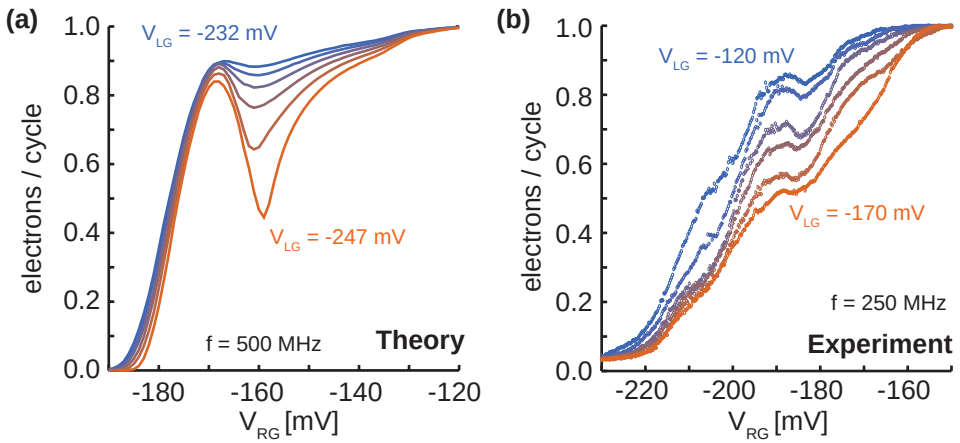

Figure 7.7: Comparison between theory and experiment of excited state effects. **(a)** Six line-plots, taken from Fig.7.6a at V_{LG} (-247, -244, -241, -238, -235, -232) show a stepwise increase of pumped electrons in the model, as a result of the involvement of the excited states in the loading process. **(b)** This is compared to line-plots taken from Fig.7.6b for voltages V_{LG} (-120, -130, -140, -150,- 160, -170). In this experiment similar steps of the pumping current as found by the model are observed as a function of V_{RG}.

A plateau of current close to the ideal 1 electron per cycle is found, which is in agreement with experiments.[177] The solid black line in Fig. 7.6a shows the boundary of the model where the D^- state equals the source and drain Fermi level at the lowest potential in the pump cycle. The crossings of the one electron ground and excited states with the Fermi level are also shown in Fig. 7.6a (dashed lines). A clear increase in pumping accuracy is observed when the loading of the electron into the ground state is possible via an intermediate excited state with subsequent relaxation. This underlines the important role of the excited states in the accuracy of the single-atom pump.

The model is compared to the experiment on a single-atom electron pump, which is operated with a driving signal of a 250 MHz frequency and around a 100 mV amplitude, see Fig. 7.6b. The bottom and left boundary indicated by the model are also found in the experimental data, where both the direction and broadening of these boundaries show strong similarities. The increase in pumping current caused by the improved loading of the ground state via the excited states appears as several steps in the model when line cuts are taken at different values of V_{LG} as shown in Fig. 7.7a. These line cuts are compared with line cuts in the experimental data of Fig. 7.6b, as shown in Fig. 7.7b. The similarities between the experiment and theory in the steplike increase of the pumping current towards the plateau of 1 electron per cycle,

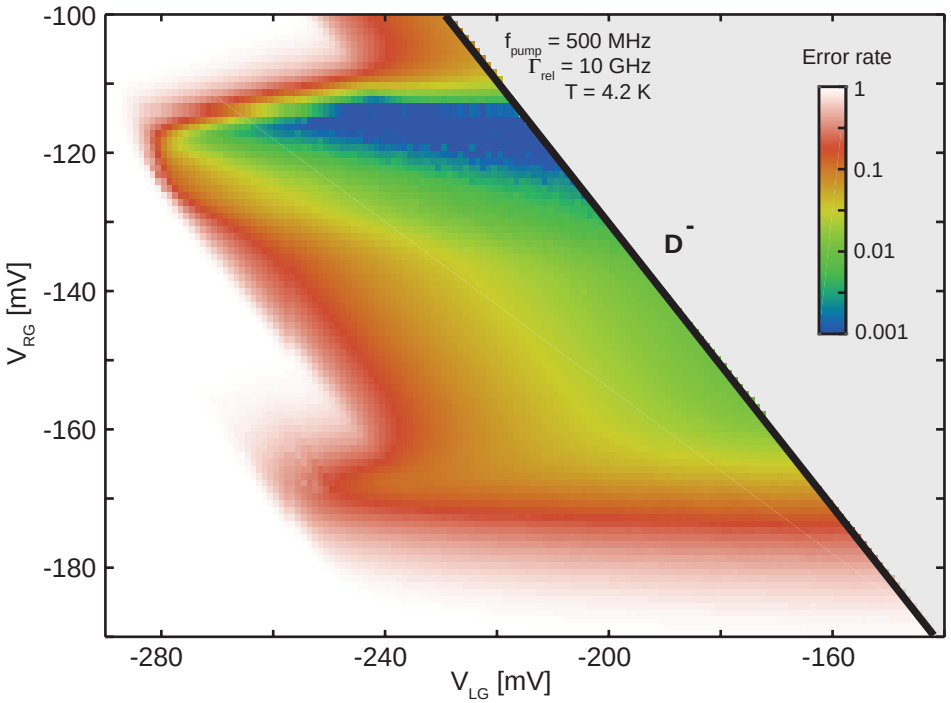

Figure 7.8: Accuracy of a single-atom electron pump. The same result as in Fig. 7.6a, but now shown as the number of electrons per cycle less than the ideal 1 electron per cycle on a logarithmic scale.

both in line shape and dc voltages, demonstrates the good agreement between the model and the experiment. Furthermore, these similarities confirm the strong positive influence of the excited states of the atom on the behavior of this pump geometry as seen in the experiment. Indeed, for single-atom pumps the excited states play a crucial role to establish an effective pumping cycle, greatly contrasting the adverse role of excited states for dynamical quantum dot pumps through non-adiabatic excitations.

7.5 Discussion of the pumping accuracy

The operational region of the single-atom electron pump has, next to the boundaries caused by the crossing of the Fermi energy (dashed and solid lines in Fig. 7.6a), two boundaries caused by the limits on the tunnel rate between the atom and the source (dotted lines in Fig. 7.6a), as also discussed elsewhere.[177] This tunnel rate increases in the direction of a more negative V_{RG}, with a small dependence on V_{LG}, see Fig. 7.6a. First, the boundary found at the bottom of Fig. 7.6a, around a -180 mV voltage on the right gate and

almost independent of V_{LG} is discussed, where the exact gate dependencies depend strongly on the position of the atom. At this boundary the tunnel rate from the $1s(A_1)$ ground state to the source is too fast at the moment this state crosses the Fermi level, leading to electrons tunneling back to the source as marked with time t_4 in Fig. 7.5. This is the same limit as considered in the decay cascade model.[194] At the other side of the plateau a boundary is found for V_{RG} around -110 mV, which has a small dependence on V_{LG}. At this boundary the loading stage of the atom is incomplete, caused by insufficient tunnel rates to the $1s(T_2)$ and $1s(E)$ to get to the full occupation of the atom within the time these states are below the Fermi level of the source. As the time of the pump-cycle that these states spend below the Fermi level depends on V_{LG}, this boundary has a dependence on the left gate voltage as well as the right gate voltage. A similar boundary can be seen for the $1s(A_1)$ ground state around -160 mV V_{RG} and will be present for the $2p_0$ state at a higher V_{RG}. In the centre of the single electron plateau, far away from every boundary and as visible in Fig. 7.5, the accuracy of the pump is limited by the ratio between the pumping frequency and relaxation rates from the excited states. Here the main systemic error comes from the back-tunneling of electrons from the excited states (shown at t_3 in Fig. 7.5). The occupation probability of the excited states, at the moment these states cross the Fermi level at t_3, strongly depends on how fast the electron relaxes to the ground state and the time this state spends below the Fermi level ($|t_3 - t_2|$), which depends on the pumping frequency.

In Fig. 7.8 the theoretical error rate of the single-atom electron pump is shown, defined as the difference with 1 electron per cycle, which illustrates the current quantisation properties of the electron pump in terms of accuracy. The exact behavior of the pump's theoretical error as a function of the dc voltages on the left and right gate is shown in Fig. 7.8. To investigate the effect of the ratio between the relaxation rate and pumping frequency, a simulation with the same pumping frequency of 500 MHz, but twice as fast relaxation times (20 GHz) is compared to a simulation with the same relaxation time (10 GHz), but at half the pumping frequency (250 MHz). Both give the same result for the accuracy in the centre of the plateau (shown in Fig. 7.9), which are two orders of magnitude more accurate than the original pumping cycle. Alternatively, to slow down the pumping frequency in the crucial loading stage, but still get a decent current output by ramping up the frequency in the unloading stage, several other waveforms have been proposed.[175,184,188] We compare our initial model to the accuracy of a model that has an effective

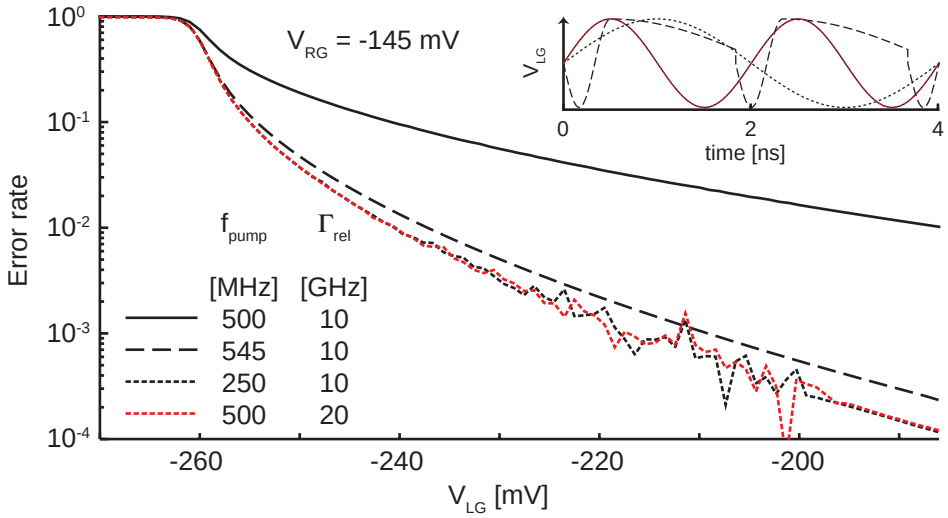

Figure 7.9: Influence of relaxation rates on the accuracy. A line-cut in Fig. 7.8 at -145 mV V_{RG} (solid line), compared with a pump cycle with half the pumping frequency (black dotted line). The same improvement in accuracy is found when the relaxation rates are doubled (red dotted line). Furthermore, a more effective pump cycle that uses more time in the loading stage and less in the unloading stage, is investigated (dashed line). The inset shows the voltages during the different cycles.

frequency of 150 MHz in the loading stage and 1.5 GHz in the unloading stage to get a total frequency around 545 MHz (dashed line in Fig. 7.9). This model shows an improvement of almost 2 orders of magnitude on the original model, while keeping the pumping frequency and relaxation rate constant, explained by the increased time the excited states stay under the Fermi level of the source.[175,184] These findings emphasize that the relaxation from excited states to the ground state of the atom is a parameter of major importance for the accuracy of the single-atom electron pump. The understanding of the possible relaxation paths between these valley-orbit excited states and available methods to increase these relaxation rates are essential to improve the accuracy of the single-impurity electron pumps, which have already shown pumping currents at frequencies of a few GHz.[177,188]

7.6 Influence of the atom placement

Finally, to study the feasibility of the single-atom electron pump, we have benchmarked the robustness of this pump as a function of the position of the atom. In Fig. 7.10 the pumping behavior with the atom in the centre (7.10b)

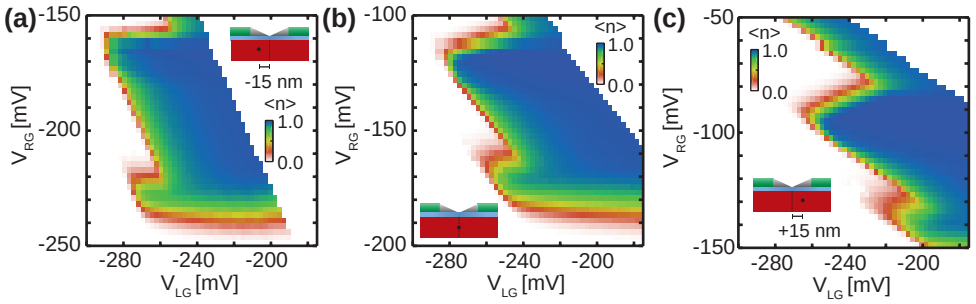

Figure 7.10: Comparison of three different dopant positions. **(a)** The phosphorous donor is displaced 15 nm towards the left gate from the centre, **(b)** the donor is in the centre and **(c)** the donor is displaced 15 nm towards the right gate from the centre. All simulations use a sinusoidal ac voltage on the left gate of 300 mV and 1 GHz and 20 GHz relaxation rates are assumed for all excited states, in order to keep the ratio between the pumping frequency and relaxation time equal to those in Figs.7.6a and 7.8, while reaching a faster computational speed. Furthermore, a lower resolution than in Figs. 7.6a and 7.8 is used, to reduce the total computation time. The same color scale as in Fig. 7.6a is used.

and moved 15 nm towards both the left (7.10a) and right (7.10c) gate are calculated, using a pumping frequency of 1 GHz and relaxation rates of 20 GHz. This is a fair comparison with the previous calculations, as this configuration keeps the same ratio between pumping frequency and relaxation rates. As it was shown in the previous sections, this ratio determines the maximum accuracy of the pump and we only expect slight changes to the boundaries of the pumping plateaus as an effect of the higher frequencies. Due to the change in capacitive coupling from the atom to the left and right gates, the slopes of the boundaries of the pumping plateau change with the change of atom position. Using this observation, the difference between the shape of the plateaus found in the theoretical model and the experimental data (as shown in Fig. 7.6), is explained by an atom located away from the centre closer to the left gate in the experiment. The overall pumping behavior is constant for displacements of 15 nm both towards the left and right gate, resulting in a robust single-atom electron pump over a distance of 30 nm (see Fig. 7.11). This is a crucial observation for establishing a reproducible charge pump geometry. The current single atom ion implantation techniques have an accuracy around 15 nm,[206] which could enable a controllable fabrication of accurate single-atom electron pumps. From Fig. 7.11 it is also concluded that moving the atom further to the right gate significantly improves the accuracy of the single-atom electron pump. The improvement in accuracy is a consequence of the weaker

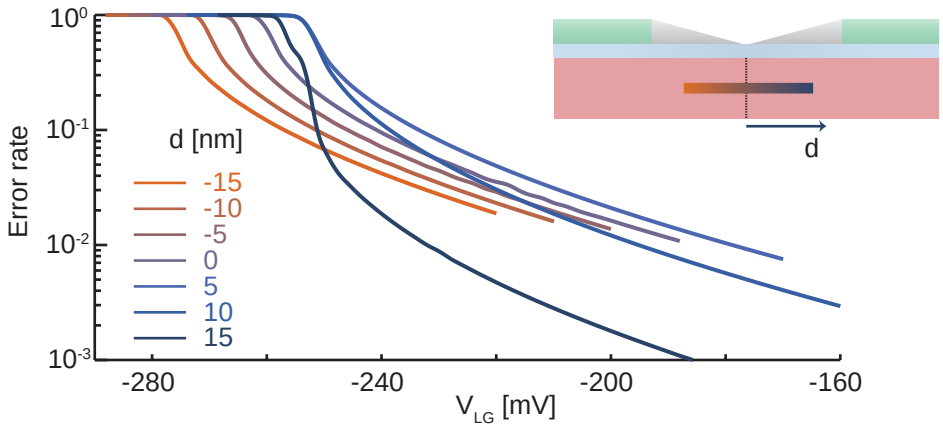

Figure 7.11: Influence of dopant placement on accuracy. The pumping accuracy as a function of V_{LG} for different donor positions, where the traces are taken at $V_{RG} = (-145 + \gamma d)$ mV to compensate for the shift of the plateau. Here d is the position relative to the centre of the transistor and γ is 3 mV/nm.

coupling of the atom to the left gate, which as a result keeps the atomic states longer below the Fermi energy ($|t_3 - t_2|$ is increased) and therefore has the same effect as a decrease in pumping frequency. However, this high accuracy region is less robust to displacements of the atomic potential.

7.7 Prospects of single-atom pumps

The implementation of single-atom pumps could, in certain circumstances, proof to be beneficial over the implementation of conventional dynamical quantum dot pumps, due to the fundamental different physical mechanisms behind the operation of these two types of single-electron pumps. As the accuracy of dynamical quantum dot pumps is related to the ratio between the back-tunneling rates of the N and N+1 electron states, the charging energy of these dots becomes of great importance. Increases in confinement by a stronger gate-control and high magnetic fields have led to larger charging energies and thereby more accurate pumps.[176,190] Recent experiments have shown that dynamical quantum dot pumps have reached an accuracy which is sufficient for applications in quantum metrology.[184] However, when operated at high frequencies, the rapid deforming of the quantum dot could lead to non-adiabatic excitations which degrade the accuracy of the pump.[195,196] The confinement potential in single-atom pumps is expected to be more robust at these frequencies, which could give them an advantage over dynamical quantum

dot pumps. As shown in the model presented here, the accuracy of this pump is directly related to the ratio between the operating frequency and the relaxation rate of the excited states. Therefore, the exact frequency domain in which the single-atom pump is the beneficial choice as a single-electron source depends on the donor relaxation rates, which is so far a not well-established parameter. The other way around, experiments on single-atom pumps could lead to more knowledge about the relaxation processes for the valley-orbit states of single donor atoms.

7.8 Conclusion

In conclusion, a model that describes the behavior of a single parameter single-atom electron pump has been presented. This model describes the loading, isolation and unloading of the electron via the robust Coulomb potential of the atom as the main steps for each pumping cycle. The most striking feature compared to dynamical quantum dot pumps, is the fact that, for atom pumps, excited states greatly enhance the accuracy by increasing the loading efficiency of the ground state via a fast relaxation process. This is in agreement with what has been recently observed experimentally by several groups[177,188] and observed in the experiment presented here. The model allows to benchmark against the position of the atom in the channel of the silicon transistor and shows that the single-atom pumps performances are unaffected by displacements of the atom up to a few tens of nm, which are at reach of the precision achieved by the current atom placement technologies.[206] Lastly, the accuracy of these pumps could be enhanced by working with more effective pulse shapes and by increasing the relaxation rate to the ground state of the atom, making single-atom electron pumps an even more attractive alternative to dynamical quantum dot charge pumps.

chapter 8

Conclusion and outlook

8.1 Conclusions

In this thesis the spin and charge dynamics of single impurities in silicon nano transistors have been investigated. The main focus is the spin-orbit system of individual acceptor atoms, which has been discussed in terms of the total angular momentum degree of freedom. Furthermore, the influence of the relaxation process of excited states on the operation of single-atom electron pumps has been studied theoretically. Acceptor atoms have been proposed as candidates for silicon spin-orbit qubits, due to the large spin-orbit coupling between heavy and light holes. However, this spin-orbit coupling makes the acceptor states highly sensitive to local strain, electric field and other defects or interfaces in their vicinity. This explains the large inhomogeneous broadening, commonly observed in resonance measurements on acceptor ensembles, which prevents the measurement of spin dynamics of these acceptor atoms. This thesis shows a different approach, where individual atoms have been studied within state-of-the-art CMOS transistors. These nano-structures have allowed the investigation of single acceptor properties, such as the energy spectrum, g-factor, and relaxation time, which are strongly influenced by their local environment. Following the experiments presented in this thesis, the following conclusions were drawn:

- By using transport and rf gate reflectometry measurement techniques it is possible to identify individual boron atoms in the channel of a silicon transistor. The charging energies and excited state spectra of bound holes can be established with transport spectroscopy. Transport via a single boron atom can be identified when the charging energy is consistent with the expected value for a bulk boron atom (44 meV) and in contrast with the charging energies usually observed for quantum dots in these structures (5 to 20 meV). Moreover, the irregular excited state spectrum of a boron atom, with the first excited state 23 meV away from the ground state, can be clearly distinguished from the evenly spaced excited state spectrum of a quantum dot. The combination of the measurements of charging energy and excited state spectrum represent the clear signature of boron atoms in the experiments presented in this thesis. Additionally, rf gate reflectometry measurements allow for the detection of atoms that are sufficiently tunnel coupled to an electrode or another atom.

- It is possible to find a single acceptor atom in a silicon nano-transistor

where the ground state is fourfold degenerate within the measurement accuracy. This is remarkable, as the effects of local strain, electric field, and the proximity to an interface are known to likely split the heavy and light hole states of the acceptor. The presence of this bulk-like fourfold degenerate acceptor state in a transistor suggests that the acceptor system can be tuned to the states preferred for realizing spin-orbit qubits by adequately controlling the strain, electric field, and magnetic field in the transistor.

- The Zeeman splitting of the states of a single acceptor reveals the influence of the local environment on the atom. Even when a bulk-like fourfold degeneracy of the ground state is observed, the measured Landé g-factors of 0.81 ± 0.06 for heavy holes and 0.85 ± 0.21 for light holes differ from the bulk value of 1.07. This indicates the effect of either a nearby Si/SiO_2 interface, local strain, or electric field on the boron atom. This effect is also highlighted by the dependence of the g-factor on the direction of the applied magnetic field, which is found to be significantly larger than expected for bulk boron atoms.

- The manipulation of the acceptor states with an electric field is experimentally demonstrated. A modification of the g-factor and a change in heavy and light hole mixing is measured as a function of a change in electric field.

- Coupled acceptor atoms are also measured in these transistors. The two-hole system of these coupled acceptors is identified by the signature of Pauli spin blockade. The tunneling of holes between the two atoms can directly be observed as a shift in the resonant frequency of a tank circuit attached to the gate of the transistor, which disappears in an applied magnetic field. This characteristic of Pauli spin blockade can be explained by the magnetic field dependence of the acceptor states and the Boltzmann distribution of the relevant states for experimental hole temperatures around 300 mK. This spin blockade effect offers a possible readout mechanism of the spin states of single acceptors.

- The relaxation time of a two-hole system of coupled acceptor atoms is measured for the first time. The relaxation time dependence on the magnetic field is measured by using the Pauli spin blockade and a pulsed measurement technique. A maximum relaxation time around 800 ns is reported. A model of the energy states of the two-hole system explains

the role of two separate heavy-light hole relaxation mechanisms on this magnetic field dependence. This experiment gives the first evidence of the expected $(\hbar\omega)^3$ behavior, while the hotspot in the relaxation rate data indicates a strong heavy-light hole mixing.

- Transport measurements reveal the light-heavy hole splitting and mixing of a single acceptor, giving valuable information about the local environment of the atom. A light-heavy hole energy splitting of 110 $\pm$ 10 μeV and a light-heavy hole exchange energy of 36 $\pm$ 5 μeV were extracted from the double acceptor transport data. Furthermore, the quantization axis of the total angular momentum of the holes changes in an applied magnetic field. In the high magnetic field limit the light-heavy hole splitting is reduced to 30 μeV, the predominantly heavy and light hole states are found closer to the pure $m_j = \pm\frac{3}{2}$ and $m_j = \pm\frac{1}{2}$ states, and bulk-like g-factors are found.

- More details about the individual and coupled acceptor atoms are revealed by microwave spectroscopy. The microwave driven resonant excitation from the bonding to the anti-bonding state of the two-hole system of coupled acceptors provides a direct measure of the tunnel coupling between the two atoms. The effect of microwaves on the tunneling between a single acceptor and the drain gives rise to a Landau-Zener-Stückelberg interference at frequencies above 17.5 GHz, indicating a coherence time around 60 ps for this system. Furthermore, photon assisted tunneling is found to cause oscillations in double acceptor transport measurements. These experiments demonstrate that individual acceptors can be influenced by microwave signals applied to the electrodes of transistors, which is an essential requirement to realize the electrically driven spin resonance of an acceptor atom.

- The dynamical behavior of donor atoms in a quantized charge pump made of a double gate transistor structure is described. The pumping accuracy of this single-donor electron pump relies on an unexpectedly favorable effect of the high lying excited states, which is in clear contrast with the more conventional quantum dot pumps. The most important ingredients for the accurate operation of the single-atom pump are the large excited state splittings and their fast relaxation rates. From this model it follows that the accuracy of these pumps is not drastically influenced by the location of the atom.

8.2 Future directions for this research

This thesis shows how the study of individual boron acceptors in silicon transistors offers a unique insight into the acceptor physics in the presence of any local strain, electric field and magnetic field. Building on the presented results, possible future experiments are discussed.

The approach to measure individual acceptors in silicon transistors can be extended further to a wide range of acceptor environments, going beyond the specific magnetic and electric field conditions investigated in this thesis. The magnetic field control can be expanded to a full three-dimensional rotation, with the use of a vector magnet or a sample rotator. Furthermore, with the use of four gates (top gate, back gate, source, and drain) a precise control over the electric field inside the transistor can be achieved. Additionally, the in situ control of strain, by using for example a piezo material, can further map out the properties of an acceptor. The light-heavy hole splitting, the light-heavy hole mixing, the Landé g-factor, the relaxation time, and the coherence time are properties of interest, all expected to have a strong dependence on the applied fields. Ultimately, the local environments proposed for acceptor qubits[93,107,109] can be achieved by the precise control over the strength and direction of all these fields.

With the identification of the heavy and light hole states of individual acceptor atoms and the possibility to apply microwaves to the gates of the transistors, shown in this thesis, the electrical driving of the spin-orbit states of the acceptor can be envisioned. Such ac driving of local gates can result in a spin resonance signal, as shown for quantum dots in III/V materials[102,105,106] and for hole quantum dots in silicon CMOS transistors.[149] The Pauli spin blockade presented in this thesis can be used as a readout scheme for the spin states of such acceptor qubits. Furthermore, the spin-orbit interaction allows for the coupling of the spin states of the acceptor to microwave cavities. A two-level spin system with a large dipole coupling, yet also with a coherence time sufficient for a qubit,[93] can be engineered by an adequate control over the acceptor environment. The coupling of a single acceptor atom to a superconducting microwave cavity enables the long-distance coupling between two acceptor atoms, which is an important component for quantum computing. All the experiments proposed here aim at optimizing the ratio between coherence time and Rabi frequency, through a precise control over the environment of the acceptors, for the realization of a new quantum computing platform based on electrically controlled acceptor atoms in silicon.

Reference list

[1] F. Seitz, "An interpretation of crystal luminescence," *Transactions of the Faraday Society*, vol. 35, pp. 74–85, 1939.

[2] N. Bohr, "On the constitution of atoms and molecules," *Philosophical Magazine Series 6*, vol. 26, no. 151, pp. 1–25, 1913.

[3] F. Bloch, "Über die Quantenmechanik der Elektronen in Kristallgittern," *Zeitschrift für Physik*, vol. 52, no. 7, pp. 555–600, 1929.

[4] A. H. Wilson, "The theory of electronic semi-conductors," *Proceedings of the Royal Society of London A: Mathematical, Physical and Engineering Sciences*, vol. 133, no. 822, pp. 458–491, 1931.

[5] N. Mott and R. Gurney, *Electronic processes in ionic crystals*. Oxford Clarendon Press, 1940.

[6] W. Shockley, *Imperfections in nearly perfect crystals*. Wiley, 1952.

[7] F. Kröger, *The chemistry of imperfect crystals*. North-Holland publishing company, 1964.

[8] G. L. Pearson and J. Bardeen, "Electrical properties of pure silicon and silicon alloys containing boron and phosphorus," *Physical Review*, vol. 75, no. 5, pp. 865–883, 1949.

[9] W. Kohn, "Shallow impurity states in silicon and germanium," vol. 5 of *Solid State Physics*, pp. 257 – 320, Academic Press, 1957.

[10] M. A. Nielsen and I. L. Chuang, *Quantum computation and quantum information*. Cambridge University Press, 2011.

[11] A. Montanaro, "Quantum algorithms: An overview," *npj Quantum Information*, vol. 2, p. 15023 EP, 2016.

[12] T. D. Ladd, F. Jelezko, R. Laflamme, Y. Nakamura, C. Monroe, and J. L. O'Brien, "Quantum computers," *Nature*, vol. 464, no. 7285, pp. 45–53, 2010.

[13] E. Gibney, "Physics: Quantum computer quest," *Nature, News Feature*, vol. 516, pp. 24 – 26, 2014.

[14] N. Gisin, G. Ribordy, W. Tittel, and H. Zbinden, "Quantum cryptography," *Reviews of Modern Physics*, vol. 74, no. 1, pp. 145–195, 2002.

[15] R. Schirhagl, K. Chang, M. Loretz, and C. L. Degen, "Nitrogen-vacancy centers in diamond: Nanoscale sensors for physics and biology," *Annual Review of Physical Chemistry*, vol. 65, no. 1, pp. 83–105, 2014.

[16] E. O. Göbel and U. Siegner, *Quantum metrology: Foundation of units and measurements*. Wiley-VCH, 2015.

[17] G. Feher, "Electron spin resonance experiments on donors in silicon. I. Electronic structure of donors by the electron nuclear double resonance technique," *Physical Review*, vol. 114, no. 5, pp. 1219–1244, 1959.

[18] G. Feher and E. A. Gere, "Electron spin resonance experiments on donors in silicon. II. Electron spin relaxation effects," *Physical Review*, vol. 114, no. 5, pp. 1245–1256, 1959.

[19] D. K. Wilson and G. Feher, "Electron spin resonance experiments on donors in silicon. III. Investigation of excited states by the application of uniaxial stress and their importance in relaxation processes," *Physical Review*, vol. 124, no. 4, pp. 1068–1083, 1961.

[20] B. E. Kane, "A silicon-based nuclear spin quantum computer," *Nature*, vol. 393, no. 6681, pp. 133–137, 1998.

[21] G. Davies and M. F. Hamer, "Optical studies of the 1.945 eV vibronic band in diamond," *Proceedings of the Royal Society of London A: Mathematical, Physical and Engineering Sciences*, vol. 348, no. 1653, pp. 285–298, 1976.

[22] J. H. N. Loubser and J. A. van Wyk, "Electron spin resonance in the study of diamond," *Reports on Progress in Physics*, vol. 41, no. 8, p. 1201, 1978.

[23] K. S. Ralls, W. J. Skocpol, L. D. Jackel, R. E. Howard, L. A. Fetter, R. W. Epworth, and D. M. Tennant, "Discrete resistance switching in submicrometer silicon inversion layers: Individual interface traps and low-frequency ($\frac{1}{f}$) noise," *Physical Review Letters*, vol. 52, no. 3, pp. 228–231, 1984.

[24] M. W. Dellow, P. H. Beton, C. J. G. M. Langerak, T. J. Foster, P. C. Main, L. Eaves, M. Henini, S. P. Beaumont, and C. D. W. Wilkinson, "Resonant tunneling through the bound states of a single donor atom in a quantum well," *Physical Review Letters*, vol. 68, no. 11, pp. 1754–1757, 1992.

[25] J. W. Sakai, T. M. Fromhold, P. H. Beton, L. Eaves, M. Henini, P. C. Main, F. W. Sheard, and G. Hill, "Probing the wave function of quantum confined states by resonant magnetotunneling," *Physical Review B*, vol. 48, no. 8, pp. 5664–5667, 1993.

[26] M. R. Deshpande, J. W. Sleight, M. A. Reed, R. G. Wheeler, and R. J. Matyi, "Spin splitting of single 0D impurity states in semiconductor heterostructure quantum wells," *Physical Review Letters*, vol. 76, no. 8, pp. 1328–1331, 1996.

[27] H. Sellier, G. P. Lansbergen, J. Caro, S. Rogge, N. Collaert, I. Ferain, M. Jurczak, and S. Biesemans, "Transport spectroscopy of a single dopant in a gated silicon nanowire," *Physical Review Letters*, vol. 97, no. 20, p. 206805, 2006.

[28] L. E. Calvet, R. G. Wheeler, and M. A. Reed, "Effect of local strain on single acceptors in Si," *Physical Review B*, vol. 76, no. 3, p. 035319, 2007.

[29] R. M. Feenstra, J. M. Woodall, and G. D. Pettit, "Observation of bulk defects by scanning tunneling microscopy and spectroscopy: Arsenic antisite defects in GaAs," *Physical Review Letters*, vol. 71, no. 8, pp. 1176–1179, 1993.

[30] P. Ebert and K. Urban, "Phosphorus vacancies and adatoms on GaP(110) surfaces studied by scanning tunneling microscopy," *Ultramicroscopy*, vol. 49, no. 1, pp. 344–353, 1993.

[31] M. B. Johnson, O. Albrektsen, R. M. Feenstra, and H. W. M. Salemink, "Direct imaging of dopants in GaAs with cross-sectional scanning tunneling microscopy," *Applied Physics Letters*, vol. 63, no. 21, pp. 2923–2925, 1993.

[32] P. Ebert, "Nano-scale properties of defects in compound semiconductor surfaces," *Surface Science Reports*, vol. 33, no. 4, pp. 121–303, 1999.

[33] A. Gruber, A. Dräbenstedt, C. Tietz, L. Fleury, J. Wrachtrup, and C. von Borczyskowski, "Scanning confocal optical microscopy and magnetic resonance on single defect centers," *Science*, vol. 276, no. 5321, pp. 2012–2014, 1997.

[34] G. A. Roberts, J. J. Finley, M. S. Skolnick, L. Eaves, J. W. Cockburn, I. A. Larkin, M. Henini, and G. Hill, "Voltage-controlled sharp-line electroluminescence in GaAs-AlAs double-barrier resonant-tunneling structures," *Physical Review B*, vol. 58, no. 8, pp. R4242–R4245, 1998.

[35] S. Francoeur, J. F. Klem, and A. Mascarenhas, "Optical spectroscopy of single impurity centers in semiconductors," *Physical Review Letters*, vol. 93, no. 6, p. 067403, 2004.

[36] S. Strauf, P. Michler, M. Klude, D. Hommel, G. Bacher, and A. Forchel, "Quantum optical studies on individual acceptor bound excitons in a semiconductor," *Physical Review Letters*, vol. 89, no. 17, p. 177403, 2002.

[37] A. Muller, P. Bianucci, C. Piermarocchi, M. Fornari, I. C. Robin, R. André, and C. K. Shih, "Time-resolved photoluminescence spectroscopy of individual Te impurity centers in ZnSe," *Physical Review B*, vol. 73, no. 8, p. 081306, 2006.

[38] M. Ikezawa, Y. Sakuma, and Y. Masumoto, "Single photon emission from individual nitrogen pairs in GaP," *Japanese Journal of Applied Physics*, vol. 46, no. 10L, p. L871, 2007.

[39] J. T. Muhonen, J. P. Dehollain, A. Laucht, F. E. Hudson, R. Kalra, T. Sekiguchi, K. M. Itoh, D. N. Jamieson, J. C. McCallum, A. S. Dzurak, and A. Morello, "Storing quantum information for 30 seconds in a nanoelectronic device," *Nature Nanotechnology*, vol. 9, no. 12, pp. 986–991, 2014.

[40] A. G. Fowler, M. Mariantoni, J. M. Martinis, and A. N. Cleland, "Surface codes: Towards practical large-scale quantum computation," *Physical Review A*, vol. 86, no. 3, p. 032324, 2012.

[41] M. Fuechsle, J. A. Miwa, S. Mahapatra, H. Ryu, S. Lee, O. Warschkow, L. C. L. Hollenberg, G. Klimeck, and M. Y. Simmons, "A single-atom transistor," *Nature Nanotechnology*, vol. 7, no. 4, pp. 242–246, 2012.

[42] C. L. Degen, "Scanning magnetic field microscope with a diamond single-spin sensor," *Applied Physics Letters*, vol. 92, no. 24, p. 243111, 2008.

[43] J. M. Taylor, P. Cappellaro, L. Childress, L. Jiang, D. Budker, P. R. Hemmer, A. Yacoby, R. Walsworth, and M. D. Lukin, "High-sensitivity diamond magnetometer with nanoscale resolution," *Nature Physics*, vol. 4, no. 10, pp. 810–816, 2008.

[44] J. R. Maze, P. L. Stanwix, J. S. Hodges, S. Hong, J. M. Taylor, P. Cappellaro, L. Jiang, M. V. G. Dutt, E. Togan, A. S. Zibrov, A. Yacoby, R. L. Walsworth, and M. D. Lukin, "Nanoscale magnetic sensing with an individual electronic spin in diamond," *Nature*, vol. 455, no. 7213, pp. 644–647, 2008.

[45] G. Balasubramanian, I. Y. Chan, R. Kolesov, M. Al-Hmoud, J. Tisler, C. Shin, C. Kim, A. Wojcik, P. R. Hemmer, A. Krueger, T. Hanke, A. Leitenstorfer, R. Bratschitsch, F. Jelezko, and J. Wrachtrup, "Nanoscale imaging magnetometry with diamond spins under ambient conditions," *Nature*, vol. 455, no. 7213, pp. 648–651, 2008.

[46] F. Dolde, H. Fedder, M. W. Doherty, T. Nobauer, F. Rempp, G. Balasubramanian, T. Wolf, F. Reinhard, L. C. L. Hollenberg, F. Jelezko, and J. Wrachtrup, "Electric-field sensing using single diamond spins," *Nature Physics*, vol. 7, no. 6, pp. 459–463, 2011.

[47] V. M. Acosta, E. Bauch, M. P. Ledbetter, A. Waxman, L. S. Bouchard, and D. Budker, "Temperature dependence of the nitrogen-vacancy magnetic resonance in diamond," *Physical Review Letters*, vol. 104, no. 7, p. 070801, 2010.

[48] G. Kucsko, P. C. Maurer, N. Y. Yao, M. Kubo, H. J. Noh, P. K. Lo, H. Park, and M. D. Lukin, "Nanometre-scale thermometry in a living cell," *Nature*, vol. 500, no. 7460, pp. 54–58, 2013.

[49] M. W. Doherty, V. V. Struzhkin, D. A. Simpson, L. P. McGuinness, Y. Meng, A. Stacey, T. J. Karle, R. J. Hemley, N. B. Manson, L. C. L. Hollenberg, and

S. Prawer, "Electronic properties and metrology applications of the diamond NV^- center under pressure," *Physical Review Letters*, vol. 112, no. 4, p. 047601, 2014.

[50] G. Waldherr, P. Neumann, S. F. Huelga, F. Jelezko, and J. Wrachtrup, "Violation of a temporal bell inequality for single spins in a diamond defect center," *Physical Review Letters*, vol. 107, no. 9, p. 090401, 2011.

[51] B. Hensen, H. Bernien, A. E. Dreau, A. Reiserer, N. Kalb, M. S. Blok, J. Ruitenberg, R. F. L. Vermeulen, R. N. Schouten, C. Abellan, W. Amaya, V. Pruneri, M. W. Mitchell, M. Markham, D. J. Twitchen, D. Elkouss, S. Wehner, T. H. Taminiau, and R. Hanson, "Loophole-free Bell inequality violation using electron spins separated by 1.3 kilometres," *Nature*, vol. 526, no. 7575, pp. 682–686, 2015.

[52] W. Shockley, M. Sparks, and G. K. Teal, "$p-n$ junction transistors," *Physical Review*, vol. 83, no. 1, pp. 151–162, 1951.

[53] K. Kuhn, C. Kenyon, A. Kornfeld, M. Liu, A. Maheshwari, W.-k. Shih, S. Sivakumar, G. Taylor, P. VanDerVoorn, and K. Zawadzki, "Managing process variation in Intel's 45nm CMOS technology.," *Intel Technology Journal*, vol. 12, no. 2, pp. 93–109, 2008.

[54] X. Wang, A. R. Brown, N. Idris, S. Markov, G. Roy, and A. Asenov, "Statistical threshold-voltage variability in scaled decananometer bulk HKMG MOSFETs: A full-scale 3-D simulation scaling study," *IEEE Transactions on Electron Devices*, vol. 58, no. 8, pp. 2293–2301, 2011.

[55] J. Verduijn, G. C. Tettamanzi, and S. Rogge, "Wave function control over a single donor atom," *Nano Letters*, vol. 13, no. 4, pp. 1476–1480, 2013.

[56] L. E. Calvet, J. P. Snyder, and W. Wernsdorfer, "Excited-state spectroscopy of single Pt atoms in Si," *Physical Review B*, vol. 78, no. 19, p. 195309, 2008.

[57] G. P. Lansbergen, R. Rahman, C. J. Wellard, I. Woo, J. Caro, N. Collaert, S. Biesemans, G. Klimeck, L. C. L. Hollenberg, and S. Rogge, "Gate-induced quantum-confinement transition of a single dopant atom in a silicon FinFET," *Nature Physics*, vol. 4, no. 8, pp. 656–661, 2008.

[58] M. A. H. Khalafalla, Y. Ono, K. Nishiguchi, and A. Fujiwara, "Horizontal position analysis of single acceptors in Si nanoscale field-effect transistors," *Applied Physics Letters*, vol. 94, no. 22, p. 223501, 2009.

[59] M. Pierre, R. Wacquez, X. Jehl, M. Sanquer, M. Vinet, and O. Cueto, "Single-donor ionization energies in a nanoscale CMOS channel," *Nature Nanotechnology*, vol. 5, no. 2, pp. 133–137, 2010.

[60] B. Koiller, X. Hu, and S. Das Sarma, "Exchange in silicon-based quantum computer architecture," *Physical Review Letters*, vol. 88, no. 2, p. 027903, 2001.

[61] S. Zwerdling, K. J. Button, B. Lax, and L. M. Roth, "Internal impurity levels in semiconductors: Experiments in p-type silicon," *Physical Review Letters*, vol. 4, no. 4, pp. 173–176, 1960.

[62] E. Burstein, E. E. Bell, J. W. Davisson, and M. Lax, "Optical investigations of impurity levels in silicon," *The Journal of Physical Chemistry*, vol. 57, no. 8, pp. 849–852, 1953.

[63] A. Onton, P. Fisher, and A. K. Ramdas, "Spectroscopic investigation of group-III acceptor states in silicon," *Physical Review*, vol. 163, no. 3, pp. 686–703, 1967.

[64] G. B. Wright and A. Mooradian, "Raman scattering from donor and acceptor impurities in silicon," *Physical Review Letters*, vol. 18, no. 15, pp. 608–610, 1967.

[65] S. G. Pavlov, N. Deßmann, V. N. Shastin, R. K. Zhukavin, B. Redlich, A. F. G. van der Meer, M. Mittendorff, S. Winnerl, N. V. Abrosimov, H. Riemann, and H. W. Hübers, "Terahertz stimulated emission from silicon doped by hydrogenlike acceptors," *Physical Review X*, vol. 4, no. 2, p. 021009, 2014.

[66] K. J. Morse, R. J. S. Abraham, D. P. Franke, N. V. Abrosimov, and M. L. W. Thewalt, "Even-parity excited states of the acceptor boron in silicon revisited," *Physical Review B*, vol. 93, no. 12, p. 125207, 2016.

[67] D. Schechter, "Theory of shallow acceptor states in Si and Ge," *Journal of Physics and Chemistry of Solids*, vol. 23, no. 3, pp. 237–247, 1962.

[68] W. Kohn and J. M. Luttinger, "Theory of donor states in silicon," *Physical Review*, vol. 98, no. 4, pp. 915–922, 1955.

[69] A. Baldereschi and N. O. Lipari, "Spherical model of shallow acceptor states in semiconductors," *Physical Review B*, vol. 8, no. 6, pp. 2697–2709, 1973.

[70] A. Baldereschi and N. O. Lipari, "Cubic contributions to the spherical model of shallow acceptor states," *Physical Review B*, vol. 9, no. 4, pp. 1525–1539, 1974.

[71] A. K. Ramdas and S. Rodriguez, "Spectroscopy of the solid-state analogues of the hydrogen atom: Donors and acceptors in semiconductors," *Reports on Progress in Physics*, vol. 44, no. 12, p. 1297, 1981.

[72] J. M. Luttinger, "Quantum theory of cyclotron resonance in semiconductors: general theory," *Physical Review*, vol. 102, no. 4, pp. 1030–1041, 1956.

[73] G. L. Bir, E. I. Butikov, and G. E. Pikus, "Spin and combined resonance on acceptor centres in Ge and Si type crystals—I: Paramagnetic resonance in strained and unstrained crystals," *Journal of Physics and Chemistry of Solids*, vol. 24, no. 12, pp. 1467–1474, 1963.

[74] A. K. Bhattacharjee and S. Rodriguez, “Group-theoretical study of the Zeeman effect of acceptors in silicon and germanium,” *Physical Review B*, vol. 6, no. 10, pp. 3836–3856, 1972.

[75] A. Köpf and K. Lassmann, “Linear Stark and nonlinear Zeeman coupling to the ground state of effective mass acceptors in silicon,” *Physical Review Letters*, vol. 69, no. 10, pp. 1580–1583, 1992.

[76] G. Feher, J. C. Hensel, and E. A. Gere, “Paramagnetic resonance absorption from acceptors in silicon,” *Physical Review Letters*, vol. 5, no. 7, pp. 309–311, 1960.

[77] T. Shimizu and N. Tanaka, “Stress dependence of g-tensor for boron acceptor in silicon,” *Physics Letters A*, vol. 45, no. 1, pp. 5–6, 1973.

[78] H. Neubrand, “ESR from boron in silicon at zero and small external stress. I. Line positions and line structure,” *Physica Status Solidi B*, vol. 86, no. 1, pp. 269–275, 1978.

[79] A. R. Stegner, H. Tezuka, T. Andlauer, M. Stutzmann, M. L. W. Thewalt, M. S. Brandt, and K. M. Itoh, “Isotope effect on electron paramagnetic resonance of boron acceptors in silicon,” *Physical Review B*, vol. 82, no. 11, p. 115213, 2010.

[80] J. M. Cherlow, R. L. Aggarwal, and B. Lax, “Raman scattering and photoluminescence in boron-doped and arsenic-doped silicon,” *Physical Review B*, vol. 7, no. 10, pp. 4547–4560, 1973.

[81] F. Merlet, B. Pajot, P. Arcas, and A. M. Jean-Louis, “Experimental study of the Zeeman splitting of boron levels in silicon,” *Physical Review B*, vol. 12, no. 8, pp. 3297–3317, 1975.

[82] H. Zeile and K. Lassmann, “Ultrasonic investigation of the acceptor ground state of Si(B) II. The distribution of splittings,” *Physica Status Solidi B*, vol. 111, no. 2, pp. 555–564, 1982.

[83] H. Neubrand, “ESR from boron in silicon at zero and small external stress. II. Linewidth and crystal defects,” *Physica Status Solidi B*, vol. 90, no. 1, pp. 301–308, 1978.

[84] Y. Yafet, “Paramagnetic relaxation of shallow acceptor states in semiconductors,” *Journal of Physics and Chemistry of Solids*, vol. 26, no. 3, pp. 647–651, 1965.

[85] D. Karaiskaj, M. L. W. Thewalt, T. Ruf, M. Cardona, and M. Konuma, “"intrinsic" acceptor ground state splitting in silicon: an isotopic effect,” *Physical Review Letters*, vol. 89, no. 1, p. 016401, 2002.

[86] D. Karaiskaj, G. Kirczenow, M. L. W. Thewalt, R. Buczko, and M. Cardona, "Origin of the residual acceptor ground-state splitting in silicon," *Physical Review Letters*, vol. 90, no. 1, p. 016404, 2003.

[87] G. L. Bir, E. I. Butikov, and G. E. Pikus, "Spin and combined resonance on acceptor centres in Ge and Si type crystals—II: The effect of the electrical field and relaxation time," *Journal of Physics and Chemistry of Solids*, vol. 24, no. 12, pp. 1475–1486, 1963.

[88] L. E. Calvet, R. G. Wheeler, and M. A. Reed, "Observation of the linear Stark effect in a single acceptor in Si," *Physical Review Letters*, vol. 98, no. 9, p. 096805, 2007.

[89] J. A. Mol, J. Salfi, J. A. Miwa, M. Y. Simmons, and S. Rogge, "Interplay between quantum confinement and dielectric mismatch for ultrashallow dopants," *Physical Review B*, vol. 87, no. 24, p. 245417, 2013.

[90] G. D. J. Smit, S. Rogge, J. Caro, and T. M. Klapwijk, "Group-theoretical analysis of double acceptors in a magnetic field: Identification of the Si:B^+ ground state," *Physical Review B*, vol. 69, no. 8, p. 085211, 2004.

[91] J. Salfi, J. A. Mol, R. Rahman, G. Klimeck, M. Y. Simmons, L. C. L. Hollenberg, and S. Rogge, "Quantum simulation of the Hubbard model with dopant atoms in silicon," *Nature Communications*, vol. 7, p. 11342, 2016.

[92] E. Kartheuser and S. Rodriguez, "Group-theoretical study of double acceptors in semiconductors under uniaxial stress," *Physical Review B*, vol. 8, no. 4, pp. 1556–1570, 1973.

[93] J. Salfi, J. A. Mol, D. Culcer, and S. Rogge, "Charge-insensitive single-atom spin-orbit qubit in silicon," *Physical Review Letters*, vol. 116, no. 24, p. 246801, 2016.

[94] F. Jelezko, T. Gaebel, I. Popa, A. Gruber, and J. Wrachtrup, "Observation of coherent oscillations in a single electron spin," *Physical Review Letters*, vol. 92, no. 7, p. 076401, 2004.

[95] T. Gaebel, M. Domhan, I. Popa, C. Wittmann, P. Neumann, F. Jelezko, J. R. Rabeau, N. Stavrias, A. D. Greentree, S. Prawer, J. Meijer, J. Twamley, P. R. Hemmer, and J. Wrachtrup, "Room-temperature coherent coupling of single spins in diamond," *Nature Physics*, vol. 2, no. 6, pp. 408–413, 2006.

[96] J. Meijer, B. Burchard, M. Domhan, C. Wittmann, T. Gaebel, I. Popa, F. Jelezko, and J. Wrachtrup, "Generation of single color centers by focused nitrogen implantation," *Applied Physics Letters*, vol. 87, no. 26, p. 261909, 2005.

[97] S. Sangtawesin, T. O. Brundage, Z. J. Atkins, and J. R. Petta, "Highly tunable formation of nitrogen-vacancy centers via ion implantation," *Applied Physics Letters*, vol. 105, no. 6, p. 063107, 2014.

[98] A. Morello, J. J. Pla, F. A. Zwanenburg, K. W. Chan, K. Y. Tan, H. Huebl, M. Mottonen, C. D. Nugroho, C. Yang, J. A. van Donkelaar, A. D. C. Alves, D. N. Jamieson, C. C. Escott, L. C. L. Hollenberg, R. G. Clark, and A. S. Dzurak, "Single-shot readout of an electron spin in silicon," *Nature*, vol. 467, no. 7316, pp. 687–691, 2010.

[99] J. J. Pla, K. Y. Tan, J. P. Dehollain, W. H. Lim, J. J. L. Morton, D. N. Jamieson, A. S. Dzurak, and A. Morello, "A single-atom electron spin qubit in silicon," *Nature*, vol. 489, no. 7417, pp. 541–545, 2012.

[100] J. J. Pla, K. Y. Tan, J. P. Dehollain, W. H. Lim, J. J. L. Morton, F. A. Zwanenburg, D. N. Jamieson, A. S. Dzurak, and A. Morello, "High-fidelity readout and control of a nuclear spin qubit in silicon," *Nature*, vol. 496, no. 7445, pp. 334–338, 2013.

[101] V. N. Golovach, M. Borhani, and D. Loss, "Electric-dipole-induced spin resonance in quantum dots," *Physical Review B*, vol. 74, no. 16, p. 165319, 2006.

[102] K. C. Nowack, F. H. L. Koppens, Y. V. Nazarov, and L. M. K. Vandersypen, "Coherent control of a single electron spin with electric fields," *Science*, vol. 318, no. 5855, pp. 1430–1433, 2007.

[103] A. Blais, R.-S. Huang, A. Wallraff, S. M. Girvin, and R. J. Schoelkopf, "Cavity quantum electrodynamics for superconducting electrical circuits: An architecture for quantum computation," *Physical Review A*, vol. 69, no. 6, p. 062320, 2004.

[104] K. D. Petersson, L. W. McFaul, M. D. Schroer, M. Jung, J. M. Taylor, A. A. Houck, and J. R. Petta, "Circuit quantum electrodynamics with a spin qubit," *Nature*, vol. 490, no. 7420, pp. 380–383, 2012.

[105] S. Nadj-Perge, S. M. Frolov, E. P. A. M. Bakkers, and L. P. Kouwenhoven, "Spin-orbit qubit in a semiconductor nanowire," *Nature*, vol. 468, no. 7327, pp. 1084–1087, 2010.

[106] V. S. Pribiag, S. Nadj-Perge, S. M. Frolov, J. W. G. van den Berg, I. van Weperen, S. R. Plissard, E. P. A. M. Bakkers, and L. P. Kouwenhoven, "Electrical control of single hole spins in nanowire quantum dots," *Nature Nanotechnology*, vol. 8, no. 3, pp. 170–174, 2013.

[107] R. Ruskov and C. Tahan, "On-chip cavity quantum phonodynamics with an acceptor qubit in silicon," *Physical Review B*, vol. 88, no. 6, p. 064308, 2013.

[108] B. Golding and M. Dykman, "Acceptor-based silicon quantum computing," *arXiv:cond-mat/0309147*, 2003.

[109] J. Salfi, M. Tong, S. Rogge, and D. Culcer, "Quantum computing with acceptor spins in silicon," *Nanotechnology*, vol. 27, no. 24, p. 244001, 2016.

[110] E. A. Chekhovich, M. M. Glazov, A. B. Krysa, M. Hopkinson, P. Senellart, A. Lemaitre, M. S. Skolnick, and A. I. Tartakovskii, "Element-sensitive measurement of the hole-nuclear spin interaction in quantum dots," *Nature Physics*, vol. 9, no. 2, pp. 74–78, 2013.

[111] Y. P. Song and B. Golding, "Manipulation and decoherence of acceptor states in silicon," *Europhysics Letters*, vol. 95, no. 4, p. 47004, 2011.

[112] P. Dirksen, A. Henstra, and W. T. Wenckebach, "An ESR hole burning study of dynamic nuclear polarisation of 29 Si in Si:B," *Journal of Physics: Condensed Matter*, vol. 1, no. 44, p. 8535, 1989.

[113] N. Q. Vinh, B. Redlich, A. F. G. van der Meer, C. R. Pidgeon, P. T. Greenland, S. A. Lynch, G. Aeppli, and B. N. Murdin, "Time-resolved dynamics of shallow acceptor transitions in silicon," *Physical Review X*, vol. 3, no. 1, p. 011019, 2013.

[114] A. Chaudhry and M. J. Kumar, "Controlling short-channel effects in deep-submicron SOI MOSFETs for improved reliability: A review," *IEEE Transactions on Device and Materials Reliability*, vol. 4, no. 1, pp. 99–109, 2004.

[115] A. K. Kambham, A. Kumar, A. Florakis, and W. Vandervorst, "Three-dimensional doping and diffusion in nano scaled devices as studied by atom probe tomography," *Nanotechnology*, vol. 24, no. 27, p. 275705, 2013.

[116] I. Ferain, R. Duffy, N. Collaert, M. J. H. van Dal, B. J. Pawlak, B. O'Sullivan, L. Witters, R. Rooyackers, T. Conard, M. Popovici, S. van Elshocht, M. Kaiser, R. G. R. Weemaes, J. Swerts, M. Jurczak, R. J. P. Lander, and K. De Meyer, "Performance improvement in narrow MuGFETs by gate work function and source/drain implant engineering," *Solid-State Electronincs*, vol. 53, no. 7, pp. 760–766, 2009.

[117] J. van der Heijden, J. Salfi, J. A. Mol, J. Verduijn, G. C. Tettamanzi, A. R. Hamilton, N. Collaert, and S. Rogge, "Probing the spin states of a single acceptor atom," *Nano Letters*, vol. 14, no. 3, pp. 1492–1496, 2014.

[118] B. Voisin, V.-H. Nguyen, J. Renard, X. Jehl, S. Barraud, F. Triozon, M. Vinet, I. Duchemin, Y.-M. Niquet, S. de Franceschi, and M. Sanquer, "Few-electron edge-state quantum dots in a silicon nanowire field-effect transistor," *Nano Letters*, vol. 14, no. 4, pp. 2094–2098, 2014.

[119] H. Sellier, G. P. Lansbergen, J. Caro, S. Rogge, N. Collaert, I. Ferain, M. Jurczak, and S. Biesemans, "Subthreshold channels at the edges of nanoscale triple-gate silicon transistors," *Applied Physics Letters*, vol. 90, no. 7, p. 073502, 2007.

[120] W. Burger and K. Lassmann, "Energy-resolved measurements of the phonon-ionization of D^- and A^+ centers in silicon with superconducting-Al tunnel junctions," *Physical Review Letters*, vol. 53, no. 21, pp. 2035–2037, 1984.

[121] R. Rahman, G. P. Lansbergen, J. Verduijn, G. C. Tettamanzi, S. H. Park, N. Collaert, S. Biesemans, G. Klimeck, L. C. L. Hollenberg, and S. Rogge, "Electric field reduced charging energies and two-electron bound excited states of single donors in silicon," *Physical Review B*, vol. 84, no. 11, p. 115428, 2011.

[122] C. Beenakker, "Theory of Coulomb blockade oscillations in the conductance of a quantum dot," *Physical Review B*, vol. 44, no. 4, pp. 1646–1656, 1991.

[123] G. P. Lansbergen, R. Rahman, J. Verduijn, G. C. Tettamanzi, N. Collaert, S. Biesemans, G. Klimeck, L. C. L. Hollenberg, and S. Rogge, "Lifetime-enhanced transport in silicon due to spin and valley blockade," *Physical Review Letters*, vol. 107, no. 13, p. 136602, 2011.

[124] W. G. van der Wiel, S. De Franceschi, J. M. Elzerman, T. Fujisawa, S. Tarucha, and L. P. Kouwenhoven, "Electron transport through double quantum dots," *Reviews of Modern Physics*, vol. 75, no. 1, pp. 1–22, 2002.

[125] K. D. Petersson, C. G. Smith, D. Anderson, P. Atkinson, G. A. C. Jones, and D. A. Ritchie, "Charge and spin state readout of a double quantum dot coupled to a resonator," *Nano Letters*, vol. 10, no. 8, pp. 2789–2793, 2010.

[126] J. I. Colless, A. C. Mahoney, J. M. Hornibrook, A. C. Doherty, H. Lu, A. C. Gossard, and D. J. Reilly, "Dispersive readout of a few-electron double quantum dot with fast rf gate sensors," *Physical Review Letters*, vol. 110, no. 4, p. 046805, 2013.

[127] J. Verduijn, M. Vinet, and S. Rogge, "Radio-frequency dispersive detection of donor atoms in a field-effect transistor," *Applied Physics Letters*, vol. 104, no. 10, p. 102107, 2014.

[128] M. F. Gonzalez-Zalba, S. Barraud, A. J. Ferguson, and A. C. Betz, "Probing the limits of gate-based charge sensing," *Nature Communications*, vol. 6, p. 6084, 2015.

[129] M. G. House, T. Kobayashi, B. Weber, S. J. Hile, T. F. Watson, J. van der Heijden, S. Rogge, and M. Y. Simmons, "Radio frequency measurements of tunnel couplings and singlet-triplet spin states in Si:P quantum dots," *Nature Communications*, vol. 6, p. 8848, 2015.

[130] L. J. Taskinen, R. P. Starrett, T. P. Martin, A. P. Micolich, A. R. Hamilton, M. Y. Simmons, D. A. Ritchie, and M. Pepper, "Radio-frequency reflectometry on large gated two-dimensional systems," *Review of Scientific Instruments*, vol. 79, no. 12, p. 123901, 2008.

[131] R. J. Schoelkopf, P. Wahlgren, A. A. Kozhevnikov, P. Delsing, and D. E. Prober, "The radio-frequency single-electron transistor (rf-SET): A fast and ultrasensitive electrometer," *Science*, vol. 280, no. 5367, pp. 1238–1242, 1998.

[132] H. Brenning, S. Kafanov, T. Duty, S. Kubatkin, and P. Delsing, "An ultrasensitive radio-frequency single-electron transistor working up to 4.2 K," *Journal of Applied Physics*, vol. 100, no. 11, p. 114321, 2006.

[133] M. C. Cassidy, A. S. Dzurak, R. G. Clark, K. D. Petersson, I. Farrer, D. A. Ritchie, and C. G. Smith, "Single shot charge detection using a radio-frequency quantum point contact," *Applied Physics Letters*, vol. 91, no. 22, p. 222104, 2007.

[134] D. J. Reilly, C. M. Marcus, M. P. Hanson, and A. C. Gossard, "Fast single-charge sensing with a rf quantum point contact," *Applied Physics Letters*, vol. 91, no. 16, p. 162101, 2007.

[135] H. L. Stormer, Z. Schlesinger, A. Chang, D. C. Tsui, A. C. Gossard, and W. Wiegmann, "Energy structure and quantized Hall effect of two-dimensional holes," *Physical Review Letters*, vol. 51, no. 2, pp. 126–129, 1983.

[136] A. Srinivasan, L. A. Yeoh, O. Klochan, T. P. Martin, J. C. H. Chen, A. P. Micolich, A. R. Hamilton, D. Reuter, and A. D. Wieck, "Using a tunable quantum wire to measure the large out-of-plane spin splitting of quasi two-dimensional holes in a GaAs nanostructure," *Nano Letters*, vol. 13, no. 1, pp. 148–152, 2012.

[137] U. Zülicke and D. Csontos, "Zeeman splitting in cylindrical hole quantum wires," *Current Applied Physics*, vol. 8, no. 3–4, pp. 237–240, 2008.

[138] D. V. Bulaev and D. Loss, "Spin relaxation and decoherence of holes in quantum dots," *Physical Review Letters*, vol. 95, no. 7, p. 076805, 2005.

[139] D. Heiss, S. Schaeck, H. Huebl, M. Bichler, G. Abstreiter, J. J. Finley, D. V. Bulaev, and D. Loss, "Observation of extremely slow hole spin relaxation in self-assembled quantum dots," *Physical Review B*, vol. 76, no. 24, p. 241306, 2007.

[140] O. Klochan, W. R. Clarke, R. Danneau, A. P. Micolich, L. H. Ho, A. R. Hamilton, K. Muraki, and Y. Hirayama, "Ballistic transport in induced one-dimensional hole systems," *Applied Physics Letters*, vol. 89, no. 9, p. 092105, 2006.

[141] D. Brunner, B. D. Gerardot, P. A. Dalgarno, G. Wüst, K. Karrai, N. G. Stoltz, P. M. Petroff, and R. J. Warburton, "A coherent single-hole spin in a semiconductor," *Science*, vol. 325, no. 5936, pp. 70–72, 2009.

[142] K. De Greve, P. L. McMahon, D. Press, T. D. Ladd, D. Bisping, C. Schneider, M. Kamp, L. Worschech, S. Hofling, A. Forchel, and Y. Yamamoto, "Ultrafast coherent control and suppressed nuclear feedback of a single quantum dot hole qubit," *Nature Physics*, vol. 7, no. 11, pp. 872–878, 2011.

[143] F. A. Zwanenburg, C. E. W. M. van Rijmenam, Y. Fang, C. M. Lieber, and L. P. Kouwenhoven, "Spin states of the first four holes in a silicon nanowire quantum dot," *Nano Letters*, vol. 9, no. 3, pp. 1071–1079, 2009.

[144] Y. Hu, F. Kuemmeth, C. M. Lieber, and C. M. Marcus, "Hole spin relaxation in Ge-Si core-shell nanowire qubits," *Nature Nanotechnology*, vol. 7, no. 1, pp. 47–50, 2012.

[145] P. C. Spruijtenburg, J. Ridderbos, F. Mueller, A. W. Leenstra, M. Brauns, A. A. I. Aarnink, W. G. van der Wiel, and F. A. Zwanenburg, "Single-hole tunneling through a two-dimensional hole gas in intrinsic silicon," *Applied Physics Letters*, vol. 102, no. 19, p. 192105, 2013.

[146] R. Li, F. E. Hudson, A. S. Dzurak, and A. R. Hamilton, "Single hole transport in a silicon metal-oxide-semiconductor quantum dot," *Applied Physics Letters*, vol. 103, no. 16, p. 163508, 2013.

[147] R. Li, F. E. Hudson, A. S. Dzurak, and A. R. Hamilton, "Pauli spin blockade of heavy holes in a silicon double quantum dot," *Nano Letters*, vol. 15, no. 11, pp. 7314–7318, 2015.

[148] B. Voisin, R. Maurand, S. Barraud, M. Vinet, X. Jehl, M. Sanquer, J. Renard, and S. D. Franceschi, "Electrical control of g-factor in a few-hole silicon nanowire MOSFET," *Nano Letters*, vol. 16, no. 1, pp. 88–92, 2016.

[149] R. Maurand, X. Jehl, D. Kotekar-Patil, A. Corna, H. Bohuslavskyi, R. Laviéville, L. Hutin, S. Barraud, M. Vinet, M. Sanquer, and S. De Franceschi, "A CMOS silicon spin qubit," *Nature Communications*, vol. 7, p. 13575, 2016.

[150] J.-M. Tang, J. Levy, and M. E. Flatté, "All-electrical control of single ion spins in a semiconductor," *Physical Review Letters*, vol. 97, no. 10, p. 106803, 2006.

[151] H. Tezuka, A. R. Stegner, A. M. Tyryshkin, S. Shankar, M. L. W. Thewalt, S. A. Lyon, K. M. Itoh, and M. S. Brandt, "Electron paramagnetic resonance of boron acceptors in isotopically purified silicon," *Physical Review B*, vol. 81, no. 16, p. 161203, 2010.

[152] G. C. Tettamanzi, J. Verduijn, G. P. Lansbergen, M. Blaauboer, M. J. Calderón, R. Aguado, and S. Rogge, "Magnetic-field probing of an SU(4) Kondo resonance in a single-atom transistor," *Physical Review Letters*, vol. 108, no. 4, p. 046803, 2012.

[153] J. Verduijn, R. R. Agundez, M. Blaauboer, and S. Rogge, "Non-local coupling of two donor-bound electrons," *New Journal of Physics*, vol. 15, no. 3, p. 033020, 2013.

[154] K. Y. Tan, K. W. Chan, M. Möttönen, A. Morello, C. Yang, J. v. Donkelaar, A. Alves, J.-M. Pirkkalainen, D. N. Jamieson, R. G. Clark, and A. S. Dzurak, "Transport spectroscopy of single phosphorus donors in a silicon nanoscale transistor," *Nano Letters*, vol. 10, no. 1, pp. 11–15, 2009.

[155] M. A. H. Khalafalla, Y. Ono, K. Nishiguchi, and A. Fujiwara, "Identification of single and coupled acceptors in silicon nano-field-effect transistors," *Applied Physics Letters*, vol. 91, no. 26, p. 263513, 2007.

[156] B. J. Villis, A. O. Orlov, X. Jehl, G. L. Snider, P. Fay, and M. Sanquer, "Defect detection in nano-scale transistors based on radio-frequency reflectometry," *Applied Physics Letters*, vol. 99, no. 15, p. 152106, 2011.

[157] M. Möttönen, K. Y. Tan, K. W. Chan, F. A. Zwanenburg, W. H. Lim, C. C. Escott, J. M. Pirkkalainen, A. Morello, C. Yang, J. A. van Donkelaar, A. D. C. Alves, D. N. Jamieson, L. C. L. Hollenberg, and A. S. Dzurak, "Probe and control of the reservoir density of states in single-electron devices," *Physical Review B*, vol. 81, no. 16, p. 161304, 2010.

[158] E. B. Foxman, P. L. McEuen, U. Meirav, N. S. Wingreen, Y. Meir, P. A. Belk, N. R. Belk, M. A. Kastner, and S. J. Wind, "Effects of quantum levels on transport through a Coulomb island," *Physical Review B*, vol. 47, no. 15, pp. 10020–10023, 1993.

[159] D. Gammon, R. Merlin, W. T. Masselink, and H. Morkoc, "Raman spectra of shallow acceptors in quantum-well structures," *Physical Review B*, vol. 33, no. 4, pp. 2919–2922, 1986.

[160] M. V. Gustafsson, T. Aref, A. F. Kockum, M. K. Ekström, G. Johansson, and P. Delsing, "Propagating phonons coupled to an artificial atom," *Science*, vol. 346, no. 6206, pp. 207–211, 2014.

[161] J. C. Abadillo-Uriel and M. J. Calderón, "Interface effects on acceptor qubits in silicon and germanium," *Nanotechnology*, vol. 27, no. 2, p. 024003, 2016.

[162] D. Miserev and O. Sushkov, "G-factors of hole bound states in spherically symmetric potentials in cubic semiconductors," *The European Physical Journal B*, vol. 89, no. 3, pp. 1–10, 2016.

[163] M. Urdampilleta, A. Chatterjee, C. C. Lo, T. Kobayashi, J. Mansir, S. Barraud, A. C. Betz, S. Rogge, M. F. Gonzalez-Zalba, and J. J. L. Morton, "Charge dynamics and spin blockade in a hybrid double quantum dot in silicon," *Physical Review X*, vol. 5, no. 3, p. 031024, 2015.

[164] F. H. L. Koppens, C. Buizert, K. J. Tielrooij, I. T. Vink, K. C. Nowack, T. Meunier, L. P. Kouwenhoven, and L. M. K. Vandersypen, "Driven coherent oscillations of a single electron spin in a quantum dot," *Nature*, vol. 442, no. 7104, pp. 766–771, 2006.

[165] C. Tahan and R. Joynt, "Relaxation of excited spin, orbital, and valley qubit states in ideal silicon quantum dots," *Physical Review B*, vol. 89, no. 7, p. 075302, 2014.

[166] S. N. Shevchenko, S. Ashhab, and F. Nori, "Landau–Zener–Stückelberg interferometry," *Physics Reports*, vol. 492, no. 1, pp. 1–30, 2010.

[167] E. Dupont-Ferrier, B. Roche, B. Voisin, X. Jehl, R. Wacquez, M. Vinet, M. Sanquer, and S. De Franceschi, "Coherent coupling of two dopants in a silicon nanowire probed by Landau-Zener-Stückelberg interferometry," *Physical Review Letters*, vol. 110, no. 13, p. 136802, 2013.

[168] M. F. Gonzalez-Zalba, S. N. Shevchenko, S. Barraud, J. R. Johansson, A. J. Ferguson, F. Nori, and A. C. Betz, "Gate-sensing coherent charge oscillations in a silicon field-effect transistor," *Nano Letters*, vol. 16, no. 3, pp. 1614–1619, 2016.

[169] M. Sillanpää, T. Lehtinen, A. Paila, Y. Makhlin, and P. Hakonen, "Continuous-time monitoring of Landau-Zener interference in a Cooper-pair box," *Physical Review Letters*, vol. 96, no. 18, p. 187002, 2006.

[170] J. R. Petta, A. C. Johnson, C. M. Marcus, M. P. Hanson, and A. C. Gossard, "Manipulation of a single charge in a double quantum dot," *Physical Review Letters*, vol. 93, no. 18, p. 186802, 2004.

[171] E. A. Laird, F. Pei, and L. P. Kouwenhoven, "A valley-spin qubit in a carbon nanotube," *Nature Nanotechnology*, vol. 8, no. 8, pp. 565–568, 2013.

[172] L. P. Kouwenhoven, A. T. Johnson, N. C. van der Vaart, C. J. P. M. Harmans, and C. T. Foxon, "Quantized current in a quantum-dot turnstile using oscillating tunnel barriers," *Physical Review Letters*, vol. 67, no. 12, pp. 1626–1629, 1991.

[173] H. Pothier, P. Lafarge, C. Urbina, D. Esteve, and M. H. Devoret, "Single-electron pump based on charging effects," *Europhysics Letters*, vol. 17, no. 3, p. 249, 1992.

[174] M. D. Blumenthal, B. Kaestner, L. Li, S. Giblin, T. J. B. M. Janssen, M. Pepper, D. Anderson, G. Jones, and D. A. Ritchie, "Gigahertz quantized charge pumping," *Nature Physics*, vol. 3, no. 5, pp. 343–347, 2007.

[175] S. P. Giblin, M. Kataoka, J. D. Fletcher, P. See, T. J. B. M. Janssen, J. P. Griffiths, G. A. C. Jones, I. Farrer, and D. A. Ritchie, "Towards a quantum representation of the ampere using single electron pumps," *Nature Communications*, vol. 3, p. 930, 2012.

[176] A. Rossi, T. Tanttu, K. Y. Tan, I. Iisakka, R. Zhao, K. W. Chan, G. C. Tettamanzi, S. Rogge, A. S. Dzurak, and M. Möttönen, "An accurate single-electron pump based on a highly tunable silicon quantum dot," *Nano Letters*, vol. 14, no. 6, pp. 3405–3411, 2014.

[177] G. C. Tettamanzi, R. Wacquez, and S. Rogge, "Charge pumping through a single donor atom," *New Journal of Physics*, vol. 16, no. 6, p. 063036, 2014.

[178] N. Ubbelohde, F. Hohls, V. Kashcheyevs, T. Wagner, L. Fricke, B. Kästner, K. Pierz, H. W. Schumacher, and R. J. Haug, "Partitioning of on-demand electron pairs," *Nature Nanotechnology*, vol. 10, no. 1, pp. 46–49, 2015.

[179] M. Kataoka, N. Johnson, C. Emary, P. See, J. P. Griffiths, G. A. C. Jones, I. Farrer, D. A. Ritchie, M. Pepper, and T. J. B. M. Janssen, "Time-of-flight measurements of single-electron wave packets in quantum Hall edge states," *Physical Review Letters*, vol. 116, no. 12, p. 126803, 2016.

[180] M. J. T. Milton, J. M. Williams, and A. B. Forbes, "The quantum metrology triangle and the redefinition of the SI ampere and kilogram; Analysis of a reduced set of observational equations," *Metrologia*, vol. 47, no. 3, p. 279, 2010.

[181] J. P. Pekola, O.-P. Saira, V. F. Maisi, A. Kemppinen, M. Möttönen, Y. A. Pashkin, and D. V. Averin, "Single-electron current sources: Toward a refined definition of the ampere," *Reviews of Modern Physics*, vol. 85, no. 4, pp. 1421–1472, 2013.

[182] M. W. Keller, J. M. Martinis, N. M. Zimmerman, and A. H. Steinbach, "Accuracy of electron counting using a 7-junction electron pump," *Applied Physics Letters*, vol. 69, no. 12, pp. 1804–1806, 1996.

[183] X. Jehl, B. Voisin, T. Charron, P. Clapera, S. Ray, B. Roche, M. Sanquer, S. Djordjevic, L. Devoille, R. Wacquez, and M. Vinet, "Hybrid metal-semiconductor electron pump for quantum metrology," *Physical Review X*, vol. 3, no. 2, p. 021012, 2013.

[184] F. Stein, D. Drung, L. Fricke, H. Scherer, F. Hohls, C. Leicht, M. Götz, C. Krause, R. Behr, E. Pesel, K. Pierz, U. Siegner, F. J. Ahlers, and H. W. Schumacher, "Validation of a quantized-current source with 0.2 ppm uncertainty," *Applied Physics Letters*, vol. 107, no. 10, p. 103501, 2015.

[185] F. Hohls, A. C. Welker, C. Leicht, L. Fricke, B. Kaestner, P. Mirovsky, A. Müller, K. Pierz, U. Siegner, and H. W. Schumacher, "Semiconductor quantized voltage source," *Physical Review Letters*, vol. 109, no. 5, p. 056802, 2012.

[186] G. P. Lansbergen, Y. Ono, and A. Fujiwara, "Donor-based single electron pumps with tunable donor binding energy," *Nano Letters*, vol. 12, no. 2, pp. 763–768, 2012.

[187] B. Roche, R. P. Riwar, B. Voisin, E. Dupont-Ferrier, R. Wacquez, M. Vinet, M. Sanquer, J. Splettstoesser, and X. Jehl, "A two-atom electron pump," *Nature Communications*, vol. 4, p. 1581, 2013.

[188] G. Yamahata, K. Nishiguchi, and A. Fujiwara, "Gigahertz single-trap electron pumps in silicon," *Nature Communications*, vol. 5, p. 5038, 2014.

[189] T. Wenz, F. Hohls, X. Jehl, M. Sanquer, S. Barraud, J. Klochan, G. Barinovs, and V. Kashcheyevs, "Dopant-controlled single-electron pumping through a metallic island," *Applied Physics Letters*, vol. 108, no. 21, p. 213107, 2016.

[190] B. Kaestner, C. Leicht, V. Kashcheyevs, K. Pierz, U. Siegner, and H. W. Schumacher, "Single-parameter quantized charge pumping in high magnetic fields," *Applied Physics Letters*, vol. 94, no. 1, p. 012106, 2009.

[191] G. Yamahata, K. Nishiguchi, and A. Fujiwara, "Accuracy evaluation of single-electron shuttle transfer in Si nanowire metal-oxide-semiconductor field-effect transistors," *Applied Physics Letters*, vol. 98, no. 22, p. 222104, 2011.

[192] L. Fricke, M. Wulf, B. Kaestner, V. Kashcheyevs, J. Timoshenko, P. Nazarov, F. Hohls, P. Mirovsky, B. Mackrodt, R. Dolata, T. Weimann, K. Pierz, and H. W. Schumacher, "Counting statistics for electron capture in a dynamic quantum dot," *Physical Review Letters*, vol. 110, no. 12, p. 126803, 2013.

[193] B. Kaestner and V. Kashcheyevs, "Non-adiabatic quantized charge pumping with tunable-barrier quantum dots: A review of current progress," *Reports on Progress in Physics*, vol. 78, no. 10, p. 103901, 2015.

[194] V. Kashcheyevs and B. Kaestner, "Universal decay cascade model for dynamic quantum dot initialization," *Physical Review Letters*, vol. 104, no. 18, p. 186805, 2010.

[195] C. Liu and Q. Niu, "Nonadiabatic effect in a quantum charge pump," *Physical Review B*, vol. 47, no. 19, pp. 13031–13034, 1993.

[196] M. Kataoka, J. D. Fletcher, P. See, S. P. Giblin, T. J. B. M. Janssen, J. P. Griffiths, G. A. C. Jones, I. Farrer, and D. A. Ritchie, "Tunable nonadiabatic excitation in a single-electron quantum dot," *Physical Review Letters*, vol. 106, no. 12, p. 126801, 2011.

[197] C. Jagannath, Z. W. Grabowski, and A. K. Ramdas, "Linewidths of the electronic excitation spectra of donors in silicon," *Physical Review B*, vol. 23, no. 5, pp. 2082–2098, 1981.

[198] R. Rahman, G. P. Lansbergen, S. H. Park, J. Verduijn, G. Klimeck, S. Rogge, and L. C. L. Hollenberg, "Orbital Stark effect and quantum confinement transition of donors in silicon," *Physical Review B*, vol. 80, no. 16, p. 165314, 2009.

[199] M. J. Calderón, J. Verduijn, G. P. Lansbergen, G. C. Tettamanzi, S. Rogge, and B. Koiller, "Heterointerface effects on the charging energy of the shallow D^- ground state in silicon: Role of dielectric mismatch," *Physical Review B*, vol. 82, no. 7, p. 075317, 2010.

[200] B. Roche, E. Dupont-Ferrier, B. Voisin, M. Cobian, X. Jehl, R. Wacquez, M. Vinet, Y. M. Niquet, and M. Sanquer, "Detection of a large valley-orbit splitting in silicon with two-donor spectroscopy," *Physical Review Letters*, vol. 108, no. 20, p. 206812, 2012.

[201] H. W. Hübers, S. G. Pavlov, and V. N. Shastin, "Terahertz lasers based on germanium and silicon," *Semiconductor Science and Technology*, vol. 20, no. 7, p. S211, 2005.

[202] R. K. Zhukavin, V. N. Shastin, S. G. Pavlov, H.-W. Hübers, J. N. Hovenier, T. O. Klaassen, and A. F. G. van der Meer, "Terahertz gain on shallow donor transitions in silicon," *Journal of Applied Physics*, vol. 102, no. 9, p. 093104, 2007.

[203] Ö. O. Soykal, R. Ruskov, and C. Tahan, "Sound-based analogue of cavity quantum electrodynamics in silicon," *Physical Review Letters*, vol. 107, no. 23, p. 235502, 2011.

[204] V. V. Tsyplenkov, E. V. Demidov, K. A. Kovalevsky, and V. N. Shastin, "Relaxation of excited donor states in silicon with emission of intervalley phonons," *Semiconductors*, vol. 42, no. 9, pp. 1016–1022, 2008.

[205] N. Q. Vinh, P. T. Greenland, K. Litvinenko, B. Redlich, A. F. G. van der Meer, S. A. Lynch, M. Warner, A. M. Stoneham, G. Aeppli, D. J. Paul, C. R. Pidgeon, and B. N. Murdin, "Silicon as a model ion trap: Time domain measurements of donor Rydberg states," *Proceedings of the National Academy of Sciences*, vol. 105, no. 31, pp. 10649–10653, 2008.

[206] A. D. C. Alves, J. Newnham, J. A. van Donkelaar, S. Rubanov, J. C. McCallum, and D. N. Jamieson, "Controlled deterministic implantation by nanostencil lithography at the limit of ion-aperture straggling," *Nanotechnology*, vol. 24, no. 14, p. 145304, 2013.